DISSERTATION

EMISSIONS, EVOLUTION, AND TRANSPORT OF AMMONIA (NH_3) FROM LARGE ANIMAL FEEDING OPERATIONS: A SUMMERTIME STUDY IN NORTHEASTERN COLORADO.

Submitted by
Julieta Fernanda Juncosa Calahorrano
Department of Atmospheric Science

In partial fulfillment of the requirements
For the Degree of Doctor of Philosophy
Colorado State University
Fort Collins, Colorado
Spring 2024

Doctoral Committee:

Advisor: Emily V. Fischer

Jeffrey L. Collett Jr.
Jeffrey R. Pierce
Shantanu H. Jathar

ABSTRACT

EMISSIONS, EVOLUTION, AND TRANSPORT OF AMMONIA (NH_3) FROM LARGE ANIMAL FEEDING OPERATIONS: A SUMMERTIME STUDY IN NORTHEASTERN COLORADO.

The Transport and Transformation of Ammonia ($\mathrm{TRANS^2Am}$) airborne field campaign occurred over northeastern Colorado during the summers of 2021 and 2022. $\mathrm{TRANS^2Am}$ measured ammonia ($\mathrm{NH_3}$) emissions from cattle feedlots and dairies with the goal of describing the near-field evolution of the $\mathrm{NH_3}$ emitted from animal feeding operations. Most of the animal husbandry facilities in Colorado are co-located with oil and gas development within the Denver-Julesburg basin, an important source of methane ($\mathrm{CH_4}$) and ethane ($\mathrm{C_2H_6}$) in the region. Leveraging $\mathrm{TRANS^2Am}$ observations, this dissertation presents estimates of $\mathrm{NH_3}$ emissions ratios with respect to $\mathrm{CH_4}$ ($\mathrm{NH_3}$ EmR), with and without correction of $\mathrm{CH_4}$ from oil and gas, for 29 feedlots and dairies in the region. The data show larger emissions ratios than previously reported in the literature with a large range of values (i.e., 0.1 - 2.6 ppbv ppbv^{-1}). Facilities housing cattle and dairy had a mean (std) of 1.20 (0.63) and 0.29 (0.08) ppbv ppbv^{-1}, respectively. $\mathrm{NH_3}$ emissions have a strong dependency with time of day, with peak emissions around noon and lower emissions earlier in the morning and during the evening. On average across all near-source sampling, only 15% of the total ammonia ($\mathrm{NH_x}$) is in the particle phase (i.e., $\mathrm{NH_4}^+$) near major sources during the warm summer months. Finally, estimates of $\mathrm{NH_3}$ emission rates from 4 optimally sampled facilities range from 4 - 29 g $\mathrm{NH_3} \cdot \mathrm{h^{-1}} \cdot \mathrm{hd^{-1}}$.

This work also investigates the nearfield evolution of $\mathrm{NH_3}$ in five plumes from large animal husbandry facilities observed during $\mathrm{TRANS^2Am}$ using a mass balance approach with $\mathrm{CH_4}$ as a conservative tracer in the timescales of plume transport. Since the plumes in $\mathrm{TRANS^2Am}$ were not sampled in a pseudo-lagrangian manner, an empirical model is needed to correct for variations in summertime $\mathrm{NH_3}$ emissions as a function of local time (LT) (CF = 1.87ln(LT) - 3.95). Results from the mass balance approach show that the average summertime $\mathrm{NH_3}$ decay time below 80% and 60% against deposition in plumes from large animal feeding operations is $\sim$1 and $\sim$2 hours, respectively. Additionally, we present estimates of deposition/emission fluxes every 5 km downwind of the plume. We found that deposition almost always happens in the first 10 km from the emission source. Beyond that, the complex environmental exchange of $\mathrm{NH_3}$ between the atmosphere and the surface suggests that fresh $\mathrm{NH_3}$ emissions from small nearby sources, water bodies, and crops/soil could contribute to sufficient $\mathrm{NH_3}$ to switch the direction of the flux (to emission). Large uncertainties still remain in emission and deposition fluxes, shining light on the need for more measurements in the region. To our knowledge, this is the first study presenting $\mathrm{NH_3}$ evolution in the atmosphere using a conservative tracer and airborne measurements.

The second goal of $\mathrm{TRANS^2Am}$ was to investigate easterly wind conditions capable of moving agricultural emissions of ammonia ($\mathrm{NH_3}$) through urban areas and into the Rocky Mountains. $\mathrm{TRANS^2Am}$ captured 6 of these events, unveiling important commonalities. 1) $\mathrm{NH_3}$ enhancements are present over the mountains on summer afternoons when easterly winds are present in the foothills region. 2) The abundance of summertime gas-phase $\mathrm{NH_3}$ is 1 and 2 orders of magnitude higher than particle-phase $\mathrm{NH_4}^+$ over the mountains and major agricultural sources, respectively. 3) During thermally driven circulation periods, emissions from animal husbandry sources closer to the mountains likely contribute more to the $\mathrm{NH_3}$ observed over the mountains than sources located further east. 4) Transport of summertime plumes from major animal husbandry sources in northeastern Colorado westward across the foothills requires $\sim$5 hours. 5) Winds drive variability in the transport of $\mathrm{NH_3}$ into nearby mountain ecosystems, producing both direct plume transport and recirculation. A similar campaign in other seasons, including spring and autumn, when synoptic scale events can produce sustained upslope transport, would place these results in context.

ACKNOWLEDGEMENTS

A thousand thank yous to Emily Fischer. It has been such a blessing spending these five and a half years learning from you, sharing the excitement of new discoveries and a job well-done, and working through the hardships life throws at us. I am leaving CSU a better person and scientist than when I arrived. You have been the most important support in this journey, and I am joyful that our paths crossed in 2017. Thanks for betting and believing in this Ecuadorian! I look forward to having more science talks with you, from wherever life takes us.

To my committee, Jeff C., Jeff P., and Shantanu. You are all such knowledgeable and kind people. Your insights and questions have pushed me to be a better scientist and make this project better. Shantanu, thank you for chatting with me about what it's like to be a foreign scientist in the U.S. Jeff P. thank you for all the hallway conversations we've had about a thousand things, including swimming. I also want to thank A.R. Ravishankara. Ravi, thank you for supporting me and my career so much. It is always fun and interesting chatting with you and learning about your many life experience.

Thanks to the CSU Department of Atmospheric Science. You do not shine away from problems and the ability of the department to change and improve never ceased to impress me. That is a lesson I am taking with me wherever I go.

To my friends, who made this journey so much more enjoyable. Thank you, Ali, Mai, I-Ting, Richie, Mo, Vicky, Emi, Joaco, Juanma and so many more. I love you all!

Sally, AJ, and Ivis, you were all an essential part of my life in the U.S. Thanks to you I learnt to discover, trust, and take care of myself. You are all amazing people and therapists. You all will always have a special space in my heart.

Finally, thank you to my family. Mami, papi, ñaño y Gabi! Gran parte de quién soy es por nuestra familia. Mami y papi, gracias por acompañarme, escucharme, y entenderme durante los buenos y malos momentos. Y gracias por ser los mejores compañeros de viaje del mundo! Gracias a los ñaños, sé que siempre puedo contar con ustedes.

DEDICATION

To the many more Latinas that will come into the field of Atmospheric Science.

TABLE OF CONTENTS

LIST OF TABLES

LIST OF FIGURES

Chapter 1

Introduction

Ammonia ($\mathrm{NH_3}$) is the most abundant alkaline gas in the atmosphere. It is a precursor for the formation of fine particulate matter ($\mathrm{PM_{2.5}}$) (Bauer et al., 2016), which impacts human health and Earth's radiative balance. It also is a major determinant of aerosol pH, with implications for cloud formation and aerosol chemistry (Karydis et al., 2021). $\mathrm{NH_3}$ can also readily undergo dry and wet deposition, altering the biogeochemical balance of the nitrogen (N) within ecosystems. N cycling is essential for the biological and chemical processes sustaining life on Earth. The imbalance in the N cycle, caused by a doubling of N anthropogenic emissions since the Industrial Revolution, has been identified by the unhealthy accumulation of N in water reservoirs, soils, and, temporarily, in the atmosphere (Fowler et al., 2013; Galloway et al., 2003; Fenn et al., 1998). The environmental implications of N emissions, deposition, and accumulation include soil acidification, water eutrophication, and air pollution (Baron et al., 2000; Lieb et al., 2011; Wolfe et al., 2001; Wolfe et al., 2003; Wyer et al., 2022; Zhan et al. 2017). Over the last decade, reduced forms of N ($\mathrm{NH_x}$ = $\mathrm{NH_3}$ + $\mathrm{NH_4}^{+}$) have become the primary source of N deposition in the U.S. and other regions of the globe (Ackerman et al., 2019; Li et al., 2016). Despite the known impacts of $\mathrm{NH_3}$ on ecosystems and human health, it is not a regulated pollutant, which has resulted in large uncertainties in its emissions inventories and overall understanding of its atmospheric fate once emitted to the atmosphere.

$\mathrm{NH_3}$ emissions worldwide have increased over recent decades, largely driven by the need for higher yields in animal and crop production related to food security concerns (Sutton et al., 2008; Galloway et al., 2004). Agriculture activities, including livestock and fertilizer application, account for over 80$\%$ of $\mathrm{NH_3}$ emissions in the U.S., Europe, and China (Van Damme et al., 2018). It is estimated that $\mathrm{NH_3}$ from agriculture can contribute 15 - 50$\%$ of the $\mathrm{PM_{2.5}}$ in these countries (Wyer et al., 2022; Liu et al., 2022). Other sources include vehicles using 3-way catalytic converters or urea to reduce emissions of nitrogen oxides ($\mathrm{NO_x}$), industrial processes including power plants, waste treatment plants (water treatment plants and landfills), soils and vegetation in natural environments, biomass burning, and water bodies (Meng et al., 2017; Xu et al., 2019; Lindaas et al., 2021; Behera et al., 2013). Some of these smaller sources can have a larger relative contribution to NH_3 concentrations in places without intensive agriculture. However, in regions downwind of agricultural practices, the contribution of agriculture to NH_3 surpasses the contribution from smaller and transient sources (e.g., biomass burning).

The deposition of N over the U.S. has recently switched from being dominated by oxidized N to being dominated by reduced N (e.g., NH_3) (Li et al., 2016). This is partly due to successful regulatory measures to decrease the emission of nitrogen oxides (i.e., NO_x) accompanied by unregulated and increasing emissions of NH_3 (Davidson et al., 2011; Kim et al., 2006; Tong et al., 2015). Most of the NH_3 emissions in the U.S. are attributed to fertilizer application (21%) and livestock (59%) (NEI, 2017). The U.S. is the largest producer of beef in the world, and 80% of the country's beef cattle and dairy cows are concentrated in the Great Plains region, one of the most intensive areas of agricultural production in the country and worldwide, and in parts of the Southwest, and Pacific Northwest (USDA, 2012). Satellite and in-situ observations in these regions show elevated concentrations of atmospheric NH_3 and NH_x deposition compared to other regions in the U.S. (e.g., Van Damme et al., 2018; Li et al., 2016). These findings can be directly tied to intensive agriculture and suggest that NH_3 emissions have a local influence due to its short lifetime in the atmosphere.

NH_3 from livestock is emitted to the atmosphere through biological and chemical bacterial decomposition of excreted N. Livestock eat protein- and N-rich feed in order to yield desirable N-rich products (i.e., meat, milk, eggs). However, most of the N in the feed (70 - 95%) is eliminated through excretion rather than converted to the N-rich products, resulting in large emissions of NH_3 and other N compounds (i.e., nitrous oxide (N_2O)) (Huntington and Archibeque, 1999). Other gasses emitted from animal feeding operations include three greenhouse gasses: methane (CH_4), N_2O, and carbon dioxide (CO_2). CH_4 and N_2O have 34 and 298 times the 100-year Global Potential Warming of CO_2, respectively (Myhre et al., 2013). Livestock emits CH_4 through enteric fermentation. Emitted NH_3 and CH_4 from livestock vary greatly depending on diurnal and seasonal cycles and the number of animals in each facility. Manure treatment and storage methods greatly influence the emissions of NH_3 and CH_4 (Eilerman et al., 2016). Proposed strategies to reduce the emission of NH_3 to the environment include reducing high protein feed, frequent removal of manure and separation of it from urine, filtration of emissions from confinement facilities (i.e., scrubbers/filters), controlling conditions to keep low temperatures and low pH in the manure, and injection or incorporation of NH_3 into the soil soon after fertilizer application (Ndegwa et al., 2008; Brandani et al., 2023).

Historical challenges in measuring NH_3 have limited progress on emissions estimates and the study of the chemical evolution of this pollutant in the atmosphere. NH_3 is a sticky molecule, which can lead to negative and positive artifacts in measurements (von Bobrutzki et al., 2010). Additionally, NH_3 in the atmosphere has complex bidirectional interactions with the surfaces as these can act as net sinks or sources of NH_3 to the atmosphere (Sutton et al., 1998). Emissions of NH_3 from plants and soil depend on the crop/soil type, temperature and humidity (air, soil, solution (e.g., plant leaf), and N status in the solution (i.e., soil, leaves) (Pleim et al., 2019). Therefore, there can be a dynamic exchange of NH_3 between the atmosphere and the surface. The relationship between the NH_3 ambient concentration and the surface compensation point (χ) determines the direction of the NH_3 exchange between the surface and the atmosphere. If the NH_3 concentration above the surface is higher than χ, NH_3 will deposit to the surface. If the NH_3 concentration above the surface is lower than χ, NH_3 will likely be emitted from the surface. If the NH_3 concentration above the surface is similar to χ, the direction of the NH_3 fluxes will change in short timescales depending on environmental and micrometeorological conditions.

Recent advances in measuring NH_3, including in-situ measurements (e.g., Pollack et al., 2019; Roscioli et al., 2016; Ellis et al., 2010) and satellite retrievals (e.g., Van Damme et al., 2018), have increased our awareness of the importance of measuring NH_3 from large point sources. The availability of new observations has helped models to represent NH_3 emissions in the U.S (Zhu et al., 2015) and worldwide (Clarisse et al., 2009) better, and they have revealed the potential underestimation of $\mathrm{NH_3}$ emission inventories (e.g., Heald et al., 2012; Nowak et al., 2012). Considerable deposition of N in and around sensitive ecosystems has been identified as one of the leading problems resulting from $\mathrm{NH_3}$ emission in the U.S. (Benedict et al., 2013a and 2013b) and globally (Liu et al., 2022). However, less is known about the fate of $\mathrm{NH_3}$ emitted from large point sources and its impact on the surrounding environment. Due to the increasing number of $\mathrm{NH_3}$ sources worldwide and the uncertainty in the magnitude and behavior of $\mathrm{NH_3}$ emissions, more detailed measurements are needed.

In this work, we focus on the $\mathrm{NH_3}$ emissions from livestock facilities in Colorado. Over 500,000 head of cattle are present in Colorado counties located in the northeastern portion of the state (CDPHE, 2014), and individual facilities are observable from satellite sensors (Van Damme et al., 2018). $\mathrm{NH_3}$ emissions and their transport have received special attention in Colorado due to the observed negative impacts of reduced N deposition on ecosystems in Rocky Mountain National Park (RMNP) (Baron et al., 2000). N-deposition is of particular concern in N-limited ecosystems, such as those in the Western U.S., where small increases in N can lead to undesirable environmental impacts. For example, N deposition in RMNP (Baron et al., 2000; Baumann et al., 1997; Benedict et al., 2013b; Bowman et al., 2012; Burns, 2004; Lieb et al., 2011; Malm et al., 2013) has been linked to adverse effects on biological and ecological processes (Bowman & Stelzer, 1998; Burn 2004; Baron 2006; Wolfe et al., 2001; Wolfe et al., 2003). RMNP is located southwest of a large animal agricultural area extending from the eastern plains to the northern Colorado foothills. RMNP is prone to N deposition, especially on days when synoptic (mainly spring/autumn) or thermally driven (especially summer) upslope winds transport agricultural emissions through the urban corridor, the foothills, and into RMNP (Piña et al., 2019; Baron et al., 2000).

Over the last three decades, several studies have worked to observe and attribute observed increases in N deposition in RMNP. Baumann et al. (1997) linked increased chemical tracer concentrations to easterly flow (i.e., upslope winds) in three mountain sites at RMNP. Field campaigns such as the Rocky Mountain Atmospheric Nitrogen and Sulfur Studies (RoMANS and RoMANS II) increased the temporal and spatial range of gas- and particle-phase observations across Colorado. Measurements from RoMANS I and II showed regional gradients of $\mathrm{NH_x}$ with higher concentrations near source emissions (especially east of the park) that decreased towards the mountains (Beem et al., 2010; Benedict et al., 2013b). By establishing year-long observations, Benedict et al. (2013a) showed that spring and summer are the peak periods for $\mathrm{NH_x}$ deposition at their monitoring site in RMNP. Benedict et al. (2013a) reported a calculated N-deposition rate of 3.65 kg N ha^{-1} y^{-1}. The critical load of N, defined as the amount of N that leads to harmful changes in an ecosystem (Baron, 2006), for wet N deposition and wet + dry N deposition in the RMNP, has been estimated at 1.5 and 3 kg N ha^{-1} y^{-1}, respectively (Baron, 2006; Baron et al., 2011; Bowman et al., 2012). Other analyses from RoMANS I and II based on models, trajectory analyses, and other source apportionment techniques attributed a large percentage (44 - 56 $\%$) of the reduced N observed in RMNP to sources within eastern Colorado, especially during summertime months (Gebhart et al., 2011; Malm et al., 2013; Gebhart et al., 2014; Thompson et al., 2015; Li et al., 2017). Benedict et al. (2018) reported on the diurnal cycles of N-containing species in the gas- and particle-phase in RMNP and found that higher concentrations are often present in the afternoon during the summer. Pan et al. (2021) observed higher N-deposition when air masses passed over upwind agricultural regions (7.9 ng m^{-2} s^{-1}) than over urban areas (1 ng m^{-2} s^{-1}). Prior studies support the hypothesis that a large percentage of N-deposition in RMNP can be attributed to emissions from agricultural sources located to the east, even though winds over the park are most often from the NW.

Overview of dissertation chapters and goals

This dissertation provides a better understanding of $\mathrm{NH_3}$ emissions from large livestock facilities and their transport to surrounding ecosystems. To this end, I use summertime airborne observation of $\mathrm{NH_3}$, $\mathrm{CH_4}$, ethane ($\mathrm{C_2H_6}$), and water-soluble aerosols collected over northern Colorado during Phase I and Phase II of the Transport and Transportation of Ammonia ($\mathrm{TRANS^2Am}$) field intensive. My work before, during, and after $\mathrm{TRANS^2Am}$ and the analysis presented here is a key contribution to a better quantification and understanding of $\mathrm{NH_3}$ emissions from large livestock facilities using state-of-the-science measurements. My research focused on 1) quantifying the magnitude of emissions from livestock facilities housing beef cattle and dairy cows in northeastern Colorado during summertime conditions and exploring the factors driving observed variability; 2) studying the loss rates of fresh NH_3 emissions immediately downwind of animal husbandry facilities (<25 km downwind); and 3) documenting the anatomy of the transport of NH_3 - rich plumes to RMNP under easterly winds. This analysis allows me to present a comprehensive picture of NH_3 emissions, evolution, and regional transport

Chapter 2 includes the common methodology used for this research. I present a detailed description of the study region (Section 2.1) and an overview of the $\mathrm{TRANS^2Am}$ field campaign (Section 2.2). Section 2.3 presents the sampling strategy used during $\mathrm{TRANS^2Am}$ for near-source and upslope sampling. A detailed description of the airborne payload is included in Section 2.4. Finally, the analysis approaches and calculations (Section 2.5) used in Chapters 3, 4, and 5 are presented in Sections 2.5.1, 2.5.2, and 2.5.3, respectively.

Chapter 3 contains the results of a paper published in the *Journal of Geophysical Research* (JGR) in 2023 (Juncosa Calahorrano et al., 2023). Using near-source sampling of NH_3 emissions during Phase I of $\mathrm{TRANS^2Am}$, this paper reports a) a summary of summertime NH_3 emission ratios with respect to CH_4 representing 29 beef cattle and dairy facilities and their dependence on temperature and time of day, b) estimates of the differences between emission ratios associated with beef cattle and dairy cow facilities, and c) NH_3 emission rate estimates as a function of maximum animal capacity for select comprehensively sampled facilities.

In Chapter 4, I use near-source sampling of five plumes from large livestock facilities sampled during Phase I and Phase II of $\mathrm{TRANS^2Am}$ to present an analysis of NH_3 evolution in the atmosphere with respect to CH_4, considered a conserved tracer in the time scales relevant to the transport of agricultural plumes (i.e., hours). Summertime partitioning of NH_3 to the aerosol phase in the near source during TRANS^{2}Am is negligible (Li et al., under review). Therefore, we assume that the only loss process of NH_3 for our dataset is dry deposition to the surface. I report on the timescales of NH_3 loss in plumes from large animal feeding operations and the magnitude of the fluxes (emission and deposition) downwind of each emission source. This chapter is currently in preparattion to be submitted to *Environmental Science and Technology* (ES&T).

Chapter 5 has been submitted for publication to the journal *Environmental Science and Technology* (ES&T) (Juncosa Calahorrano et al., submitted). Using observations of upslope events during Phase I and Phase II of $\mathrm{TRANS^2Am}$, I present aircraft observations of $\mathrm{NH_x}$ plumes as they travel from the eastern agricultural region across the Colorado Front Range urban corridor and into the Rocky Mountains during summer. We quantify plume transit times and identify different flow patterns that support the movement of agricultural $\mathrm{NH_x}$ plumes into the mountains and their recirculation. We also identify particular regions and facilities with high potential for plume transport into the mountains during summer upslope events.

Finally, Chapter 6 summarizes the findings in this dissertation and provides recommendations for future field studies related to $\mathrm{NH_3}$ emissions.

Chapter 2

Methods

2.1 Study Region

Colorado has a large number of livestock operations (Figure 2.1a), and the majority and largest facilities (in terms of maximum reported animal capacity) in this region house beef cattle and dairy cows (blue and pink dots, respectively in Figure 2.1). Over 1 million animals are clustered in counties in the northeast part of the state (i.e., Larimer, Weld, Morgan, Washington, Yuma, Logan, and Phillips). While many of these operations are large sources of trace gases, separating and quantifying the emissions from individual facilities is difficult because many facilities are located in close proximity to the dense oil and gas development throughout much of the area (i.e., Denver-Julesburg basin - black dots in Figure 2.1a and 2.1b), as well as large urban centers (i.e., vehicle traffic and industrial sources along the Colorado Front Range corridor). Rocky Mountain National Park (RMNP) and other sensitive high-alpine areas are located directly west of the polluted Colorado Front Range. N deposition in this area is dominated by reduced N during upslope events (easterly winds) that carry emissions from the eastern plains to the mountain ecosystems (Benedict et al., 2013a; 2013b; Li et al., 2016, Pan et al., 2021). Agricultural emissions traveling due west cross over urban centers where other urban pollutants (i.e., nitric acid (HNO_3)) are available for forming fine particulate matter ($PM_{2.5}$) through ammonium nitrate (NH_4NO_3) formation.

Several recent measurement campaigns have aimed at characterizing emissions from animal husbandry in the region. For example, Eilermain et al. (2016) report on a year-long ground-based survey of 4 facilities housing beef, dairy, and sheep, and this report summarizes their diurnal and seasonal variations. The study highlights the strong relationship between NH_3 emissions and time of the day. Kille et al. (2019) apportioned CH_4 emissions in the region to either oil and gas or agriculture using ethane (C_2H_6) and NH_3 as tracers for each of these sources, respectively. This resulted in NH_3 emissions ratios with respect to CH_4 for the region. The Ammonia Phase

Partitioning and Transport (APART) field campaign was the proof of concept field study leading to TRANS^{2}Am. They characterized plumes downwind of five beef cattle facilities during November 2019, showing that NH_3 near-source emissions can be tracked using airborne platforms. They found that large NH_3 emissions ratios can be observed during cooler temperature conditions in the region (Pollack et al., 2022 and McCabe et al., 2023). Finally, Golston et al. (2020) deployed three mobile platforms in the summer of 2014. They intercepted NH_3 and CH_4 plumes downwind of 43 facilities (15 beef, 25 dairy, 1 sheep, and 2 poultry) in the region and found a large underestimation in emissions inventories (i.e., NEI and EDGAR) for NH_3 and CH_4 as well as significant site-to-site variability for NH_3 and CH_4 emissions. The NH_3 emission ratios with respect to CH_4 from all the studies listed above range between 0.17 and 2.7 ppbv ppbv^{-1}. Even fewer studies (Kille et al., 2017; McCabe et al., 2023; Golston et al., 2020) report emission rates of NH_3 (rather than emissions ratios that are normalized by CH_4) in the region. The few studies reporting emission rates of NH_3 highlight the need for more systematic measurements to estimate this magnitude in the region (Kille et al., 2017; McCabe et al., 2023; Golston et al., 2020). Because of the large number of facilities in the region and the large variability in their near-source emissions and evolution, large uncertainties remain on what NH_3 emissions from livestock are in Colorado.

2.2 Campaign overview

The TRANS^{2}Am field campaign occurred over two phases: Phase I: 27 July 2021 - 23 August 2021, and Phase II: 16 August 2022 - 02 September 2022. The field campaign was halted abruptly in August 2021 when the plane was damaged by a collision with a bird and then resumed in 2022. TRANS^{2}Am had a total flight time of $\sim$77 hours. Of those flight hours, 75% were dedicated to sampling near-sources (RF01- RF06, RF08 - RF09, RF11 - RF15, RF17, RF19, RF22 - RF23) and 25% to sampling upslope events (TF04, RF07, RF10, RF16, RF18, RF21). One additional flight ($\sim$2 h) was focused on validating NH_3 observations from the Cross Track Infrared Sounder (CrIS) on board of the Suomi-NPP satellite (RF20). The study region was impacted by local and transported smoke during Phase I (summer 2021). The smoke was transported from fires

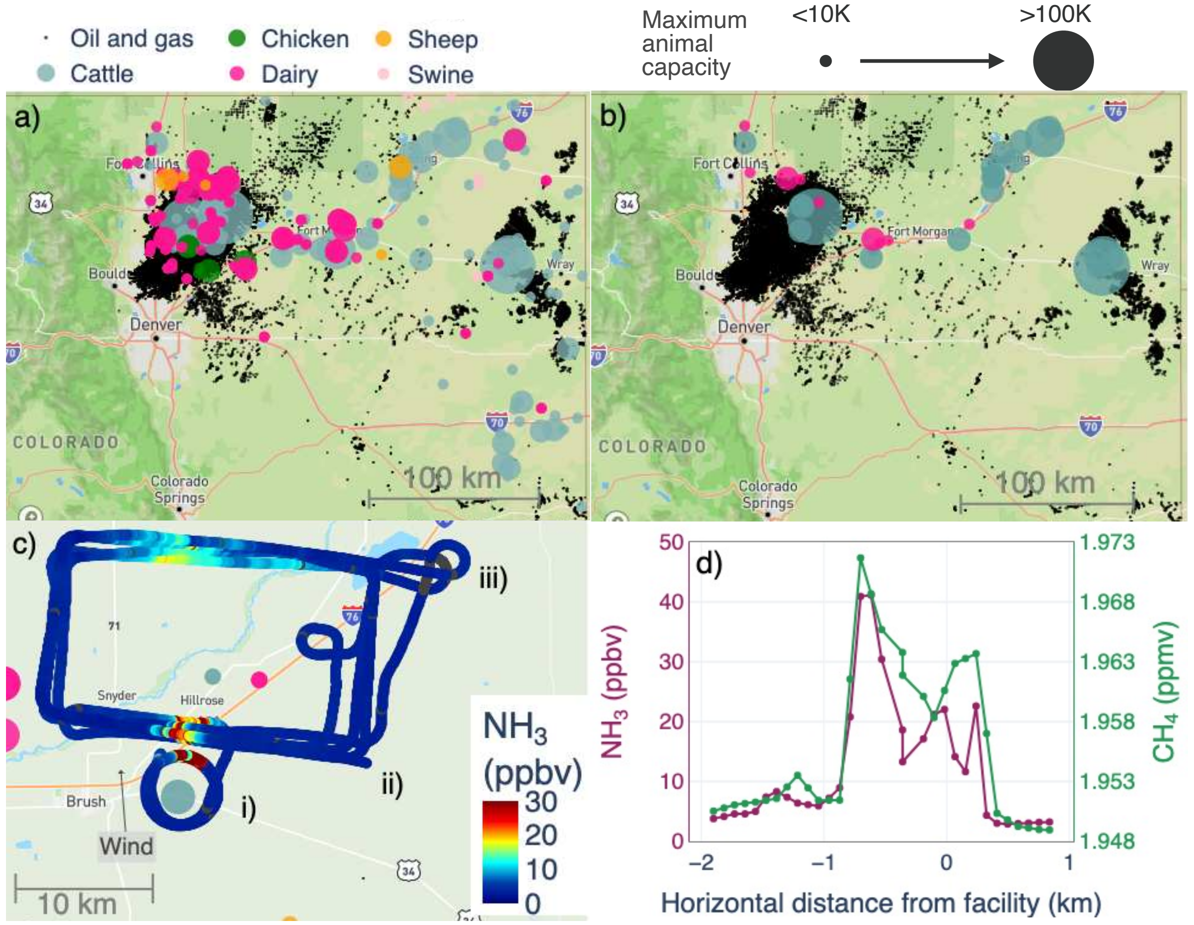

Figure 2.1: a) Map of northeastern Colorado showing the large number of livestock facilities in the region. The different colors signify the type of animal housed at each facility, and the size of the marker is proportional to the maximum animal capacity. Black dots indicate the locations of active oil and gas wells as of 2015. b) Same map as a) but only including facilities sampled systematically during Phase I of TRANS^{2}Am. c) Flight track of the UWKA colored by NH_3 (ppbv) during the sampling of Facility 1 (F01; refer to Table 3.1 for more information) on 02 August 2021. This example flight track is representative of the general sampling strategy used during TRANS^{2}Am. Letters (i, ii, iii) refer to different vertical transects used for emission rate calculations (refer to Figure 3.5 and Section 2.5.1.5 for more information). d) Example of a transect with colocated enhancements of NH_3 (ppbv; purple) and CH_4 (ppmv; green) vs. horizontal distance from the facility. Note that we include non-plume background values in each transect (i.e., tails on each side of each transect).

originating in the western U.S. (Washington, Oregon, California, Arizona) (NCEI, 2021). This was not the case during Phase II (summer 2022), where levels of carbon monoxide (CO) across all flights were lower.

During Phase I and II of TRANS^{2}Am, the University of Wyoming King Air (UWKA) was based at Laramie Regional Airport (KLAR) in Laramie, WY, and was deployed to the northern Colorado Front Range. A mobile lab was also deployed for the sampling of RF21 (see Figure A1 and **Mobile Lab Payload** in Appendix A). Figure 2.1a shows the study region, and Figure 2.1b shows the facilities for which we provide NH_3 emission estimates. The flight patterns associated with TRANS^{2}Am were designed to meet two sets of objectives. The first set of objectives focuses on near-source emissions and evolution, and the second set of objectives focuses on the regional transport of reduced N into the nearby Rocky Mountains. Below we describe the sampling strategy for each of the flight patterns.

2.3 Sampling Approach

2.3.1 Near-source Sampling Approach

The approach to sample and follow plumes from specific large animal husbandry sources encompassed four steps and an example of this approach is provided in Figure 2.1c, and Figures 2.2a - 2.2e. 1) The UWKA characterized the planetary boundary layer (PBL) after take-off by climbing to the top of the PBL and during descent while approaching the region with the target facility. 2) Once the pilot visually identified the target facility, the UWKA circled it at ∼300 m (∼1000 ft) agl in order to identify any obstacles and determine the plume outflow direction. When no obstacles were identified, the UWKA proceeded to perform an additional circle of the facility at ∼150 m (∼500 ft) agl. During these maneuvers, the aircraft remained ∼1 km from the edge of each facility to limit the noise exposure for the animals. 3) Once the plume outflow location was determined, the UWKA completed a set of stacked boxes downwind at different vertical levels. Vertical altitudes were determined to optimize time and sampling throughout the PBL. The vertical distance between flight legs was ∼150 m (∼500 ft). The maximum altitude reached varied between ∼500 m (∼1500

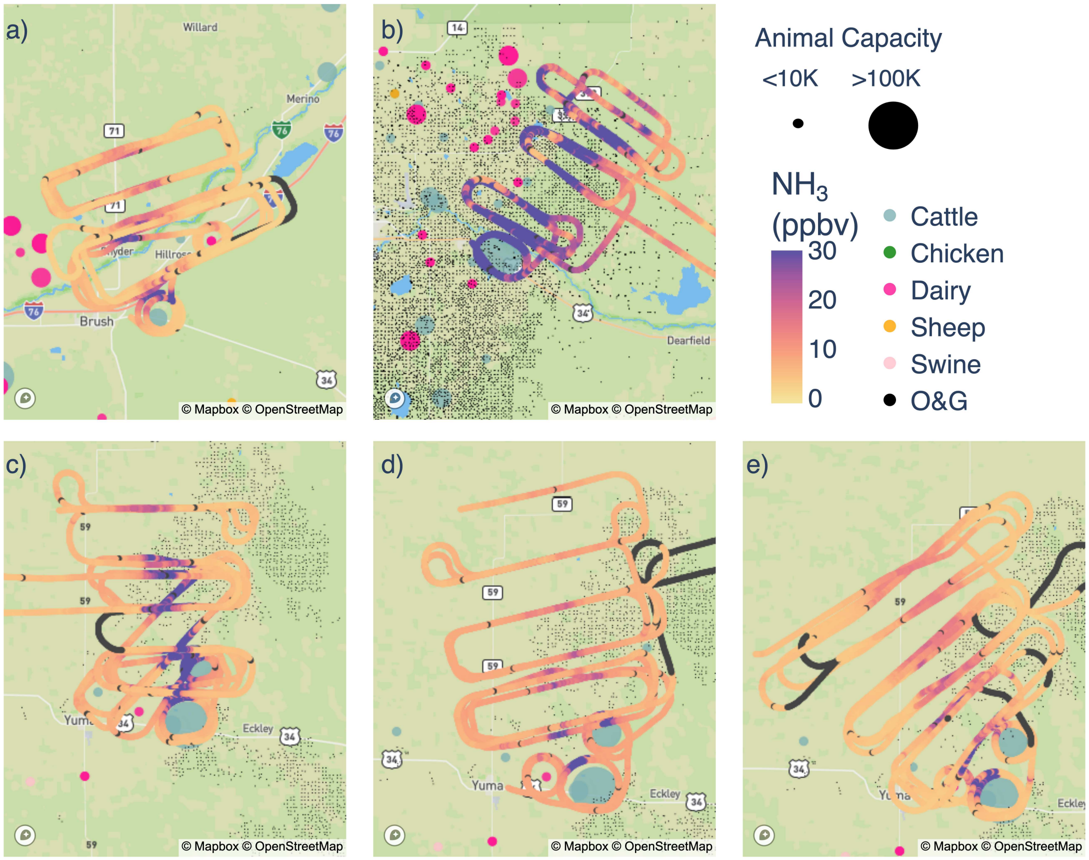

Figure 2.2: Flight track of the University of Wyoming King Air (UWKA) colored by NH$_3$ (ppbv) for the sampling of a) F01 during RF09 on August 14 2021, b) F04 during RF13 on August 23 2031, c) F27/28 during RF11 on August 17 2021, d) F27/28 during RF19 on August 21 2022, and e) F27/28 during RF22 on August 30, 2022. The colored circles represent the type of animal housed in each facility and they are sized by the reported animal maximum capacity. The black dots represent active oil and gas wells as of 2015. Blacked-out areas represent periods of zero measurements. Note, Van Damme et al. (2018) reported on various NH$_3$ hotspots around the world visible from satellite. The region shown in Figures 1c, 1d, and 1e was featured in that analysis. Sampling of F27/28 during RF11 (panel c) was originally envisioned with wind from the southwest, allowing us to sample a single plume from both facilities (F27 and F28). Upon arrival to the site we encountered strong winds from the south which positioned the plume from F27 upwind of the from F28.

ft) and 1800 m (∼6000 ft) agl based on i) the predicted planetary boundary layer (PBL) height for that day, ii) real-time assessment of the plume enhancements at higher altitudes, and iii) overall flight time constraints (max 3h and 40 min). The closest and furthermost legs of the boxes were located ∼5 and 10 km downwind of each facility, respectively. These distances shifted slightly for safety considerations as needed (i.e., air traffic control and obstacles). 4) When plumes were clearly detected 10 km downwind, and time allowed, another set of stack boxes was completed further downwind (see Figure 2.2a - 2.2e). The vertically stacked legs downwind of the facility formed ''curtains" that can be used to calculate horizontal fluxes. Note that this sampling approach was designed to optimize samples of the vertical 'curtains' used to calculate emission rates rather than following a particular parcel of air downwind from the emission source. The data presented here cannot be considered pseudo-lagrangian sampling. Figure 2.1d shows an example transect of NH_3 and CH_4 produced from the sampling approach outlined above. Note the large co-located enhancements in both species (i.e., NH_3 and CH_4).

2.3.2 Upslope transport Sampling Approach

The TRANS^{2}Am sampling strategy for upslope conditions included four north-south flight ''legs" at two different altitudes (∼150-300 magl (500-1000 ft) and ∼450-600 magl (1500-2000 ft)) and different longitudes across the study region (Figure 2.3a). The average longitudes of the four legs from east to west were 104.50°W, 104.84°W, 105.21°W, and 105.50°W (L1 to L4). L1 and L2 were positioned in the region with the largest number of facilities in the area. The easternmost leg (L1) passed over large facilities (10,000 - >100,000 maximum animal capacities) containing cattle and dairy cows. During RF10, these legs were located further east, upwind of these large facilities, at ∼104.41°W. L2 was located downwind (west) of the densest concentration of livestock facilities and ∼10 km downwind of one of the largest facilities (maximum animal capacity > 100,000 hd) in the area. L3 was located west of the major Colorado urban corridor, which includes the cities of Fort Collins, Loveland, and Longmont. There are 22 animal husbandry facilities between L2 and L3, most of these facilities are dairies rather than cattle feedlots, and the

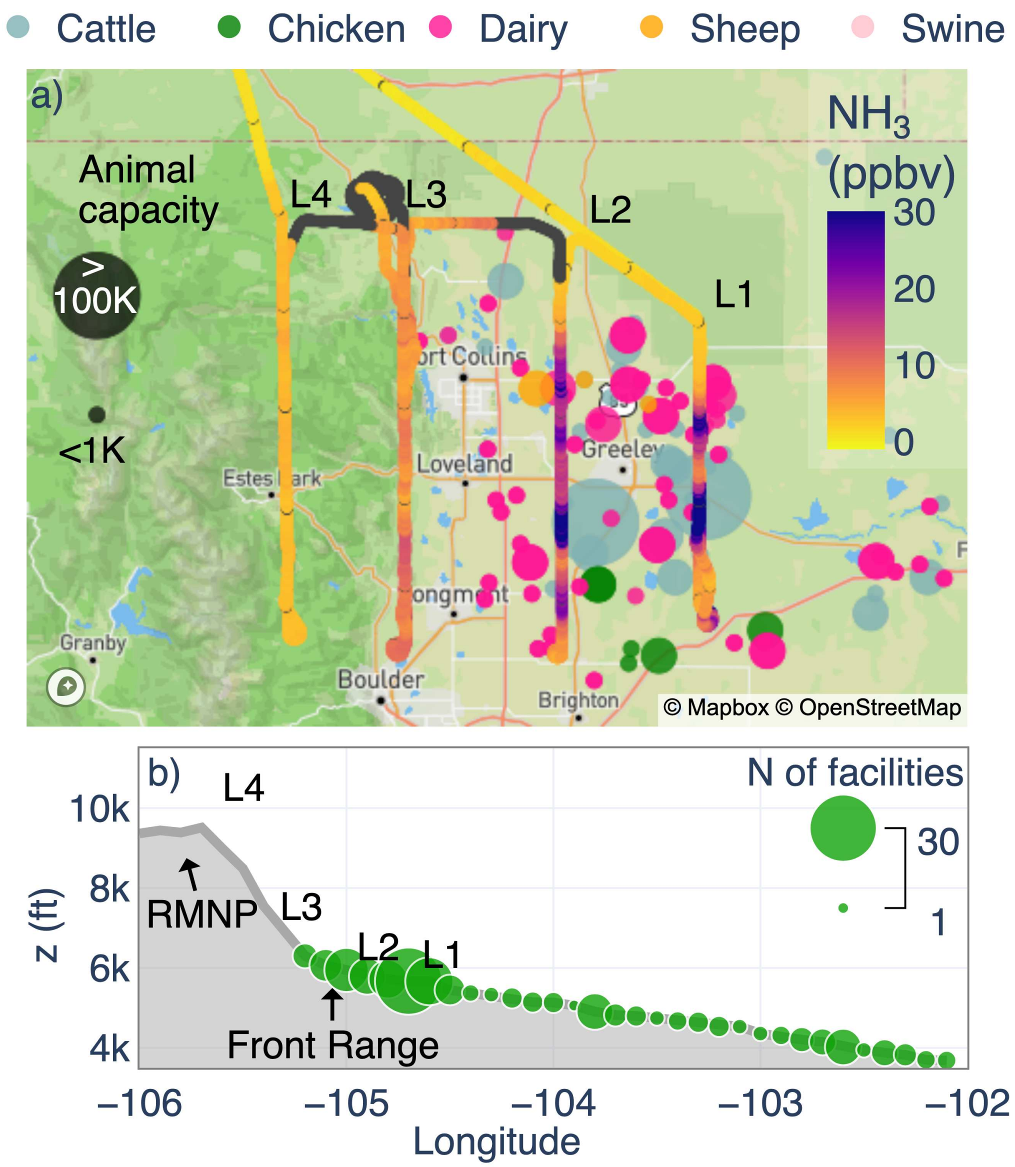

Figure 2.3: a) Flight track of the UWKA colored by NH_3 (ppbv) on August 29, 2022, between 13:10 and 16:20 local time (MT). This flight track is representative of sampling during Phase I and Phase II of TRANS^{2}Am under easterly winds. Dots represent agricultural facilities colored by the type of animal and sized by the reported maximum capacity in animal units. b) Longitudinal average (every 0.1º) of the study region terrain. The size of the green dots represents the number of facilities located at each longitude. The N-S bounds used for this terrain profile are 39 - 41.75 ºN.

maximum animal capacities are < 10,000 animals, with the exception of one large sheep farm. Finally, L4 passed over Estes Park, the town directly abutting RMNP to the east. Figure 2.3b shows an overview of terrain averaged longitudinally, overlaid with the animal feeding operation sources along each longitude.

2.4 Airborne payload

2.4.1 Gas-phase NH_3

NH_3 was measured using a Colorado State University (CSU) owned and operated commercial (Aerodyne Research, Inc.), single-channel, quantum-cascade tunable infrared laser direct absorption spectrometer (QC-TILDAS) operating at 967 cm^{-1} with an effective path length of 76 m (McManus et al., 1995; McManus et al., 2010; Zahniser et al., 1995, Ellis et al., 2010). The NH_3 instrument was utilized aboard the UWKA during APART, and details of the instrumentation are available in Pollack et al. (2022). Briefly, the spectrometer uses a direct absorption technique combined with a high sample flow rate (>10 SLPM) to achieve a fast (up to 10 Hz) collection of absolute NH_3 mixing ratios. The NH_3 QC-TILDAS is operated with a heated inertial inlet to provide filter-less separation of particles > 300 nm from the sample stream (Ellis et al., 2010). Prior studies show active continuous passivation of the instrument flow path with a strong perfluorinated base improves the time response of the NH_3 QC-TILDAS on mobile platforms (Roscioli et al., 2016). However, we found that a response time of 1 to 3 s associated with a 90% recovery in NH_3 signal could be maintained during TRANS^{2}Am flights without passivant addition by regularly cleaning the instrument sampling surfaces between flights (Pollack et al., 2019). During TRANS^{2}Am we did not add passivant to the instrument due to the deployment in series with the HNO_3 QC-TILDAS (see section 2.4.1). The NH_3 TILDAS is mounted on a vibrationally isolated apparatus and a constant high-frequency vibration is applied to the laser objective to wash out etalon fringe effects due to motion in flight, and thus there is minimal impact of motion sensitivity on instrument precision (Pollack et al., 2019). An injection-style aircraft inlet allows calibration and passivation gases to be introduced into the sample stream within a few centimeters of the inlet tip. The QC-TILDAS was calibrated on the ground between flights via standard addition to the sample stream with a known concentration of NH_3 generated from a temperature-regulated permeation tube. The instrument was regularly zeroed in flight by overflowing the inlet tip with a bottled source of NH_3-free, ultrapure (or ”zero”) air. The emission rate of the permeation device was calibrated before and after the flight intensive by the NOAA ultraviolet (UV) optical absorption system (Neuman et al., 2003). As reported in Pollack et al. (2019), adding individual uncertainties in quadrature resulted in a combined uncertainty of $\pm 12\%$ of the measured mixing ratio. During TRANS^{2}Am, the 1-Hz NH_3 measured mixing ratio had a 1-Hz precision in flight of 60 pptv corresponding to a 3-sigma detection limit of 180 pptv detection limit. Thus, the overall uncertainty of the instrument is reported as $\pm 12\%$ of the measured mixing ratio plus the 180 pptv detection limit.

2.4.2 Gas-phase HNO_3

Similar to NH_3, HNO_3 was measured using a commercial (Aerodyne Research, Inc.), single-channel, QC-TILDAS but operating at 1723 cm^{-1} with an effective path length of 76 m. The HNO_3 instrument is owned by Aerodyne and was operated by CSU during the TRANS^{2}Am field campaign. To make space for the complete payload and to maintain the >10 SLPM sample flow rate for up to 10 Hz collection, the NH_3 and HNO_3 instruments shared a common aircraft inlet, inertial inlet, and pumping system. Like the NH_3 instrument, the HNO_3 instrument was calibrated on the ground between flights via standard addition to the sample stream with a known concentration of HNO_3 generated from a temperature-regulated permeation device (Kin-Tech; verified by the NOAA UV optical absorption system (Neuman et al., 2003)). NH_3 and HNO_3 calibrations were performed individually with copious flushing of the sampling surfaces of the common inlet before application of the other calibrant. The HNO_3 instrument was regularly ‘’zeroed” with a bottled supply of ultrapure air in flight. Like NH_3, the HNO_3 instrument time response can be improved using active continuous passivation of the sampling surfaces using a strong acid (Roscioli et al., 2016). However, passivant addition is not possible when using a combined sample flow path with NH_3. The typical time response of the non-passivated HNO_3 instrument is $\sim$70 s for a 90%

recovery in signal (Roscioli et al., 2016). During TRANS^{2}Am, the time resolution of the HNO_3 instrument was degraded to $\sim$500 s for 90% signal recovery owing to the use of a common inlet and the HNO_3 QC-TILDAS being positioned downstream of the NH_3 QC-TILDAS in the flow path. Given this long-time response, future comparisons between HNO_3 and other species will require convolution of the fast measurements to the slower HNO_3 data. All the same, HNO_3 data was collected at 10 Hz and averaged to 1 Hz during Phase I of TRANS^{2}Am. The 1-Hz precision was 185 pptv, corresponding to a 3-sigma detection limit of 555 pptv at 1 Hz. The HNO_3 spectrometer was also mounted on vibration isolators and a constant high-frequency vibration was applied to the laser objective, and thus motion sensitivity in flight had a minimal impact on precision. The uncertainty related to the 1Hz samples is ±20% of the measured mixing ratio plus the 555 pptv detection limit.

2.4.3 C_2H_6

C_2H_6 measurements were collected at 1 Hz using a University of Wyoming-owned and operated commercial spectrometer (Aerodyne Research, Inc., Ethane Mini Trace Gas Monitor) employing a similar tunable infrared laser direct absorption spectroscopy (QC-TILDAS) technique as the NH_3 and HNO_3 instruments (Zahniser et al., 1995). The C_2H_6 instrument uses a 2990 cm^{-1} distributed feedback tunable diode laser, multipass cell with a path length of 76 m (McManus et al., 1995) and an infrared detector. The C_2H_6 QC-TILDAS is described in detail in Yacovitch et al. (2014). The instrument was zeroed periodically in flight with UZA and calibrated on the ground between flights using a high-accuracy (2.09 ± 0.01 ppb) standard purchased from NOAA ESRL. The 1-Hz precision in flight was 90 ppt resulting in a 3-sigma detection limit of 270 ppt.

2.4.4 CH_4, CO, CO_2, H_2O

CH_4, CO, CO_2 and H_2O were measured simultaneously using a University of Wyoming owned and operated Picarro G2401-m flight-ready analyzer. The instrument samples each species in rotation at $\sim$0.3 Hz. This closed-path instrument employs infrared cavity ring-down spectroscopy. Ambient air is pumped at a flow rate of 600 mL min^{-1} into an optical cavity that is maintained at

45 °C and 140 Torr (Crosson, 2008). Ultra-high reflectivity mirrors allow for multiple passes in the cavity, creating an effective path length >10 km and leading to high measurement sensitivity (Crosson, 2008). Precision was 30 ppb for CO, 200 ppb for CO_2 and 2 ppb for CH_4 with low drift. The stated low drift for a 24-hour period is 1.5 ppb for CH_4. Most of the flights of $TRANS^2Am$ were 4 hours long, which results in <2 ppb of drift (bellow the noise of the instrument). The instrument was zeroed using a bottled supply of UZA and periodically calibrated on the ground between flights with a high-precision NOAA ESRL standard.

2.4.5 Aerosol Composition

Cations, anions, organic acids, and carbohydrates were measured using a Particle-into-Liquid Sampler (PILS) coupled with a fraction collector. This system allows for the collection of liquid samples for offline analysis by ion chromatography. The PILS collects ambient particles into purified water. After particles are grown inside the body of the PILS by mixing the cool airflow with hot steam, the particles are collected by an impactor, and then washed off by a continuous flow of liquid passed over the impactor, providing a liquid sample for analysis (Orsini et al., 2003). The PILS sampled from the NCAR-University of Wyoming Aerosol Inlet mounted to the roof of the King Air (Snider et al., 2018). The PILS size-cut was provided by a non-rotating MOUDI impactor stage with a 50% transmission efficiency at 1 atmosphere ambient pressure of 1 μm (PM1) (Marple et al., 1991). The flow rate for the PILS was 15 LPM pulled off of the main aerosol inlet line. Sodium carbonate and phosphorous acid-coated denuders were placed upstream of the PILS to remove gaseous interferences. A valve upstream of the PILS was manually closed for 10 min forcing the airflow through a HEPA filter to obtain a measurement of the background in near real-time.

The liquid sample from the PILS was sent to a Brechtel Fraction Collector to collect samples for offline analysis (Sorooshian et al., 2006). The PILS liquid flowrates were set and the fraction collector operated similar to the approach used during WE-CAN (Western Wildfire Experiment for Cloud Chemistry, Aerosol Absorption and Nitrogen) to obtain $\sim$1.2 mL of liquid sample every 2 min (Sullivan et al., 2022). Pre-loaded carousels were manually switched during flight. After each flight the vials were unloaded, recapped with solid caps, and transported to CSU in coolers with ice packs to be stored in a 2ºC cold room until analyzed.

Each fraction collector vial was brought to room temperature and analyzed for cations, anions, organic acids, and carbohydrates. In order to conserve sample and allow for analysis of all species, 300 μL aliquots were transferred to polypropylene vials for each analysis. Various ion chromatography techniques were employed and are briefly described below.

The cation analysis, which includes ammonium (NH_4^+), was conducted on a Dionex ICS-3000 ion chromatograph. A Dionex IonPac CS12A analytical column (3 x 150 mm) employing an eluent of 20 mM methanesulfonic acid at a flow rate of 0.5 mL min^{-1} was used. The injection volume was 190 μL with a complete run time of 17 min. The anions, which includes nitrate (NO_3^-), and organic acids were measured using a Dionex ICS-4000 capillary ion chromatograph. A Dionex AS11-HC capillary column with a potassium hydroxide gradient provided by an eluent generator at a flowrate of 0.015 mL min^{-1} was used for the separation. The complete run time was 65 min with an injection volume of 35 μL. A blank correction was necessary for the cations, anions, and organic acids. Therefore, their concentrations were corrected by using the average of all background samples collected during a specific flight. For all the species measured by these analyses, the LOD was 1 ng m^{-3}.

Levoglucosan was determined via high-performance anion-exchange chromatography with pulsed amperometric detection (HPAEC-PAD) using a Dionex DX-500 series ion chromatograph with an ED-50/ED-50A electrochemical cell. The cell included two electrodes: a pH-Ag/AgCl (silver/silver chloride) reference electrode and ‘’standard” gold working electrode. For the separation, a Dionex CarboPac PA-1 column (4 x 250 mm) employing a sodium hydroxide gradient was used. The injection volume was 100 µL with a complete run time of 59 min. More details on this method can be found in Sullivan et al. (2011a,b, 2014, 2019). Levoglucosan did not require background correction. The LOD for levoglucosan was determined to be less than approximately 0.10 ng m^{-3}.

2.5 Analysis Approach and Calculations

2.5.1 Near source emissions

We use three methods to estimate NH_3 emission ratios relative to CH_4 (NH_3 EmR) for targeted facilities. 1) We determine the average NH_3 normalized excess mixing ratio (NEMR) per horizontal plume transect (see **NH_3 normalized excess mixing ratios (NEMR)**). 2) We estimate NH_3 EmR from an Ordinary Least Square (OLS) slope calculated using the observed NH_3 and CH_4 mixing ratios within plume conditions (see **Ordinary least squares (OLS) regression**). 3) We determine the NH_3 EmR using the OLS slope that is refined by removing CH_4 mixing ratios associated with emissions from oil and gas operations (see **Linear regression analysis with multiple predictors to eliminate influence of CH_4 from oil and gas sources.**). All three methods utilize observations identified during transects 10 km or closer to the targeted facility. Figure A2 shows the UWKA flight tracks for the 12 flights targeting near-source emissions.

Transect identification

To estimate NH_3 EmR, we identified all plume transects within 10 km downwind of each facility (total of 232 transects: 156 for cattle facilities and 76 for dairy facilities). The transects are characterized by co-located enhancements with respect to background air for NH_3 and CH_4, as shown in Figure 2.1d. CH_4 can be considered a conserved tracer because its lifetime against oxidation by the hydroxyl radical (OH), which is its main sink process, is sufficiently long ($\sim$8.3 years) such that it does not undergo any significant loss process in the timescales relevant to this study (i.e., minutes to hours) (Holmes, 2018). Each of our transects includes at least 10 data points of background air or out-of-plume observations on either side of a plume which is necessary to calculate the enhancement of NH_3 and CH_4 used to calculate the NH_3 NEMR. Note that in some transects, background mixing ratios differed on each side of a plume.

We calculated the physical age of each intercepted transect downwind of the facility using the distance of the transect downwind from the facility divided by the average wind speed for that transect. We note that most of our intercepted transects fall within the first hour of physical age (see

Figure A3). We also estimated an emission time for each transect by subtracting the physical age for each transect from the average time at which that transect was sampled. A summary of these calculations is presented in Figure A4. The data collected during TRANS^{2}Am largely represent plumes that have been emitted between mid-morning to early afternoon.

We include transects up to 10 km downwind of a given facility for the NH_3 EmRs calculations described below. Table A1 and Figure A5 summarize how calculated values vary when they are based on different subsets of the data. Briefly, overall estimates of NH_3 EmRs are slightly higher (2 - 7 %) when they are based only on transects collected < 4 km downwind versus also including more data collected further downwind. Next, we describe the three methods used to calculate the NH_3 EmRs, including a detailed explanation of the regression model to isolate oil and gas CH_4 emissions from agricultural CH_4 emissions. Figure 2.4 shows a schematic of the methods used for the NH_3 EmR calculations.

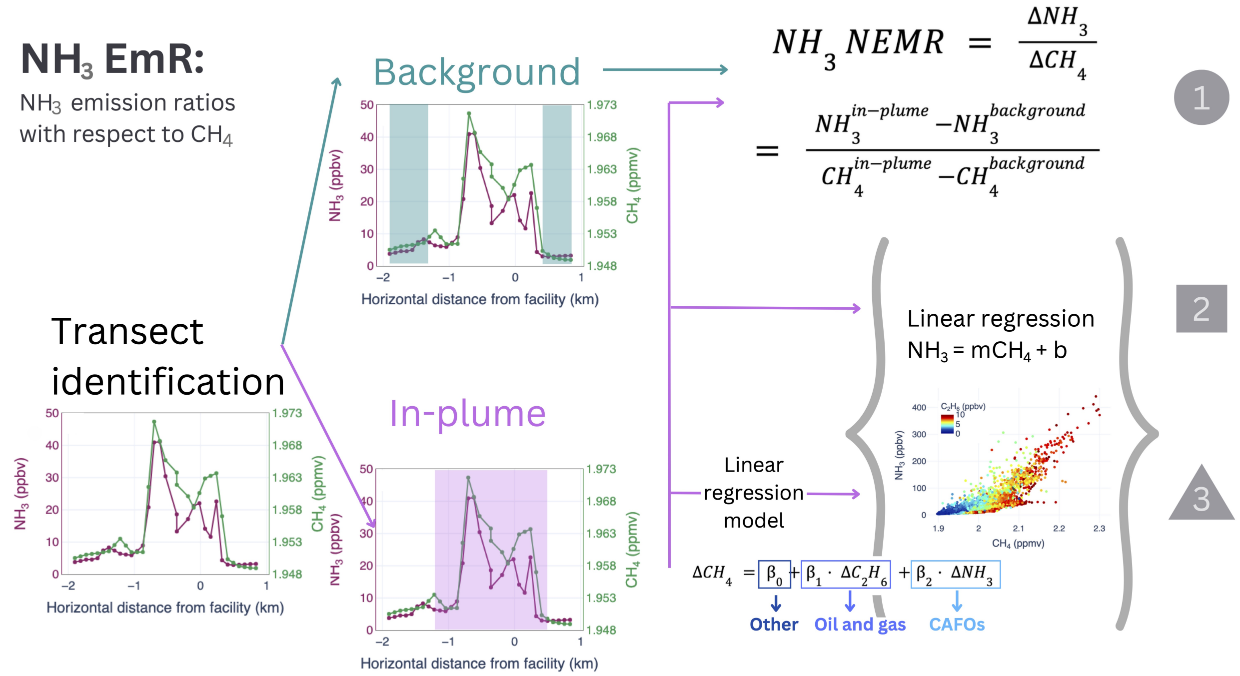

Figure 2.4: Schematic of the methodology used to calculate the NH_3 emissions ratios with respect to CH_4 (NH_3 EmR) showing the three methods presented in Figure 3.1.

NH_3 normalized excess mixing ratios (NEMR)

For each identified transect described above, we calculate the NH_3 NEMR using Eq. 2.1.

$$NH_3\,NEMR = \frac{\Delta NH_3}{\Delta CH_4} = \frac{\overline{NH_3^{in-plume}} - \overline{NH_3^{background}}}{\overline{CH_4^{in-plume}} - \overline{CH_4^{background}}} \tag{2.1}$$

In Eq. 2.1, transect-specific in-plume values are defined as the average of 1Hz observations where NH_3 is > the 25th percentile for that transect. Background values are defined as the average of the observations where NH_3 is < the 25th percentile. Using Eq. 2.1 results in one NEMR value for each transect. A sensitivity analysis using different backgrounds (see Figure A6) shows that choosing a lower percentile for background values (i.e., 5th percentile) might result in lower in plume average values, underestimating the NH_3 EmR by $\sim$5%. Calculating transect-specific NH_3 NEMRs allows us to look at each plume interception independently as a function of time of day, distance from a facility, and vertical location. Note that some of the analysis in this work uses NH_3 NEMR for individual transects rather than the average NH_3 NEMR within 10 km from the facility (i.e., NH_3 EmR).

Ordinary least squares (OLS) regression

We use the slope calculated from an ordinary least squares (OSL) linear regression of NH_3 versus CH_4 for the observations from all the transects within 10 km as one estimate of the NH_3 EmR. This method uses only in-plume observations. A sensitivity analysis of this method using both background and in-plume observation vs. only in-plume observations shows very similar results (Figure A7).

Linear regression analysis with multiple predictors to eliminate influence of CH_4 from oil and gas sources.

Given the close proximity of oil and gas operations to agricultural facilities, we used co- measured C_2H_6 to account for the influence of this potential additional CH_4 source. This is likely a more important issue for correctly interpreting aircraft observations than those collected by vehicles with close access to the perimeter of target facilities; however, Kille et al. (2017) was able to consistently quantify a positive C_2H_6 flux out of one of the three dairy sites they sampled using the CU Solar Occultation Flux instrument onboard a mobile vehicle.

Following Kille et al., (2018), we use the *linear model* module from the *sklearn python package* version 1.0.2 to perform a linear regression analysis to the time series of ΔCH_4 (Eq. 2.2) for each facility or group of nearby facilities sampled during each RF (see Table A2 for details). This method helps us account for or eliminate the percentage of CH_4 in each observation that is attributed to oil and gas operations in the time series selected for the analysis (Eq. 2.3-2.5). We use ΔC_2H_6 as the predictor for oil and gas emissions, ΔNH_3 as the predictor for agricultural (i.e, livestock) emissions, and ΔCH_4 as the predictand. This method assumes that oil and gas and livestock operations are the only sources of C_2H_6 and NH_3 in the region, respectively.

$$\Delta CH_4 = \beta_0 + \beta_1 \cdot \Delta C_2H_6 + \beta_2 \cdot \Delta NH_3 \tag{2.2}$$

The regressions coefficients β_1 and β_2 (ppbv ppbv^{-1}) represent the $\frac{\Delta CH_4}{\Delta C_2H_6}$ and $\frac{\Delta CH_4}{\Delta NH_3}$ ratios, respectively. The coefficient β_0 represents the excess CH_4 above the background that cannot be attributed to any of the two sources. All ΔX (CH_4, C_2H_6, or NH_3) have been calculated using a background, defined as the average of all the data below the 10^{th} percentile of the time series selected for the analysis. We note that using ΔX instead of absolute mixing ratios for each trace gas does not change the values for β_1 and β_2, it only changes the β_0 coefficient, which is related to the regional background selected. Table A2 shows details for the linear regression analysis, including the regression score, the regression coefficients, and the facilities name and RF that are included in the analysis. We only used model outputs with regression scores (R^2) above 0.4. Once β_0, β_1, and β_2 have been defined from the linear regression model, we use them to calculate the percentage contribution from each emission source (β_0= other/unexplained CH_4 above regional background, β_1= CH_4 from oil and gas, and β_2= CH_4 for agricultural emissions) for each 1-Hz CH_4 observation using Eqs. 2.3 - 2.5. An example of the percentage contribution from each emission source to CH_4 is shown in Figure A8 for the same transect shown in Figure 2.1d.

$$\%Other = \frac{\beta_0}{\beta_0 + \beta_1 \cdot \Delta C_2H_6 + \beta_2 \cdot \Delta NH_3} \times 100 \tag{2.3}$$

$$\%Oil\ and\ gas = \frac{\beta_1 \cdot \Delta C_2H_6}{\beta_0 + \beta_1 \cdot \Delta C_2H_6 + \beta_2 \cdot \Delta NH_3} \times 100 \tag{2.4}$$

$$\%Agriculture = \frac{\beta_2 \cdot \Delta NH_3}{\beta_0 + \beta_1 \cdot \Delta C_2H_6 + \beta_2 \cdot \Delta NH_3} \times 100 \tag{2.5}$$

Emission rate calculations

We calculated NH_3 emission rates in grams of NH_3 per hour per head of cattle (g $NH_3 \cdot h^{-1} \cdot hd^{-1}$) for four facilities (F01, F04, F19, F27/28) sampled under ideal wind conditions (i.e., winds > 4 ms^{-1}) with a consistent direction, sampling boxes located perpendicular to the wind direction, and minor influence from other emission sources (i.e., other feedlots or dairies)) following the methods by Hacker et al. (2016). The reference frame of the plumes was rotated using the prevalent wind direction to minimize the crosswind component and maximize the perpendicular wind component. We used different downwind sections (i.e., curtains) of each plume to get multiple independent emission rate estimates per facility (i.e., Figure 2.1c shows three transects (i.e., curtains) collected downwind of F01 and Figure 3.4a shows seven transects collected downwind of F04). The 1-Hz data, including calculated instant fluxes (μg $NH_3 \cdot m^{-2} \cdot s^{-1}$ - instantaneous P, T conditions) were averaged to a 200 × 100 m (horizontal × vertical) grid. We assume that the layer near the surface is the same as the data collected at the lowest sampled layer (e.g., ~150 - 300 m agl) corrected by the average topography in each grid cell. We assume that relevant concentration values at the top of the planetary boundary layer height (PBLh) were 10% of the highest available sampled altitude. The PBLh was calculated using potential temperature, water, and wind vertical profiles during descent while approaching the target facilities, following similar methods detailed in Cazorla and Juncosa (2018). We apply a simple linear interpolation (smooth factor = 1) to complete grids without observations. Finally, we integrated the instant fluxes across the total curtain area to obtain a total emission rate per facility at different distances. The maximum animal capacity per facility is based on a livestock registration and permitting database maintained by the Colorado Department of Public Health and Environment (CDPHE, 2017).

2.5.2 Near source evolution

We use five NH_3-rich agricultural plumes sampled during TRANS^{2}Am Phase I and II corresponding to three facilities: F01 sampled during RF09, F04 sampled during RF13 and F27/28 sampled on three different days (RF11, RF19, RF22) to study the fate of the NH_3 emitted from large animal feeding facilities. We chose these plumes for this analysis because they have 1) enhancements of NH_3 detectable up to or beyond 20 km, 2) minor influence from other emission sources downwind of the target facility, and 3) a consistent wind direction throughout the sampling time. High resolution (1-Hz) measurements of NH_3 and CH_4 mixing ratios and meteorological parameters (i.e., wind components, temperature, pressure) were used to calculate the mass conductances (J) (i.e., horizontal fluxes) across each "curtain" downwind of the facility (see **Mass conductance and NH_3 fluxes**). C_2H_6 was used to correct CH_4 for any oil and gas influence. Figures 2.2a - 2.2e show the NH_3 plumes sampled during RF09, RF11, RF13, RF19, and RF22 up to $\sim$25 km downwind of large beef cattle facilities.

Mass conductance and NH_3 fluxes

Under the assumption of mass conservation, for a domain with no net convergence or divergence of air masses, the domain-integrated mass conductance (J) should be conserved for non-depositing species (e.g., CH_4) (Lassman et al., 2020). The relative change in the mass conductance of NH_3 to CH_4 ($\frac{J_{NH_3}}{J_{CH_4}}$), can provide insights into the loss processes of NH_3 within the domain.

$$J = \int_{z=0}^{z=PBLh} \int_{y=0}^{y} \Delta C(x,y,z) \cdot V_p(x,y,z) \cdot \, dy \, dz \tag{2.6}$$

In Eq. 2.6, ΔC refers to the background corrected concentration of NH_3 or CH_4 in units of μg m^{-3} and V_p is the perpendicular wind component in units of m$\cdot s^{-1}$. The mass conductance (J) is the horizontal instantaneous rate of mass flow across a plane normal to the mean wind ($\Delta C \cdot V_p$) for each species (NH_3 or CH_4) integrated over the vertical and horizontal domain for each ”curtain” downwind of the facility (Hecker et al., 2016). J was calculated using subsets of measurements from curtains within x = 5 km bins downwind of the targeted facility. This means there is a J estimate between 0 km <= x < 5 km, 5 km <= x < 10 km, and so on. To assess the relative change in $\frac{J_{NH3}}{J_{CH4}}$ downwind of the targeted facility, we use the normalized value of $\frac{J_{NH3}}{J_{CH4}}$ at ”curtain” (x = i) with respect to $\frac{J_{NH3}}{J_{CH4}}$ from the first ”curtain” (x = 1) as shown in Eq. 2.7.

$$Fraction\ of\ NH_3\ remaining\ in\ the\ atmosphere\ (x=i) = \frac{\frac{J_{NH3}}{J_{CH4}}(x=i)}{\frac{J_{NH3}}{J_{CH4}}(x=1)} \tag{2.7}$$

Finally, to calculate the $\mathrm{NH_3}$ deposition ($-F_{NH_3}$) or emission (F_{NH_3}) flux between each curtain, we use the *Fraction of NH3 remaining in the atmosphere* in ”curtain” x = i normalized to the *Fraction of NH3 remaining in the atmosphere* in the previous ”curtain” x = i - 1 multiplied by J from ”curtain” x = i - 1 as shown in Eq. 2.8.

$$F_{NH_3}(x=i) = J_{NH_3}(x=i-1) \times \left[1 - \frac{Fraction\ of\ NH_3\ remaining\ (x=i)}{Fraction\ of\ NH_3\ remaining\ (x=i-1)}\right] \tag{2.8}$$

The error for the calculated fluxes (Eq. 2.8) include i) 20% uncertainty for the NH_3 mass conductance (J_{NH3}), which includes the uncertainty of the NH_3 measurements (set at 12%) and 15% error from transect identification and other measurements errors (i.e., wind); and ii) the difference in J_{NH3}/J_{CH4} values when time correction was or was not applied (see Figure 4.4) and a 5% variability in J_{NH3}/J_{CH4} with respect to different boundary conditions.

Other details on how these calculation were performed follow:

- The reference axis of the plumes was rotated based on the predominant wind direction to minimize the cross-wind component (V_c) and maximize V_p.
- High-resolution mixing ratios of NH_3 and CH_4 (1Hz) were converted to concentration (μg m^{-3}) using the corresponding molecular weight and the observed temperature and pressure.

- In order to calculate transect-specific agricultural CH_4 (CH_{4_ag}), we use linear regression with multiple predictors for each transect (see Section 2.5.1) as in Kille et al. (2019). ΔC_2H_6 and ΔNH_3 were used as predictors for oil and gas and agriculture, respectively. This model is strongest near sources and becomes more uncertain as a plume moves downwind.

- We use a transect-specific background corrected mixing ratio for each species (ΔNH_3, ΔCH_4, ΔCH_{4_ag}, ΔC_2H_6) for the linear regression model with multiple predictors and to calculate ΔC. For the near-source evolution, the transect-specific background was defined as the average of the mixing ratios within a given transect below the 10^{th} percentile. A sensitivity analysis of the backgrounds using 20^{th} and 30^{th} percentile shows an average of 5 - 10% difference in the final J_{NH_3} and $J_{CH_{4_{ag}}}$.

- The 1Hz data is averaged into boxed 200 m wide and 100 m tall for each "curtain".
  - To complete $\Delta C \cdot V_p$ in the boxes near the surface, we used $\Delta C \cdot V_p$ from the lowest available layer (e.g., 100 m or 200 m above the surface) and corrected them by the percentage of topography in the surface box. Because of uneven topography in the region, the height of the boxes (z) at the surface might vary as a function of the topography. If a box near the surface included 20 m of terrain elevation, the corresponding $\Delta C \cdot V_p$ would be 80% of that from the closest available layer directly above it.
  - The boxes at the top of the PBL were completed using the $\Delta C \cdot V_p$ from the highest available layer and a decay rate of -0.76 ppbv/250 m and -0.67 ppbv/250 for NH_3 and CH_{4_ag}, respectively, based on the vertical profiles in Figure A.9.
  - To complete the rest of the empty boxes, we used simple a linear interpolation (*scipy.interp1* smooth factor = 1).
  - All negative $\Delta C \cdot V_p$ were excluded from the analysis. Negative values were infrequent and resulted from either background subtraction or negative wind components.

2.5.3 Upslope transport

Hysplit trajectories

We use the Hybrid Single Particle Lagrangian Integrated Trajectory (HYSPLIT) model (Draxler and Hess, 1998) to identify the origin of the NH_3 plumes observed in L3 and L4. We also use the trajectories to estimate the transport time of NH_3-rich plumes from their sources to where the UWKA observed them in L3 and L4. We initialized ensemble sets (27 trajectories) of forward and backward trajectories using the High-Resolution Rapid Refresh (HRRR) meteorological product. The HRRR dataset has a time step of 1 hour, a 3 $\times$ 3 km grid spacing, and 36 sigma-level layers between 1 and 0.0124. Our trajectories were initialized for a period of 6 hours at the center point of sharp NH_3 enhancements within each leg. Each trajectory was initialized at the same altitude as the UWKA. The trajectories that contacted the surface (i.e., altitude of 0 m) were excluded from the analysis. The total distance error of the trajectories is reported to be 15 - 30$\%$ of the total time traveled.

Chapter 3

Summertime airborne measurements of Ammonia emissions from cattle feedlots and dairies in northeastern Colorado

3.1 Emission Ratios for Cattle Feedlots and Dairies

Figure 3.1 shows NH_3 EmR for 29 facilities housing a) beef cattle or b) dairy cows sampled during Phase I of TRANS^{2}Am. Figure 3.1 shows that there is large variability in NH_3 EmR between different facilities. Specifically, beef cattle facilities have NH_3 EmR ranging from 0.1 to 2.6 (average 1.2) ppbv ppbv^{-1} and dairies have lower NH_3 EmR ranging from 0.2 to 0.5 (average 0.3 ppbv ppbv^{-1}). There is a significant difference between the average NH_3 EmR associated with beef cattle versus dairy facilities. During this study, the NH_3 EmR associated with dairies was on average, 4 times less than the NH_3 EmR associated with beef cattle (0.3 vs. 1.2 ppbv ppbv^{-1}). This difference has been observed previously (Eilerman et al., 2016). Factors that contribute to this pattern include differences in production (milk vs. beef), feeding products, and higher CH_4 emissions from dairies related to fresh manure/anaerobic lagoons within the feedlots (Miller et al., 2014; Eilerman et al,, 2016; Golston et al., 2020). In this dataset, dairy NH_3 EmR are less variable, but this could also be explained by the fewer observations. Note that the different methods used to calculate NH_3 EmR provide similar results with few exceptions. In general, those methods used to correct CH_4 emissions from other sources (i.e., NH_3 NEMR and OLS regression corrected for CH_4) produce similar values, but those values are higher than values produced using methods that do not correct for CH_4 emissions from other sources (OLS regression without correcting for CH_4) (see Figure A4 and A7). Differences in NH_3 EmR from facilities housing beef cattle vs. dairy cows could result from higher emissions of NH_3 from facilities housing beef cattle and/or higher CH_4 emissions from facilities housing dairy cows. A t-test of the distribution of NH_3 and CH_4 for

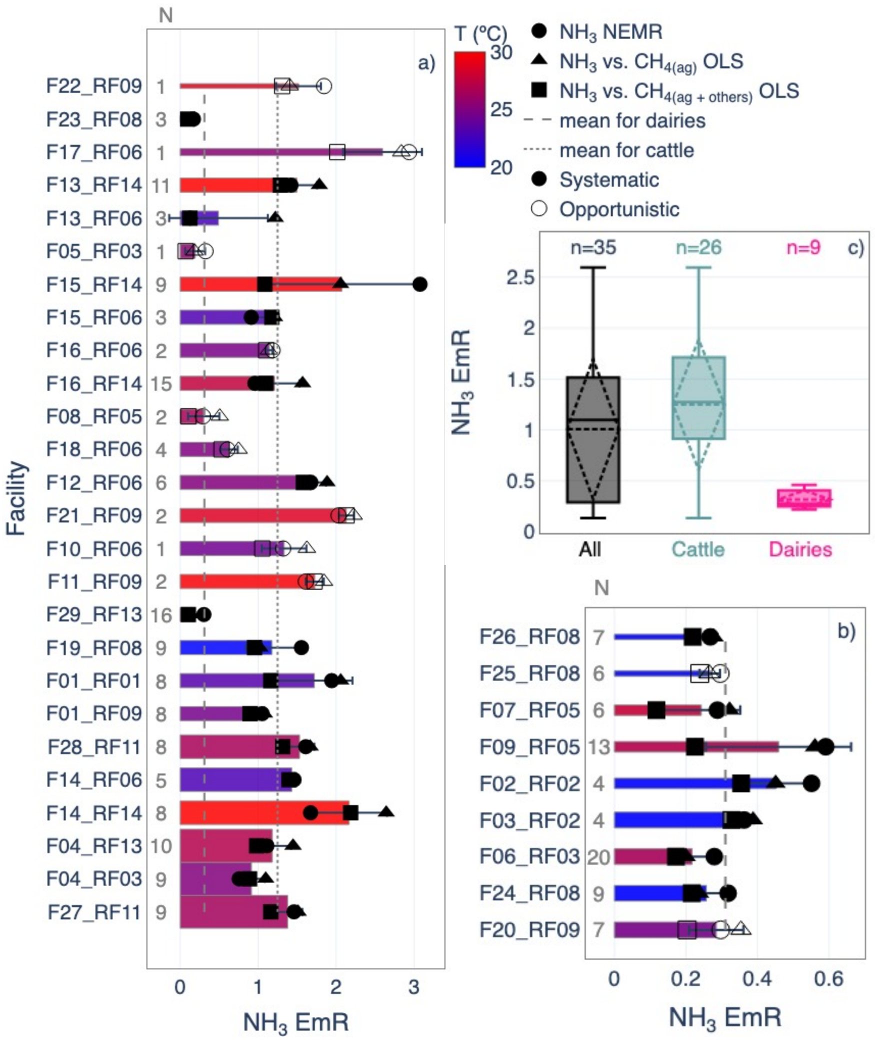

Figure 3.1: Average NH_3 emission ratios with respect to CH_4 (NH_3 EmR) for a) beef cattle and b) dairy facilities. NH_3 EmRs are calculated using all transects < 10 km from the targeted facility. The number of transects used are shown in gray to the left of the colored bars. Bars are colored by the average ambient air temperature (ºC) measured from the aircraft during the time of sampling, and bar width represents the maximum animal capacity reported (CDPHE, 2017). Bars with the smallest width represent those facilities for which there is no available information about animal capacity (N = 3, see Table 3.1 for more details). The different symbols represent different methods for estimating the NH_3 EmR. Circles indicate values calculated using the NH_3 NEMR method. Squares represent values calculated using in-plume observations and the OLS regression method (NH_3 vs. CH_4(ag+others) OLS); triangles indicate values calculated using the OLS regression method with the multiple-predictors linear regression method for isolating CH_4 emissions associated with agricultural sources (NH_3 vs. CH_4(ag) OLS). Error bars show the standard deviation between the three methodologies. Filled and open symbols show estimates for facilities sampled systematically and opportunistically, respectively. Note that those facilities sampled opportunistically (open symbols) do not follow the sampling strategy (i.e., spiral + boxes downwind) outlined in Section 2.3.1 and usually include only a few transects (1-4). The dotted and dashed lines in Figures 3.1a and 3.1b represent the average NH_3 EmR for beef and dairy cattle, respectively, during Phase I of TRANS^{2}Am. c) Average NH_3 EmR estimates for all facilities (black), separated by beef (blue) and dairy (pink).

facilities housing beef cattle and dairy cows shows that in this dataset, both are true (see Figure B1 and B2). Facilities housing beef cattle have higher mean NH_3 mixing ratios (25.4 vs. 12.3 ppbv) and lower CH_4 mixing ratios (1.978 vs. 1.984 ppmv) compared to dairies.

Table 3.1: Summary of facility information, meteorological conditions, NH_3 EmR, and emission rates for beef cattle [C] and dairy [D] facilities sampled during Phase I of TRANS^{2}Am.

Facility Name and Flight Number [animal type] C = Cattle D = Dairy	Lat (°)	Lon (°)	Animal Max. Capacity	T (°C)	RH (%)	Mean NH_3 EmR [std] (ppbv ppbv^{-1})	Emission rates [mean] ($gNH_3 \cdot h^{-1} \cdot hd^{-1}$)
F01_RF01 [C]	40.262	-103.543	42000	23	30	1.7 [0.5]	10, 16, 26 [17.3]
F01_RF09 [C]	40.262	-103.543	42000	25	45	1.0 [0.1]	No
F02_RF02 [D]	40.569	-104.612	9742	19	54	0.5 [0.1]	No
F03_RF02 [D]	40.574	-104.696	13150	19	54	0.4 [0.03]	No
F04_RF03 [C]	40.378	-104.510	100100	25	27	0.9 [0.2]	No
F04_RF13 [C]	40.378	-104.510	100100	27	32	1.2 [0.2]	18, 7.5, 29, 10, 16, 8.5, 4 [11.8]
F05_RF03 [C]	40.307	-104.610	15000	26	27	0.2 [0.1]	No
F06_RF03 [D]	40.450	-104.485	13384	27	24	0.2 [0.1]	No
F07_RF05 [D]	40.604	-104.950	4235	28	23	0.2 [0.1]	No
F08_RF05 [C]	40.758	-104.976	25024	27	19	0.3 [0.2]	No
F09_RF05 [D]	40.839	-104.978	7500	27	17	0.5 [0.2]	No
F10_RF06 [C]	40.512	-103.325	30024	24	25	1.3 [0.3]	No
F11_RF09 [C]	40.512	-103.325	30024	30	32	1.7 [0.1]	No

F12_RF06 [C]	40.580	-103.309	30000	25	28	1.7 [0.2]	No
F13_RF06 [C]	40.761	-103.127	10500	23	33	0.5 [0.6]	No
F13_RF14 [C]	40.761	-103.127	10500	30	16	1.5 [0.3]	No
F14_RF06 [C]	40.781	-102.966	65100	23	35	1.4 [0.03]	No
F14_RF14 [C]	40.781	-102.966	65100	31	20	2.2 [0.5]	No
F15_RF06 [C]	40.832	-102.933	20012	23	36	1.1 [0.2]	No
F15_RF14 [C]	40.832	-102.933	20012	30	22	2.1 [1.0]	No
F16_RF06 [C]	40.660	-103.170	22030	25	32	1.1 [0.04]	No
F16_RF14 [C]	40.660	-103.170	22030	28	24	1.2 [0.3]	No
F17_RF06 [C]	40.706	-103.248	10000	25	28	2.6 [0.5]	No
F18_RF06 [C]	40.632	-103.316	28000	25	27	0.6 [0.1]	No
F19_RF08 [C]	40.165	-104.132	35000	19	93	1.2 [0.3]	13, 6, 10 [9.6]
F20_RF09 [D]	40.336	-103.475	17000	25	44	0.3 [0.1]	No
F21_RF09 [C]	40.580	-103.309	30000	29	35	2.1 [0.1]	No
F22_RF09 [C]	40.590	-103.306	NA	29	33	1.5 [0.3]	No
F23_RF08 [C]	40.206	-104.112	9510	17	83	0.1 [0.04]	No
F24_RF08 [D]	40.265	-104.123	14066	18	77	0.3 [0.1]	No
F25_RF08 [C&D]	40.244	-104.074	NA	19	77	0.3 [0.03]	No
F26_RF08 [D]	40.241	-104.000	NA	17	81	0.3 [0.03]	No
F27_RF11 [C]	40.116	-102.585	125150	26	35	1.4 [0.2]	16, 17, 15.5, 21, 15.5 [17]
F28_RF11 [C]	40.178	-102.568	54060	27	35	1.5 [0.2]	16, 17, 15.5, 21, 15.5 [17]
F29_RF13 [C]	40.438	-104.600	34020	25	41	0.2	No

Table 3.2: Comparison of molar emission ratios and emission rates in the Colorado Front Range from previous publications

Study	Mean NH_3 NEMR (error where reported) (ppbv $ppbv^{-1}$)	Mean Emission rate (gNH^3 h^{-1} hd^{-1})	Number of facilities
Cattle			
This study	1.2 (range = 0.1 - 2.6)	4 - 29	20/4
Eilerman et al. (2016)	0.23 (+0.20/-0.11)		1
Golston et al. (2020)	0.25 (±0.03)	2.27 ±0.23	15
Kille et al. (2017)		12 ±2.8	1
Shonkwiler and Ham (2018)		3.33 ±1.63	1
Sun et al. (2015)		2.64 ±0.26	2
Pollack et al. (2022)	0.8 - 2.7		4
Dairy			
This study	0.3 (range = 0.2 - 0.5)		9
Eilerman et al. (2016)	0.14 (+0.13/-0.07) 0.17 (+0.08/-0.05)		2
Golston et al. (2020)	0.14 (±0.02)	5.33 ±0.49	25
Kille et al. (2017)		11.4 ±3.5	3

Table 3.2 compares NH_3 EmR (and fluxes see Section 3.4) observed in our study to prior observations in the Colorado Front Range. There are several key points from this comparison. 1) Our calculated NH_3 EmR are higher than both Eilerman et al. (2016) and Golston et al. (2020) for both cattle and dairy facilities. This is only partially explained by the time of day of our sampling. The vast majority of the sampling occurred between 10 AM and 3 PM LT when the diurnal profile of NH_3 EmR typically peaks (see Eilerman et al. (2016), Golston et al. (2020) and Section 3.2). However, a close comparison to the work of Golston et al. (2020) indicates that we observed higher NH_3 EmR during the afternoon peak in NH_3 emissions. Our average values are also higher than those reported in Eilerman et al. (2016) for summer only and for cattle specifically. 2) Prior to the sampling by Golston et al. (2020), estimates of NH_3 EmR in this region were limited to a handful of facilities. Our dataset represents a dramatic increase in the number of facilities that can be used to estimate NH_3 EmR. While each prior study cited in Table 3.2 indicates a substantial step forward

in terms of its technical and/or methodological approach, more observations are likely still needed to account for the true variability in NH_3 EmR, particularly outside of the warm summer months.

3.2 Temperature Dependencies

In general, Figure 3.1 shows that the highest NH_3 EmR observed during Phase I of TRANS^{2}Am were associated with the highest temperatures. Figure 3.2 explores the relationship between NH_3 EmR and temperature further. Figure 3.2 shows the NH_3 EmR estimates as a function of temperature (ºC) and relative humidity (%) for beef cattle (top panel) and dairy cows (lower panels). Panels a) (cattle) and c) (dairy) show the range of temperature and relative humidity of the data presented here, colored by NH_3 EmR and sized by facility maximum capacity. Panels b) (cattle) and d) (dairy) show NH_3 EmR vs. temperature colored by relative humidity.

NH_3 EmR for beef cattle generally increases with increasing temperatures, consistent with prior work documenting an exponential relationship between NH_3 EmR and temperature for livestock facilities (Eilerman et al., 2016; Golston et al., 2020). In general, we observe a weak overall relationship between NH_3 EmR estimates and temperature for facilities housing beef cattle. The relationship between NH_3 EmR and temperature is especially hard to assess for the few NH_3 EmR estimates for dairies (panel d). Note that TRANS^{2}Am collected data in a small range of temperatures compared to those observed year-round in Colorado (Figure 3.2 panels a) and c)). Most of the data were collected during hot and dry conditions, and few observations were collected during hot and humid conditions, usually after precipitation events. Broadly consistent with our findings, the data presented in Golston et al. (2020) that was collected at temperatures $> \sim 25$ °C also shows a large spread in NH_3 EmR ranging from near 0 up to almost 2 ppbv ppbv^{-1}. In both datasets, variability in NH_3 EmR appears larger in this uppermost temperature range.

The observed relationship between NH_3 EmR and temperature for beef cattle facilities is shown with the dashed line in panel b). The temperature dependence of NH_3 emissions was derived using the principle that volatilization of NH_3 increases with higher temperature (Eilerman et al., 2016, Sutton et al., 1994, Sander et al., 1999). Briefly, the NH_3 compensation point for volatilization

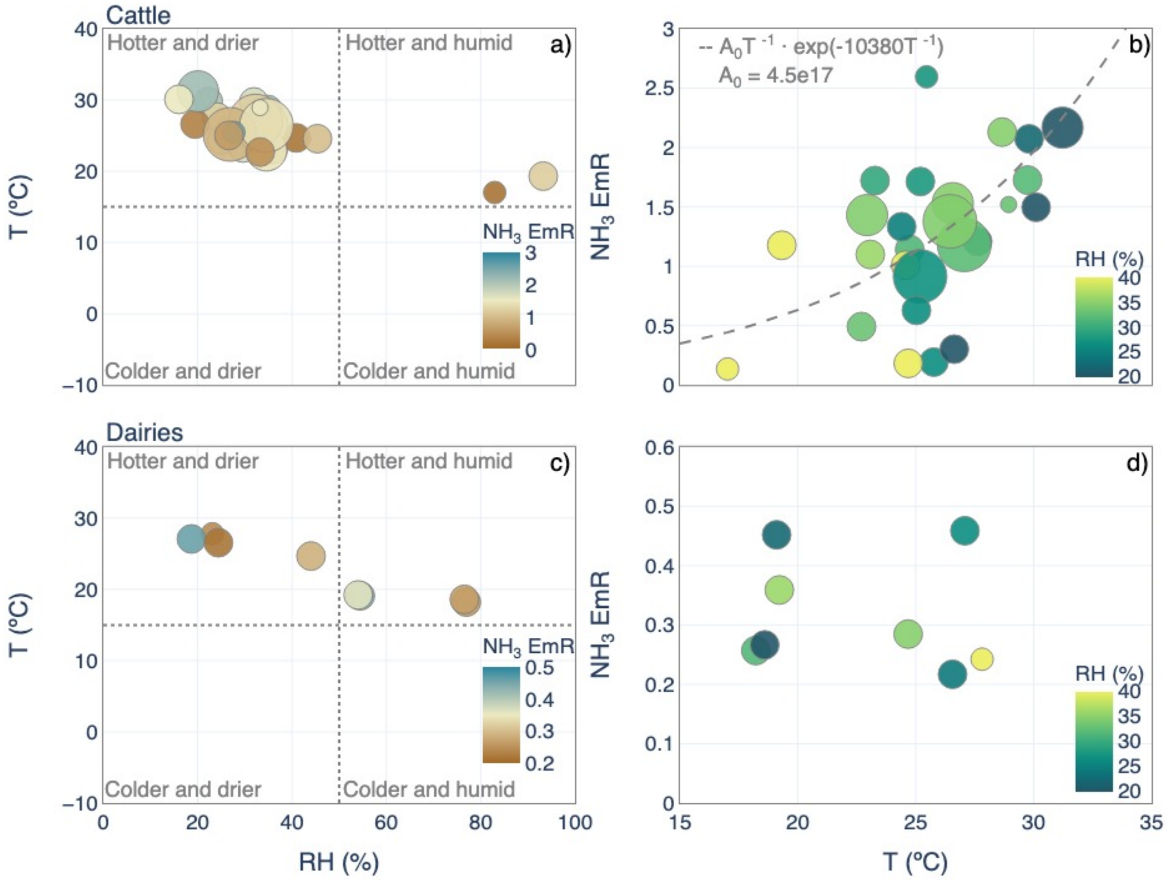

Figure 3.2: NH$_3$ EmRs (ppbv ppbv^{-1}) estimates for individual facilities as a function of temperature and relative humidity for beef cattle (top panels) and dairy cows (lower panels).

varies as a function of temperature and pH of the solution, both unknown for this dataset. Here, we have used atmospheric temperatures as a proxy for soil temperature and coefficients that remain mostly constant with temperature and pH, allowing for a semi-empirical fit of the observations to the model (see Eq. 2.9 and Eq. B.1 for more details). Panel b) shows that one of the highest estimated NH_3 EmR corresponds to the highest temperatures and lowest relative humidity in the range of observations (i.e., 2.2 ppbv ppbv^{-1}, 31 ºC, 21%). However, we observed a larger NH_3 EmR (i.e., $\sim$2.6 ppbv ppbv^{-1}) from an opportunistic sample at a lower temperature and higher relative humidity (i.e., 25 ºC, 27%). Pollack et al. (2022) report NH_3 EmR estimates during November 2019 under colder conditions (median of 15 ºC) for five beef cattle facilities in the same study region. Their estimates range from 0.8 to 2.7 ppbv ppbv^{-1}. Similar to what Eilerman et al. (2018) observed, this suggests that large NH_3 EmR exist under colder conditions.

The few samples associated with lower temperatures (purple bars in Figure 3.1), higher relative humidities, and lower NH_3 EmR (i.e., facilities sampled during RF02 and RF08) were collected after regional precipitation events. Overall, most of the reduced nitrogen (NHx = NH_3 + NH_4^+) in the near-source sampling is found in the gas phase as NH_3 (see Figure B3). Figure B3 shows that the partitioning of NH_3 to the particle phase as NH_4^+ is, on average, less than 15% of the total NHx for the data presented in this study. The few exceptions (RF02, RF03, and RF08) are those sampled after precipitation events which, in general, have lower NH_3 mixing ratios (see Figure B4). In order to further explore the relationship between NH_3 emissions and temperature and based on previous observations that found a strong correlation between NH_3 emissions and time of the day (Eilerman et al., 2016), Figure 3.3 shows transect-specific NH_3 NERM as a function of sampling time.

Figure 3.3 shows a diurnal pattern of NH_3 NEMR with higher values in the mid-afternoon and lower values in the morning and evening periods. The highest NEMRs were observed between 12 and 4 PM. More quantitative information can be drawn from Figure 3.3 by examining some of the specific flights where that same facility was repeatedly sampled at different times and temperatures. F13, F14, F15, and F16 were sampled during both RF06 (pink dots in Figure 3.3) and RF14 (dark purple dots in Figure 3.3). RF06 was a mid-morning flight (10 AM - 1 PM) with average plume

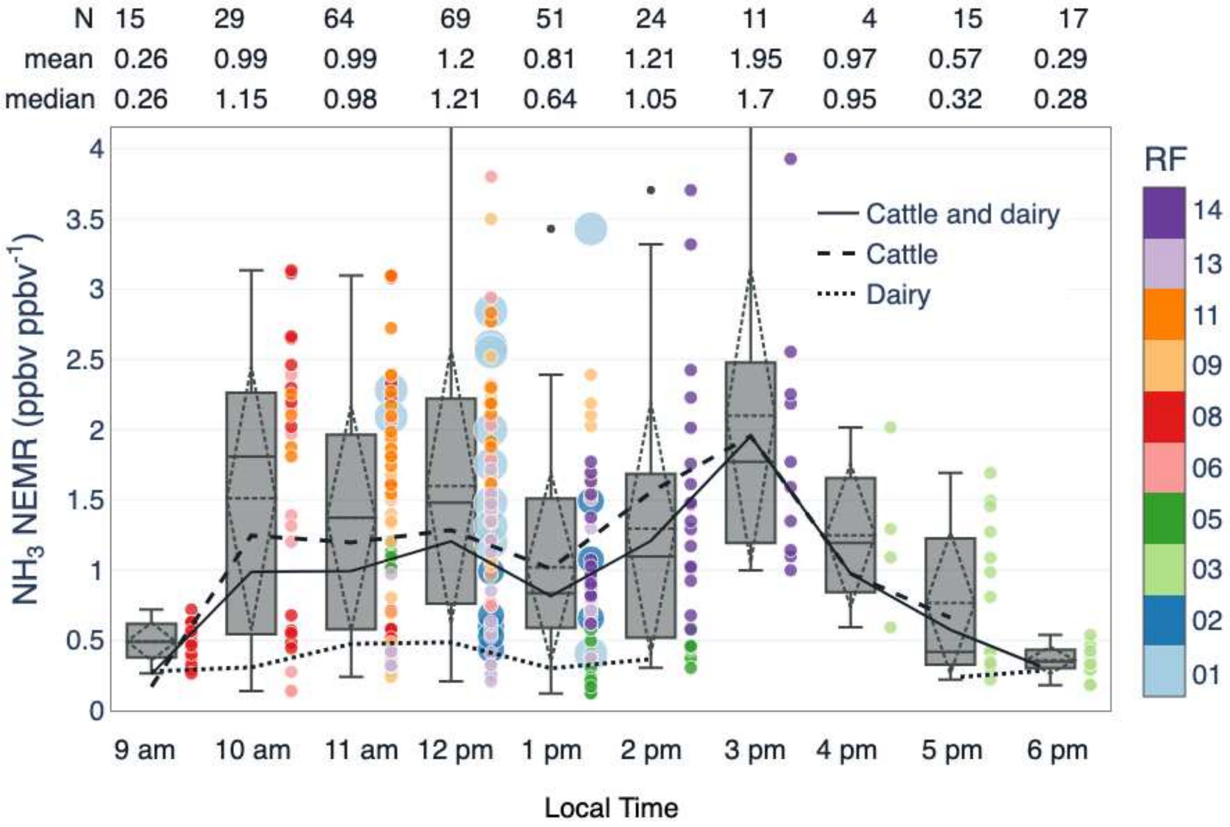

Figure 3.3: Transect-specific NH_3 NEMR as a function of local sampling time. The points represented by the boxplots are colored by research flight (RF). Points for RF01 (light blue) and RF02 (dark blue) were made larger intentionally to prevent masking from other data points. The lower and upper ends of the boxes span from quartile 1 (Q1) to quartile 3 (Q3). The whiskers correspond to each box edge (Q1 or Q3) ±1.5 the interquartile range (IQR: Q3-Q1). If no outliers are present, the whiskers represent minimum and maximum values. The dashed rhombuses show the sample mean (middle line) and the standard deviation (corners). N indicates the number of transects in each box plot. Note that all transects, including those >10 km and all animal types, have been included.

interception temperatures and relative humidities of $\sim$23 ºC and 34%. RF14 was an afternoon flight (1 PM - 4 PM) with average plume interception temperatures and relative humidities of $\sim$30 ºC and 21%. The NH_3 EmR estimates for these four facilities are 0.14 - 1.06 ppbv ppbv^{-1} higher for RF14 (hotter and drier) than they are for RF06 (colder and more humid). F04, one of the biggest facilities sampled during Phase I of TRANS^{2}Am (see Figure 6 for details), was sampled during RF03 (light green dots in Figure 3.3) and RF13 (light purple dots in Figure 3.3). RF13 was a midmorning flight (10 AM - 2 PM) with higher average temperature and relative humidity than RF03 (27 vs. 25 ºC and 31 vs. 27%), a late afternoon flight (4 - 6 PM). The NH_3 EmR were higher during RF13 (hotter and more humid) than RF03 by 0.27 ppbv ppbv^{-1}.

We also observed one case where higher temperatures did not produce a higher NEMR for a given facility. F01 was sampled twice (RF01 (light blue dots in Figure 3.3) and RF09 (light orange dots in Figure 3.3)) at roughly the same time of the day; the average temperature was slightly higher during RF09 (24.5 ºC) than during RF01 (23.2 ºC). However, the relative humidity was considerably higher during RF09 (45%) than during RF01 (30%). Despite a similar time of day and temperature range, NH_3 EmR estimates are lower for RF09 than they are for RF01 (1.00 vs. 1.972 ppbv ppbv^{-1}), suggesting that drier conditions favor NH_3 volatilization and emissions. The NH_3 emissions estimated for all these facilities and their differences in the context of different temperatures, relative humidities, and sampling times reflect the variability of NH_3 emissions for the same facility and their dependency on temperature, relative humidity, and time of day.

3.3 Plume Evolution Case Study

Loss of gas-phase NH_3 in plumes advected from feedlots can occur from dry deposition or chemical transformation of NH_3 to particle NH_4^+. Under the assumption of constant emissions relative to CH_4 and pseudo lagrangian sampling, we can use the ratio of NH_3 to CH_4 downwind of the CAFOs to constrain the loss of gas-phase NH_3, since both NH_3 and CH_4 are diluted similarly downwind of a source, but CH_4 does not undergo significant chemical losses in the temporal scales of this study (i.e., hours). Changes in the ratio of NH_3 to CH_4 downwind of the CAFOs can be

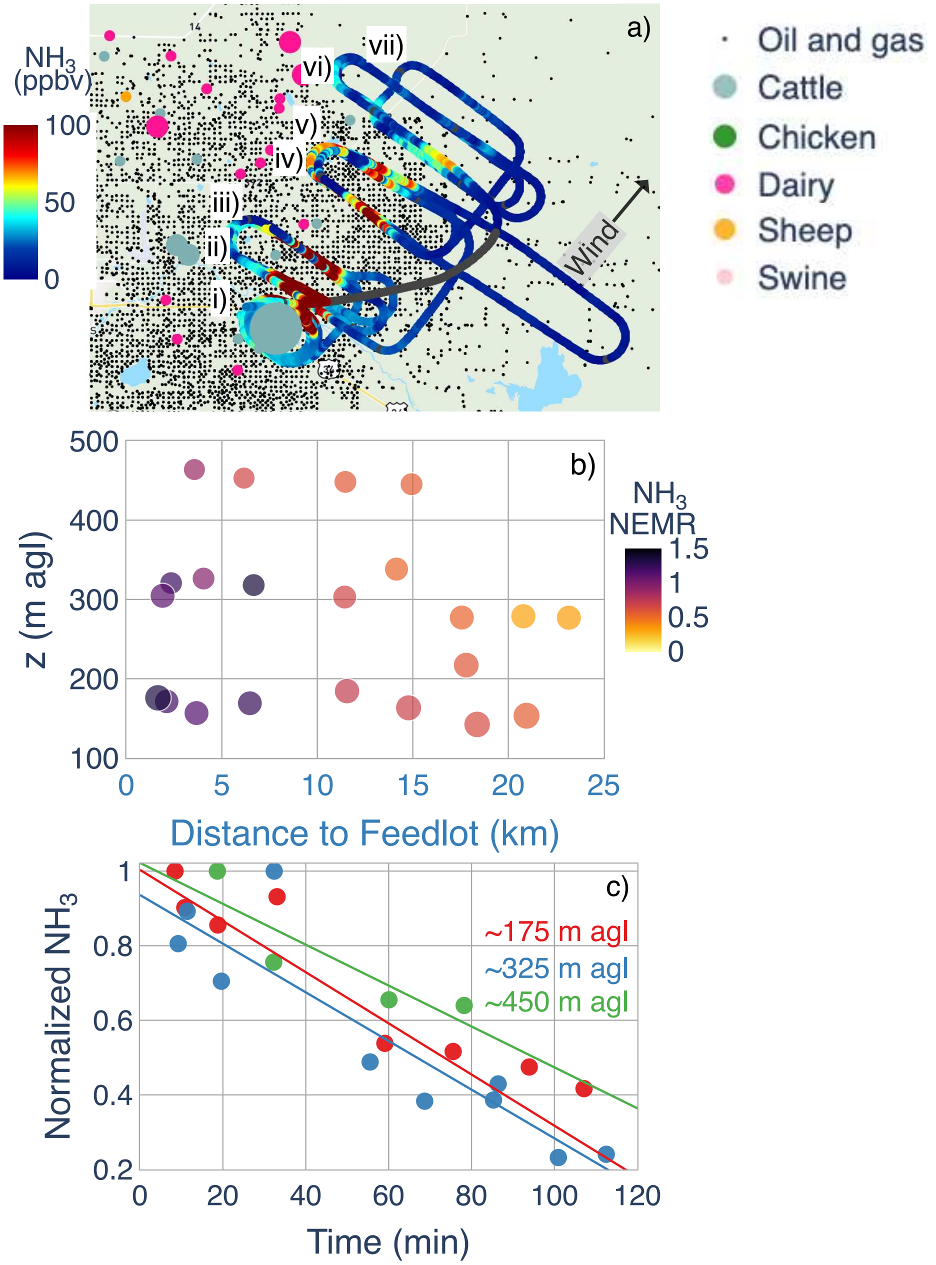

Figure 3.4: a) Flight track of the UWKA colored by NH$_3$ (ppbv) during sampling of F04 on 23 August 2021. As in Figure 3.1, the colored and sized dots represent agricultural facilities housing different animals, and the black dots signify oil and gas operations as of 2015. Letters (i - vii) refer to different vertical transects used for emission rate calculations (refer to Figure B16 for more information) b) Transect-specific NH$_3$ NEMR as a function of altitude above ground level (m agl) and distance downwind from the center of the facility (km). c) Normalized NH$_3$ NEMR with respect to the maximum value in each altitude bin (∼175, 325, 450 m agl) as a function of the traveled time since emission (in minutes). Traveled time is calculated as the distance of each transect from the targeted facility divided by the average wind speed for that transect. Lines signify the linear fit for each altitude bin. E-folding time (time at which normalized NH$_3$ NEMR drops below 1/e) was determined by the linear fit.

used to calculate the total loss of NH_3 due to deposition or partitioning to the gas-phase (Lassman et al., 2020).

Across the dataset presented in this chapter, we identified only one instance with substantial decay of NH_3 beyond 10 km from the facility: F04 during RF13. Note that the plume downwind of this facility did not decay similarly on the other sampling day (i.e., RF03). F04 was sampled on 23 August 2021, between 12:30 and 2 PM LT. F04 is one of the largest facilities housing beef cattle sampled during TRANS^{2}Am, with a reported animal maximum capacity of 100,000 animals. The plume intercepted from F04 during the RF13 shows the largest NH_3 mixing ratios observed throughout Phase I of TRANS^{2}Am with values up to 440 ppbv of NH_3. The plume from F04 was intercepted up to 25 km downwind (Figure 3.4). The sampling included circles around the facility (as close as 2 km) and three distinct vertically stacked boxes at 4 - 6 km downwind, 11 - 14 km downwind, and 17 - 23 km downwind. The first two stacked boxes were executed at $\sim$175, 325, and 450 m agl. The last one was executed only at 175 and 325 m agl. The PBL on this day contained two inversions. The lowest inversion was identified at $\sim$500 m agl, and a second one was located at $\sim$1300 m agl (see Figure S12 for vertical profiles). Above the latter inversion, the BL appeared to be well-mixed. The maximum altitude that the aircraft reached was $\sim$2800 m agl, and thus characterization of the boundary layer above this altitude was not possible. In general, NH_3 NEMR decreased with distance from the facility after 10 km. The closest transects to the facility (at 175 and 325 m agl) have an average NH_3 NEMR of 1.11 (+/- 0.19 std). The furthest transects (175 and 325 m agl) have an average NH_3 NEMR of 0.301 (+/- 0.06). The calculated e-folding time for NH_3 NEMR at 175, 325, and 450 m agl are 108, 87, and 119.3 minutes, respectively. These estimates are not likely independent due to PBL mixing within the lower boundary layer.

3.4 NH_3 Emission Rates

Figure 3.5 shows inferred NH_3 emission rates for F01 during RF01, sampled from 3 distances downwind. The inferred emission rate magnitudes vary from 10 to 26 g $NH_3 \cdot h^{-1} \cdot hd^{-1}$ depending on where the calculation is performed. NH_3 inferred emission rates for F01, F04, F19 and F27/F28

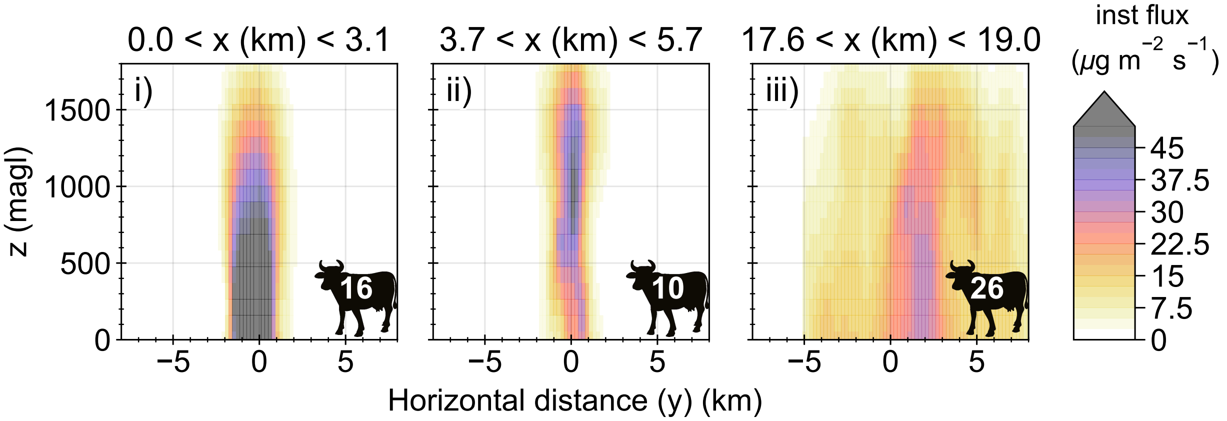

Figure 3.5: Example NH_3 emissions rates determined for F01 sampled during RF01 via transects at downwind distances of a) 0 - 3.1 km, b) 3.7 - 5.7 km, and c) 17.6 and 19 km. The colorbar shows inferred instantaneous horizontal fluxes in each grid cell in μg NH_3 m^{-2} s^{-1}. Grid cells are 200 (horizontal) x 100 (altitude) m. The number in the lower right corner shows the total inferred emission rates in g $NH_3 \cdot h^{-1} \cdot hd^{-1}$. Panels show simple linear interpolation using the python package *scipy.interpolate*, with a smooth factor of 1.

range from 4 - 29 g $NH_3 \cdot h^{-1} \cdot hd^{-1}$. The average (std) is 14.4 (6.62) g $NH_3 \cdot h^{-1} \cdot hd^{-1}$. All these facilities house beef cattle. Similar to the example shown in Figure 3.5 (F01), the estimated NH_3 emission rates for F04, F19, and F27/28 depend on where the calculation is performed downwind from each facility. In general, there is not a consistent relationship between NH_3 emission rate and distance downwind (see Figure B6). For more details, refer to Table 1 and Figures B7 - B9. The emission rates for F27 and F28 are combined estimates since these facilities are within ~8 km of each other, and their plumes merged during sampling. Note that the NH_3 emission rates estimates for F04 during RF13 are presented for curtains >10 km from F04, where substantial NH_3 loss was observed (see Figure 3.4). If the curtains > 10 km are not included, the average NH_3 emission rate for F04 during RF13 increases from 11.8 to 17 g $NH_3 \cdot h^{-1} \cdot hd^{-1}$ which is closer to the estimates of the other two larger facilities (F01 and F27/28). Unlike NH_3 emissions ratios, inferred NH_3 emission rates do not require correction for CH_4 emissions.

The average of our estimates is higher than those reported in previous studies (i.e., 2.64 - 12 g $NH_3 \cdot h^{-1} \cdot hd^{-1}$ (Golston et al., 2020; Kille et al., 2017; Sun et al., 2015; Shonkwiller and Ham, 2018)) with one exception that reports NH_3 emission rates 14 (±2) g $NH_3 \cdot h^{-1} \cdot hd^{-1}$ for one facility (F04 in this study) (McCabe et al., 2023). Differences between our findings and previous results could be explained by 1) single sample per facility, 2) the different methodology use to sample NH_3 (i.e., airborne observations vs. ground observations), or they may more fully reflect the variability in emissions in space and time. Our estimates are also larger than those reported from other regions. For example, emission rates measured for facilities in Alberta, Canada, report values of 5.83 and 8.5 g $NH_3 \cdot h^{-1} \cdot hd^{-1}$, which are in the lower range of what we observed in northeastern Colorado (Staebler et al., 2009; McGinn et al., 2007). Shonkwiler and Ham (2018) summarize other studies of NH_3 emission rates in other places in the U.S. and around the world during different seasons. NH_3 emissions rates estimates of 2.6 and 5.75 - 8 g $NH_3 \cdot h^{-1} \cdot hd^{-1}$ have been observed downwind of small feedlots (<1200 beef cattle) in China (Yang et al., 2016) and Australia (Denmead et al., 2014), respectively.

3.5 Conclusions

In Chapter 3, I report on summertime airborne observations of NH_3 and CH_4 collected over northeastern Colorado during the first phase of the TRANS^{2}Am field intensive. We intercepted plumes downwind of 29 dairies and cattle feedlots, and we used these observations to infer NH_3 emissions ratios (EmR) with respect to CH_4, and NH_3 horizontal emission rates for a subset of facilities. We show the following:

- NH_3 EmR during August 2021 ranged from 0.1 - 2.6 ppbv ppbv^{-1}, which are larger than those presented in previous literature. The NH_3 EmR associated with beef cattle feedlots are on average four times larger than NH_3 EmR associated with dairies (1.2 vs. 0.3 ppbv ppbv^{-1}, respectively).
- The study region presents a complex combination of emissions sources, especially for CH_4, which has substantial emissions from both oil and gas operations and agriculture intermixed. We present three estimates of NH_3 EmR with and without correction for CH_4 emissions from oil and gas operations. Estimates that account for intermixed oil and gas CH_4 emissions (NH_3 NEMR and OLS regression with agriculturally-specific CH_4) are higher than

NH_3 EmR based on methods that do not account for intermixed oil and gas CH_4 emissions (OLS regression with uncorrected CH_4). Accounting for CH_4 emissions from oil and gas operations is likely more important for aircraft observations than ground-based observations that sample immediately adjacent to facilities. However, prior work that has not accounted for other emissions sources may underestimate NH_3 EmR in the region.

- In the region immediately downwind of the diaries and cattle feedlots we sampled, particle phase NH_4^+ accounted for <15% of the absolute NH_x on average.

- Prior work has reported correlations between NH_3 EmR and temperature. However, data from Phase I of TRANS^{2}Am represents a relatively small temperature range. Even though we document a general trend of increasing NH_3 EmR with temperature, we also observed high NH_3 EmR at lower temperatures with high relative humidities.

- NH_3 NEMRs have a relationship with time of day, with higher NH_3 NEMRs between 12 and 4 PM LT. For 5 of the 6 facilities sampled on different days, NH_3 NEMRs are higher for samples collected under hotter and drier conditions as well as later in the day.

- We document NH_3 decay relative to CH_4 within the plume associated with the largest facility (F04) sampled during Phase I of TRANS^{2}Am. This plume contained the highest NH_3 mixing ratios observed during the campaign. The plume encountered downwind of F04 during RF13 had an e-folding time of 108, 87, and 119.3 minutes for samples collected downwind at 175, 325, and 450 m agl. While the decay was clear on RF13, the plume downwind of F04 did not show similar decay during its sampling on RF03.

- Our inferred horizontal emissions rate estimates for NH_3 for four beef cattle facilities range from 4 - 29 g $NH_3 \cdot h^{-1} \cdot hd^{-1}$ with an average (std) of 14.4 (6.62) g $NH_3 \cdot h^{-1} \cdot hd^{-1}$. We observe larger NH_3 emission rates (g $NH_3 \cdot h^{-1} \cdot hd^{-1}$) compared to other studies, with one exception. We do not find a relationship between maximum reported animal capacity and inferred horizontal NH_3 emissions rates.

Phase I of TRANS^{2}Am substantially increases the number of in situ measurements of NH_3 emissions and their relationship with CH_4 from facilities housing beef cattle and dairy cows in northeastern Colorado. These data represent the warmest part of the seasonal cycle. Future work should focus on colder, more humid conditions characteristic of other times of the year. These data show the variability associated with NH_3 emissions from CAFOs during hot and dry conditions.

Chapter 4

Near-source ammonia evolution observed from in-situ measurements in plumes from large beef cattle facilities.

4.1 Plume characteristics

Figure 4.1 summarizes the spatial and environmental characteristics of the plumes analyzed in this study. F27/28 was sampled in the early morning to early afternoon (10:30 - 15:00). Surface (atmospheric) average temperature for F27/28 during RF11, RF19 and RF22 were 304.2 (299.5), 296.2 (293.7), and 299.4 (296.3) K, respectively (see Figure C.1). The most concentrated portion of the plumes is located within 3 km from the center of the plume. Peak $\mathrm{NH_3}$ ($\mathrm{CH_{4\_ag}}$) is between 250 - 150 ppbv (150 - 100 ppbv) in the first 5 km and rapidly decreases to <50 ppbv by 15 km. The horizontal averaged wind profiles for F27/28 show strong (> $5\mathrm{ms^{-1}}$) and steady winds throughout the plume with a consistent wind direction during all the sampling days (RF11, RF19, and RF22).

In contrast, the winds associated with F04 during RF13 are less consistent. For instance, the first curtain sampled downwind of F04 has wind speeds < $3.5\mathrm{ms^{-1}}$ and the last curtain has wind speeds closer in magnitude to those observed in F27/28 (> $5\mathrm{ms^{-1}}$). There is also a shift in the wind direction, evident by the shift in the center of the plume after 15 km. This plume was only sampled up to 500 m agl due to the presence of a shallow inversion on that day. Measured $\mathrm{NH_3}$ and $\mathrm{CH_{4\_ag}}$ peak mixing ratios for facility F04 are >400 and 300 ppbv, respectively, the largest among all the near-source observations during $\mathrm{TRANS^2Am}$. F04 was sampled between 12:30 and 13:40 with soil and atmospheric temperatures both of $\sim$300.5 K (see Figure C.1).

Finally, F01 was sampled between 11:10 and 12:40 with soil (atmospheric) temperature reaching 302 (297) K (see Figure C.1). F01 horizontal winds are stronger (> $3.5\mathrm{ms^{-1}}$) but have a higher $\mathrm{V_c}$ (larger deviation from the predominant wind direction) than the other plumes. The plume pro-

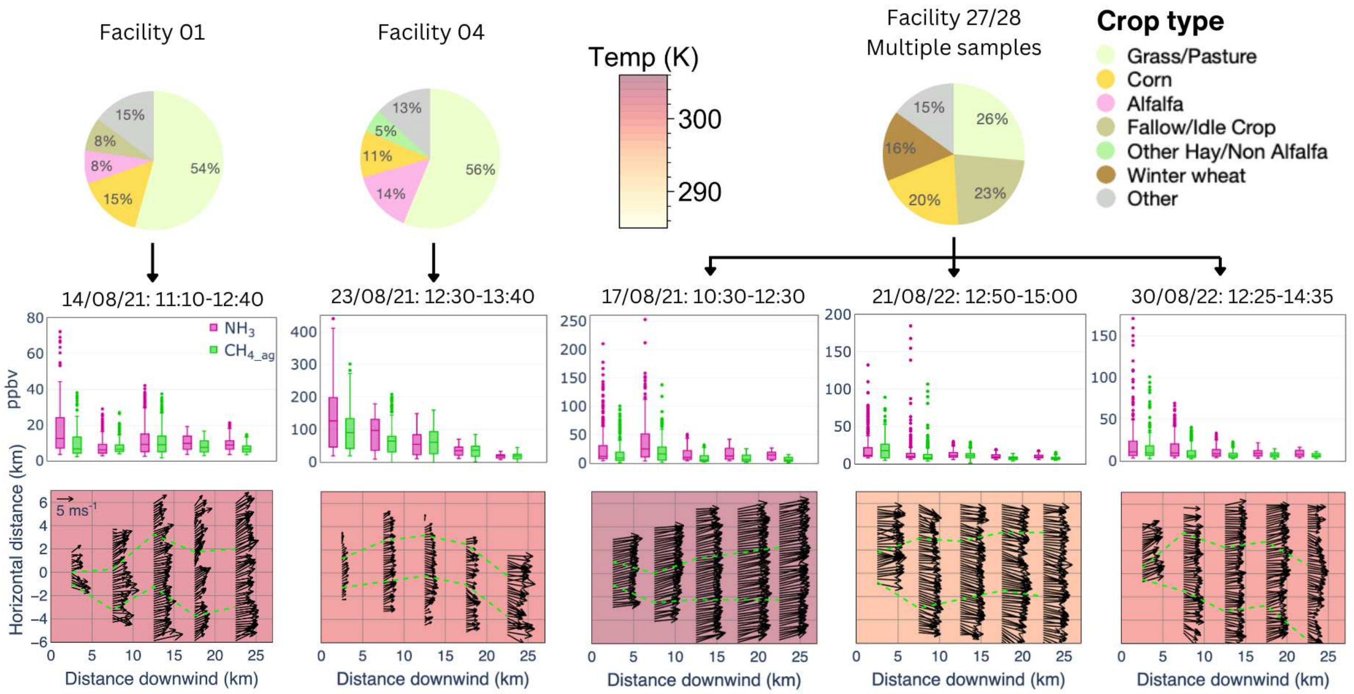

Figure 4.1: Environmental and spatial characteristics of the plumes. The pies in the top row show the predominant crop types downwind of each facility. The middle panels show the distribution of NH_3 (pink) and CH_{4_ag} (green) for each curtain downwind. The bottom panels show the average horizontal wind profile as a function of distance downwind colored by the daily average soil temperature (NARR). The green dashed line represents the horizontal distance at which the NH_3 maximum mixing ratio decreases by 1 standard deviation.

file suggests the plume broadened reaching a maximum width of 3 km at 15 km downwind. Peak NH_3 and CH_{4_ag} mixing ratios are the lowest among the plumes presented in this study (~80 and 40 ppbv, respectively).

4.2 Temporal evolution of NH_3 emissions and mass conductance (J) correction

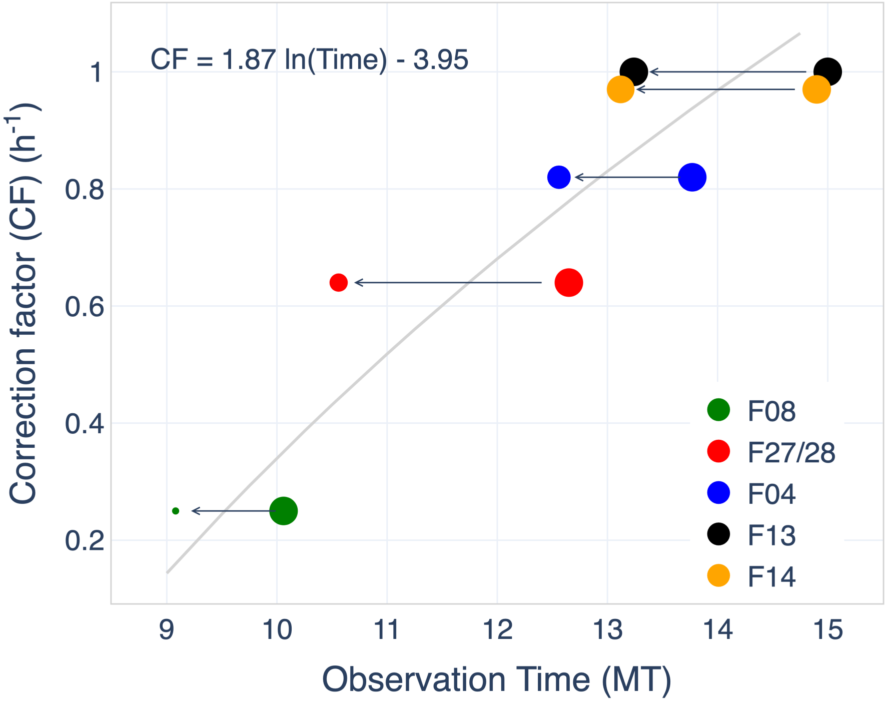

Figure 4.2: Observed hourly change in NH_3 EmR between 9:00 and 15:00 MT. The color of the circles signify different facilities. The right circle sizes are all the same, regardless of the magnitude of NH_3 EmR, which varies by facility. The size of the left circle of the same color represents the relative magnitude of NH_3 EmR one hour earlier for that facility. Grey line is the time-dependent correction factor used to account for differences between NH_3 EmR.

NH_3 emissions ratios with respect to CH_4 (NH_3 EmR) vary strongly with time of day (Juncosa Calahorrano et al., 2023, Eilerman et al., 2016). $\mathrm{TRANS^2Am}$ did not sample plumes in a pseudo-lagrangian fashion. Thus the material in the plume encountered at each transect downwind was not emitted at the same time and $\mathrm{NH_3}$ to $\mathrm{CH_4}$ ratios downwind need to be time-corrected to account for differences between their corresponding $\mathrm{NH_3}$ EmRs. Figure 4.2 shows the relative change in $\mathrm{NH_3}$ EmR observed during repeat sampling of 5 facilities. For instance, $\mathrm{NH_3}$ EmR at 9:00 is 25% of that at 10:00. Later in the day the difference between $\mathrm{NH_3}$ EmR as a function of time decreases, i.e., the $\mathrm{NH_3}$ EmR at 13:00 is similar to that at 14:00 (i.e. a correction factor of 1). The $\mathrm{TRANS^2Am}$ data do not provide information before 9:00 or after 15:00 MT. Thus, the equation presented here can only be used for observations between 09:00 and 15:00 MT. Not accounting for the emission time can lead to an under- (plume emitted later in the day) or overestimation (plume emitted earlier in the day) of $\mathrm{NH_3}$ loss in large plumes from livestock facilities. Therefore, in order to correctly assess the loss of $\mathrm{NH_3}$ in the plumes sampled during $\mathrm{TRANS^2Am}$, we apply the corresponding correction factor from the fit in Figure 4.2 to the mass conductances calculated for each curtain in each facility.

Figure C.2 shows the correction applied to the data presented here. The correction was applied based on the calculated emission time of each curtain (distance traveled × average plume wind speed) relative to the emission time of the first curtain (0 km <= x < 5 km). Some of the facilities sampled earlier in the day (e.g., F27/28 - RF11) need a higher correction than those sampled later in the day (e.g., F27/28 - RF19). Note that all the corrections are relative to the NH_3 EmR on the first curtain.

4.3 $\mathrm{NH_3}$ and $\mathrm{CH_4}$ mass conductances

Figure 4.3 presents the spatial extent and distribution of $\mathrm{NH_3}$ and $\mathrm{CH_{4\_ag}}$ emitted from F27/28 during RF22. We focus the discussion on key features of Figure 4.3; however, this plume is representative of other plumes (see Figures C.3- C.6). The distribution of the $\Delta C \cdot V_p$ for both $\mathrm{NH_3}$ and $\mathrm{CH_{4\_ag}}$ are collocated pointing to a common emission source. Close to the facility (panels a and f) the plume is concentrated immediately downwind of the center of the facility with $\Delta C \cdot V_p$ > 100 $\mu\mathrm{g\ m^{-2}\ s^{-1}}$ spanning 1 or 2 km horizontally from the center of the facility. Note that for

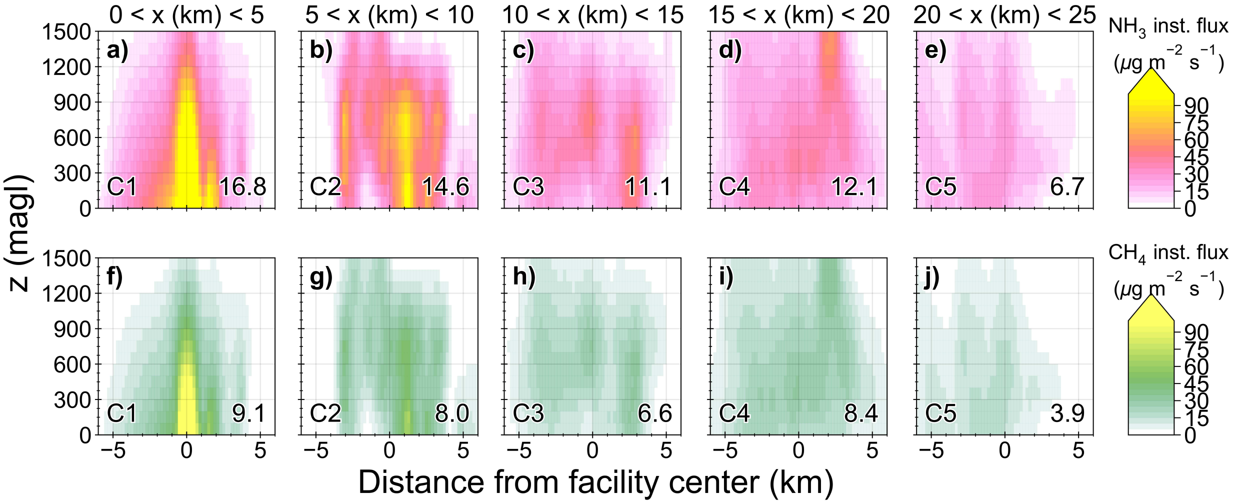

Figure 4.3: Example of NH_3 (top row) and CH_{4_ag} (bottom row) mass conductances (J) for F27/28 sampled during RF22 on August 30, 2022. Panels a - e and f - j present J_{NH3} and J_{CH4_ag} every 5 km downwind of the facility. The colorbar refers to the inferred $\Delta C \cdot V_p$ in each grid cell in $\mu g\ m^{-2}\ s^{-1}$. Grid cells are 200 m wide and 100 m high. The number in the lower right corner is the integrated mass conductance (J) per hour per head of cattle in $g \cdot hr^{-1} \cdot head^{-1}$ for each domain (or ”curtain” C). Panels show simple linear interpolation using the python package scipy.interpolate, with a smooth factor of 1.

curtain 1 (C1), J_{NH3} is higher than J_{CH4_ag} (J_{NH3}/J_{CH4} = 1.85), consistent with previous literature reporting beef cattle NH_3 EmRs > 1 (Eilerman et al., 2016; Golston et al., 2020; Pollack et al., 2022; Juncosa Calahorrano et al., 2023).

Between 5 and 10 km downwind (i.e., C2) , high $\Delta C \cdot V_p$ are still observable, especially for NH_3. Juncosa Calahorrano et al. (2023) reported considerable decay in NH_3 EmR > 10 km downwind. In this case, time corrected J_{NH3}/J_{CH4} = 1.68 signals a 10% loss of NH_3 in the first 10 km of transport. The time correction factor applied for this plume was 0.74 h^{-1}, corresponding to an original emission time of 12:17 PM. This means that the emission at 11:17 AM would be 0.74 that of 12:17 PM (i.e., 1.85 × 0.74 = 1.37). The average emission time for each curtain downwind (C2-C5) was estimated at 12:33, 12:39, 12:36, and 13:04 MT. The difference in emission time between C1 and C2-C5 is between 18 and 46 min, all are below the 1-hour mark (0.272 and 0.781 hours). The difference in the calculated emission time means that the emissions representative of the air masses intercepted between C2 and C5 would be between 0.785 and 0.925 of that intercepted in C1.

Beyond 10 km (C3-C5 or panels c-e and h-j), the $\Delta C \cdot V_p$ for $\mathrm{NH_3}$ and $\mathrm{CH_4\_ag}$ are less concentrated in both the horizontal and vertical directions. Time corrected $J_{\mathrm{NH3}}/J_{\mathrm{CH4}}$ are 1.51, 1.31, and 1.35 for curtains 10-15, 15-20, and 20-25 km downwind, respectively. The decrease in $J_{\mathrm{NH3}}/J_{\mathrm{CH4}}$ with respect to distance downwind is the result of a loss of $\mathrm{NH_3}$, which, during dry and hot summertime conditions, can be mainly attributed to deposition. However, estimated $J_{\mathrm{NH3}}/J_{\mathrm{CH4}}$ in C5 (1.35) is higher than that in C4, suggesting an emission source between these two curtains. To our knowledge, there are no major animal husbandry facilities, urban emissions or landfills in this region, thus we hypothesize that the increase in $J_{\mathrm{NH3}}/J_{\mathrm{CH4}}$ between C4 and C5 is due to crop or soil emissions directly beneath the area between C4 and C5 (see Figure A.13).

There are three small beef cattle facilities in the region that were downwind of the main facility sampled during RF22 (see Figure 2.2e). The first one, has a maximum animal capacity of 4500 and is located 6 km east and 16 km S of the largest beef cattle facility. Due to the wind direction on this day, the emissions from this facility likely mixed with the main plume at C3 and thus C4 and C5 represent a combination of the emissions from both facilities. The second one, has a maximum animal capacity of 3000 and is located 10 km west and 4 km S of the largest beef cattle facility. The third one, has an animal capacity of 6500 and is located 22 km west and 7 km S of the largest beef cattle facility. Due to the wind direction during RF22, we were largely able to remove the emissions from these latter two facilities from our analysis of the evolution of the main plume. We identified potential emission sources downwind of the other facilities and their relative positions downwind are noted later in Figure 4.5 and discussed in Section 4.2.

4.4 $\mathrm{NH_3}$ fraction remaining in the atmosphere

We normalized the corrected $J_{\mathrm{NH3}}/J_{\mathrm{CH4}}$ at different distances downwind with respect to $J_{\mathrm{NH3}}/J_{\mathrm{CH4}}$ from the first curtain (i.e., 0 km <= x < 5 km or C1) to assess the $\mathrm{NH_3}$ remaining in the atmosphere for each facility and this is plotted versus transport time in Figure 4.4. Figure 4.4 shows that the loss of $\mathrm{NH_3}$ in the atmosphere from animal agricultural plumes decays exponentially

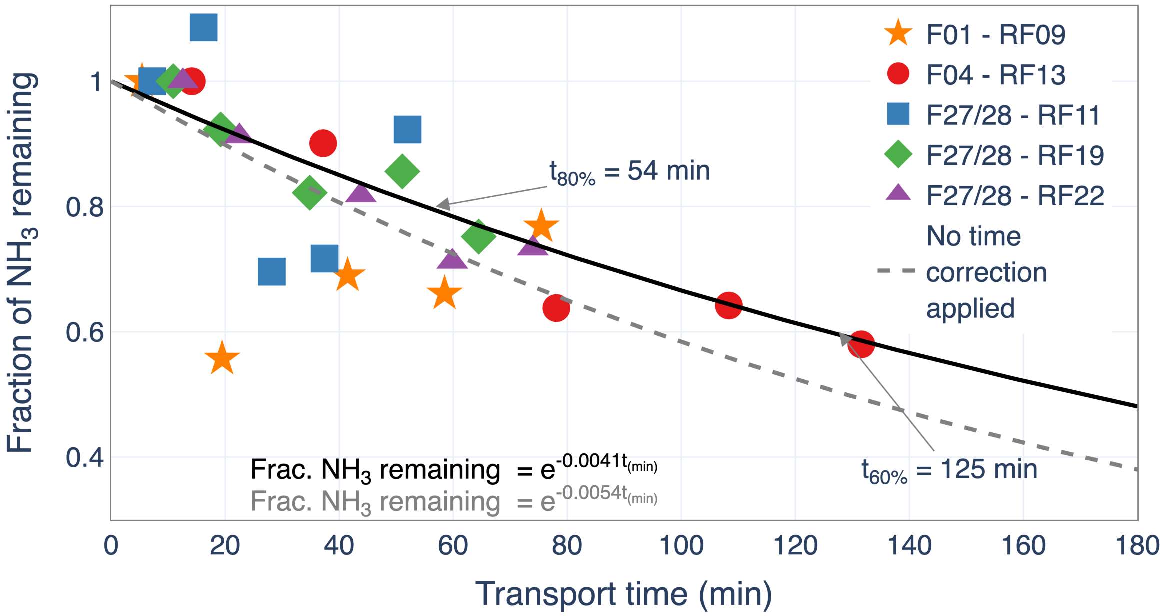

Figure 4.4: Fraction of NH_3 remaining in the atmosphere as a function of transport time from each emission source. Transport time was estimated using the average observed wind speed for each plume. The different symbols and colors correspond to the five research flights (3 facilities). The black solid line is the exponential decay using the correction presented in Section 4.2 Figure 4.2 (symbols shown here). The gray dashed line is the exponential decay without the correction from Figure 4.2 (data points not shown here).

with transport time downwind. Under the conditions sampled during $\mathrm{TRANS^2Am}$, $\mathrm{NH_3}$ decays below 80% and 60% within 40-55 and 100-125 min ($\sim$1 - 2 hours), respectively.

We expect that the loss of $\mathrm{NH_3}$ would depend on initial concentrations, atmospheric conditions, transport time, and underlying surface type. Here we can explore transport time. While all the plumes were observed up to $\sim$25 km downwind of the emission source, the transport time for each plume varies because of differences in the wind speed. Efficient plume transport (i.e., higher wind speeds) results in less potential interaction between the plume and the surface, suggesting that less $\mathrm{NH_3}$ is deposited to the surface. For example, the green diamonds (F27/28 RF11) and red circles (F04 RF13) in Figure 4.4, show two different plumes sampled up to 25 km downwind. The plume represented by the green diamonds was transported by an average wind speed of 8.2 $\pm$ 0.8 $\mathrm{ms^{-1}}$ (consistent throughout the vertical extent) and $\sim$75% of the original $\mathrm{NH_3}$ remains in the atmosphere at 25 km. In contrast, the plume represented by the red circles was transported by average wind speeds 3.3 $\pm$ 1.6 $\mathrm{ms^{-1}}$, resulting in 60% of the original $\mathrm{NH_3}$ remaining in the atmosphere at the same distance. An exception for this would happen when strong winds enhance turbulence .

4.5 $\mathrm{NH_3}$ emission and deposition fluxes

Figure 4.5 shows the net emission and deposition fluxes downwind of each facility. All but one plume which had a significant source at 7 km downwind (F27/28 RF11) during the sampling period, shows net deposition fluxes >0.4 $\mu\mathrm{g\ m^{-2}\ s^{-1}}$ in the first 10 km. $\mathrm{NH_3}$ mixing ratios were the most concentrated in this area (Figure 4.2). Beyond 10 km, there is significant variability in net emission vs. deposition which are discussed below. Emission fluxes (0.5 $\mu\mathrm{g\ m^{-2}\ s^{-1}}$) occurred between 10 - 15 km downwind of F01 when this facility was sampled during RF09. Another small facility (animal maximum capacity = 4500 animals) and the S. Platte River were located between 11 and 12 km downwind of F01. The upward flux provides evidence that this water body may be contributing to fresh emissions. Due to the proximity of other facilities to the S. Platte River upstream of our sampling location (see Figure 2.2), the $\mathrm{NH_3}$ emissions observed near the river

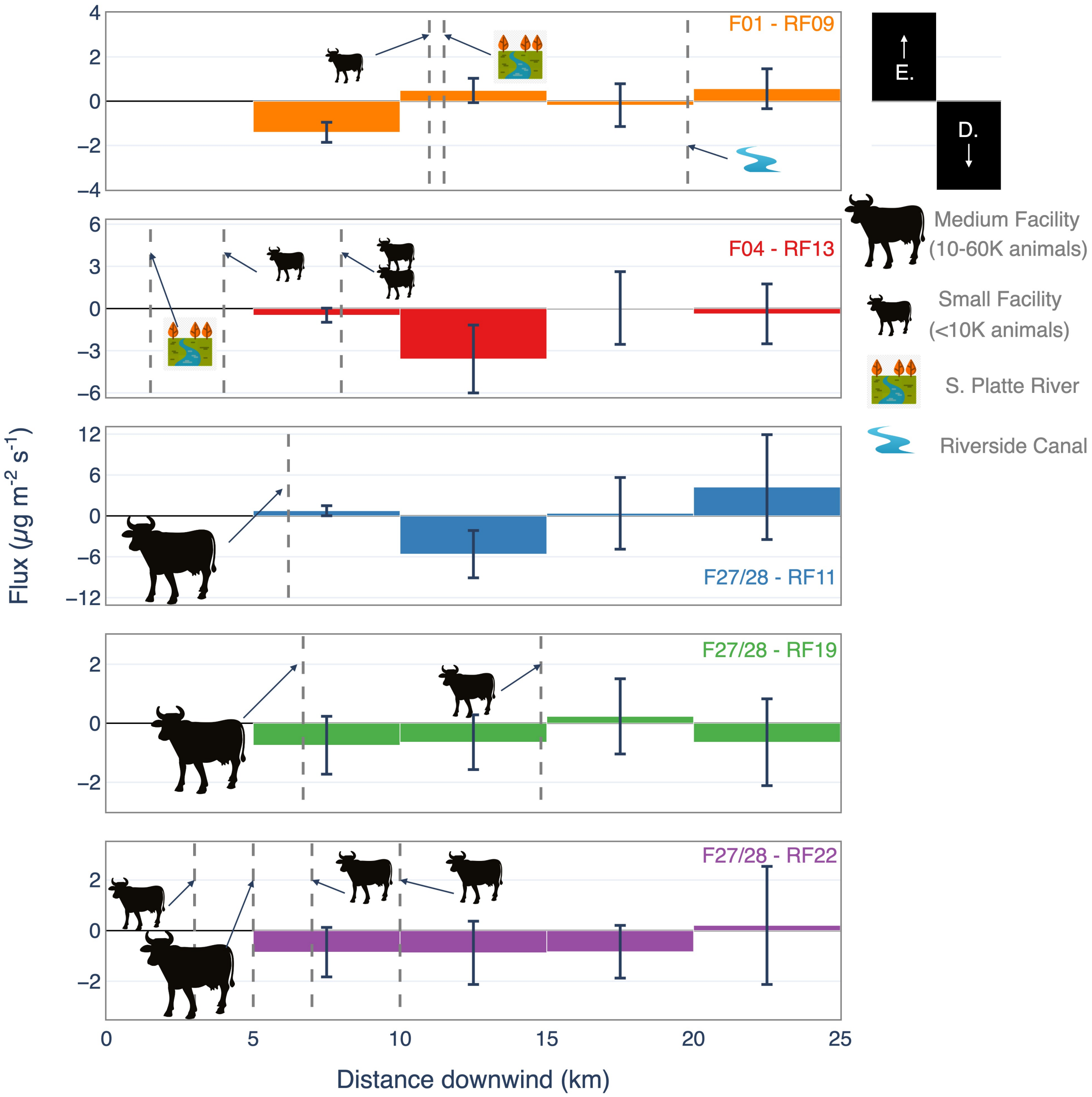

Figure 4.5: Estimated NH_3 fluxes downwind each facility. Each flux was calculated with respect to NH_3 mass conductance from the previous curtain. Positive values indicate net emission fluxes with respect to the previous curtain. Negative values indicate net deposition fluxes with respect to the previous curtain. Grey dashed lines indicate known emission sources located directly beneath a given plume. Bars represent propagated error related to time correction (Figures 4.2 and 4.4), measurement uncertainties (see Section 2.4.1) and a 5% variability in J_{NH3}/J_{CH4} with respect to different boundary conditions (see Section 2.5.2).

might also be influenced by agricultural sources. Between 15 and 20 km the direction of the fluxes is not distinguishable from zero. A water canal located 20 km downwind also likely contributed to the emissions flux observed between 20 and 25 km downwind ($\sim 0.6\ \mu\mathrm{g\ m^{-2}\ s^{-1}}$). F04 - RF13 had the largest $\mathrm{NH_3}$ mixing ratios of the five plumes presented in this study (Figure 4.2). In this case there was net deposition up to 25 km downwind of the facility, except between 15 and 20 km downwind where the direction of the flux is not distinguishable from zero. Other emission sources located within the first 10 km of transport, could contribute to fresh emissions decreasing the calculated magnitude of deposition between 2 and 8 km. The largest estimated deposition flux for this facility occurs between 10 and 15 downwind ($3.6 \pm 0.7\ \mu\mathrm{g\ m^{-2}\ s^{-1}}$).

The plume from F27/28 was sampled several times under different wind conditions (Figure 2.2), which positioned the plume(s) over different sources downwind of the facilities (Figure 4.5). The net flux in between 5 and 10 km downwind during the sampling of plume F27/28 - RF11 is representative of both deposition from F27 and emissions from F28. We are not able to separate these influences because the plumes merged. After the plumes merged (>10 km) a significant deposition flux is calculated between 10 and 15 km downwind ($9.4 \pm 1.5\ \mu\mathrm{g\ m^{-2}\ s^{-1}}$). Similar to F01 and F04, the direction of the fluxes is not distinguishable from zero between 15 and 20 km. Large emissions fluxes ($7 \pm 2.7\ \mu\mathrm{g\ m^{-2}\ s^{-1}}$) are observed between 20 and 25 km downwind. We analyzed satellite imagery as well as crop information and could not identify a single large source (or many small ones) that could explain these emissions. We hypothesize that N-saturated soil or crops (from fertilizer application or previous $\mathrm{NH_3}$ deposition from F27/28) could be responsible for the emissions.

Southwesterly winds during RF19 and RF22 allowed for more favorable sampling of F27/28 with a single plume from both F27 and F28 at approximately the same origin. Under these wind conditions, the plume passed over small facilities located 7 and 15 km downwind that likely contributed to fresh emissions, decreasing the calculated magnitude of deposition between 5 and 15 km. Despite emission from the small facility downwind, there were net deposition fluxes between 5 and 15 km downwind. However, the uncertainty in our estimates shows that the calculated fluxes for both sampling days are not distinguishable from zero. Similar to what was discussed above, satellite images, and the database we use to locate sources (CDPHE, 2014) do not show large emission sources under these plumes, leading us to hypothesize that the N-saturated soil/crops downwind could be the sources in this area.

One of the selection criteria for the plumes selected in this study, was the low number of sources under the plume downwind from the main facility. Even then, the NH_3 fluxes shown in Figure 4.5 illustrate the complexity of NH_3 deposition and emissions in agricultural ecosystems. Studies have suggested that NH_3 fluxes near animal feeding operations might exhibit a net downward (deposition) direction. Here we show that that is mainly true in the first 10 km downwind in the absence of other sources (animal husbandry, water bodies saturates with NH_3). For a given facility, the deposition rate and the direction of the flux is highly dependent on the NH_3 atmospheric concentration and other sources downwind. Our analysis shows that: 1) fresh emissions from relatively smaller facilities can lead to net emission fluxes even in the presence of a large NH_3 plume, 2) the South Platte River and other water bodies can contribute to emissions of NH_3, especially if they are saturated with NH_3 from other agricultural sources (Chen et al., 2021), 3) soil and crops downwind of animal emissions sources can be sources of NH_3.

4.6 Conclusions

Chapter 4 shows analysis of the evolution of five plumes of NH_3 and CH_4 emitted from large cattle feeding operations during summertime over northeastern Colorado. Our observations show the following.

- The transport time of plumes plays an important role in the amount of NH_3 lost to the surface. Faster winds result in more effective transport of plumes and decrease the time for interaction of NH_3 with the surface, decreasing the probability of deposition.
- NH_3 EmR from cattle feeding operations exhibit a strong diurnal dependence. To study the loss of NH_3 in plumes that have not been sampled in a pseudo-lagrangian manner, it is necessary to account for different NH_3 EmRs associated with each plume intercept. Failing

to do so, may lead to an overestimation of $\mathrm{NH_3}$ loss if the plume encountered downwind was actually emitted earlier in the day than the plume intercepted near the facility. Similarly, if the plume intercepted downwind was emitted later in the day, an underestimation of $\mathrm{NH_3}$ loss is likely. This is especially important for plumes sampled in the morning and evening, when $\mathrm{NH_3}$ EmRs change rapidly with time.

- $\mathrm{NH_3}$ loss from large animal agricultural emission sources can be predicted by the plume's transport time. Our observations suggest that 60% of the $\mathrm{NH_3}$ emitted from these large sources is lost within 2 hours of emission. The 80% and 60% time is ~ 1 and 2 hours, respectively. This work has focused on large emission sources with few or significantly smaller sources downwind. However, in many locations, many small animal feeding operations exist close to each other, making it challenging to quantify the fate of a single plume due to the mixing of plumes with different atmospheric ages.

- The bidirectionality of $\mathrm{NH_3}$ fluxes in agricultural ecosystems is evident in the $\mathrm{TRANS^2Am}$ data. The main crops downwind of the plumes studied here are grass/pasture, corn, alfalfa, fallow/idle crop, other hay/non alfalfa, and winter wheat. All have the potential to emit $\mathrm{NH_3}$. Additionally, two of the five plumes presented here were transported towards the S. Platte River which appears to be another source of $\mathrm{NH_3}$ when influence by agricultural sources upstream. Within 10 km of a large animal feeding operation, $\mathrm{NH_3}$ will likely be deposited to the ground. After 10 km, the directionality of the net $\mathrm{NH_3}$ flux varies as a function of the magnitude of the initial deposition and the location of other emissions sources contributing to fresh $\mathrm{NH_3}$.

- Our estimates of $\mathrm{NH_3}$ loss can be utilized in the modeling of single or multiple animal agricultural plumes and their surroundings. The lifetime of $\mathrm{NH_3}$ in the atmosphere should be useful for interpreting satellite observations of $\mathrm{NH_3}$ emissions and transport in the atmosphere.

Chapter 5

Anatomy of a summertime upslope event in northeastern Colorado: Ammonia transport to the Rocky Mountains.

5.1 Partitioning of the gas- and particle-phase NH_x.

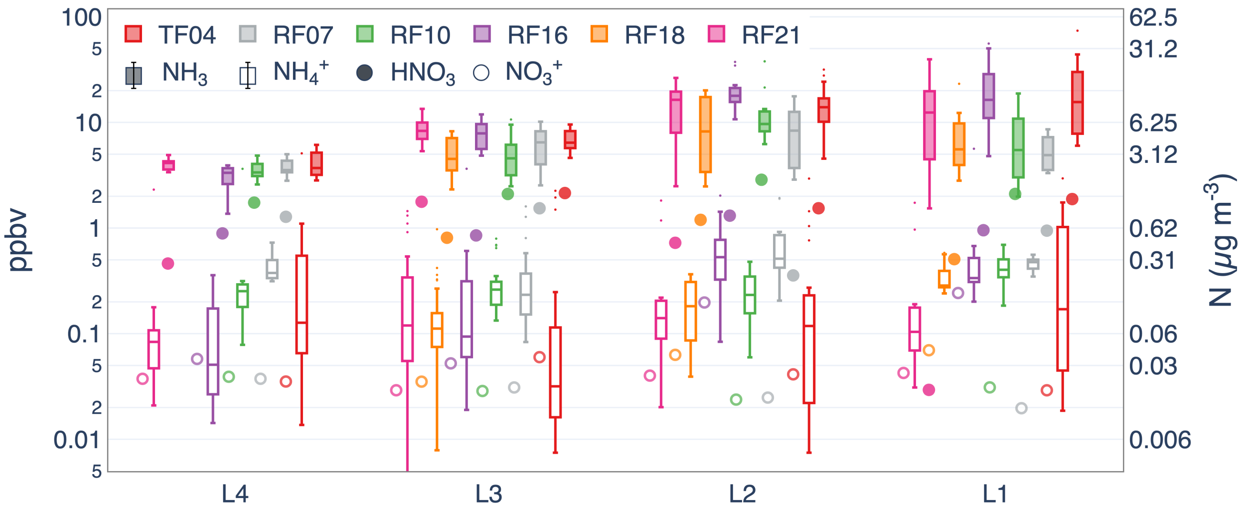

Figure 5.1: Distribution of 2-min averaged NH_3 (closed) and PILS NH_4^+ (open) in ppbv (μg/m^3) for six upslope events sampled over Phase I and Phase II of TRANS^{2}Am. Dots represent average HNO_3 (closed) and PILS NO_3^- values for that leg. L1 to L4 correspond to the transects labeled in Figure 2.3 and are plotted from right to left, showing the partitioning from east to west. Each Lx distribution for the reduced N (NH_3 and NH_4^+) shows the data at all altitudes and uses all data between the longitude ranges described in the methods section. Note both y-axes are on logarithmic scales.

NH_3 mixing ratios decrease from the eastern Colorado source region westward into the mountains, with a ∼10-fold reduction typical between L1 and L4 (Figure 5.1). The largest gradient in

NH_3 occurs between L2 and L3. $NH_4{}^+$ is more equally distributed across all the sampled legs. The difference between $NH_4{}^+$ and NH_3 decreases towards the west and is largely driven by the decrease in NH_3 mixing ratio. The hot and dry conditions encountered during Phase I and II did not favor particle formation during the near-source flights (Li et al., in prep) and likely would be the case for the upslope flights. Phase I was smoke-impacted (see Figures 5.5j - 5.5l), which is most evident in the higher N-aerosol and levoglucosan concentration in L4 for TF04, RF07, and RF10 (see Figure D.1-D.2). There is substantially more $NH_4{}^+$ (NH_3) than $NO_3{}^-$ (HNO_3) in the aerosol (gas-phase). Reduced N dominates in the particle-phase, with one exception we discuss in the SI (i.e., RF18; Figure D.3). Generally, higher percentages of oxidized-N (i.e., HNO_3 and $NO_3{}^-$) are observed in L3 and L4 as the aircraft is situated downwind of the urban corridor.

5.2 Plume tracking

Figure 5.2 shows sharp, distinct co-located plume enhancements in NH_3 and CH_4 during L1 and L2. These large enhancements were observed across all events. These enhancements differ from L3 and L4, where the NH_3 and CH_4 plumes are less concentrated and broader. Both L1 and L2 pass over or directly downwind of some of the largest animal feeding operations. L1 overpassed a large cattle facility with a reported animal maximum capacity of > 100,000 animals (F04 in Juncosa Calahorrano et al., 2023). L2 was located $\sim$10 km downwind of another large cattle facility with a similar animal maximum capacity. As shown in Figure 2.3a, the trajectory analysis in Figure D.4, and the wind roses associated with RF21, the influence of emission sources located along L1 on mixing ratios observed on L2 might be minimal given a) the weak easterly wind component (2 - 4 ms^{-1}) along L1 and b) the distance between L1 and L2 (30 - 32 km).

Summertime upslope events are generally driven by differential topographic heating and are characterized by low wind speeds. The upslope flow starts near the foothills and propagates towards the plains. Since these are thermally driven events, they occur during daylight hours and are usually complemented by nighttime downslope flows (Piña et al., 2019; Baumann et al., 1997). The earlier sampling time (i.e., 12:00 and 13:00 LT) and the nature of summertime upslope flows

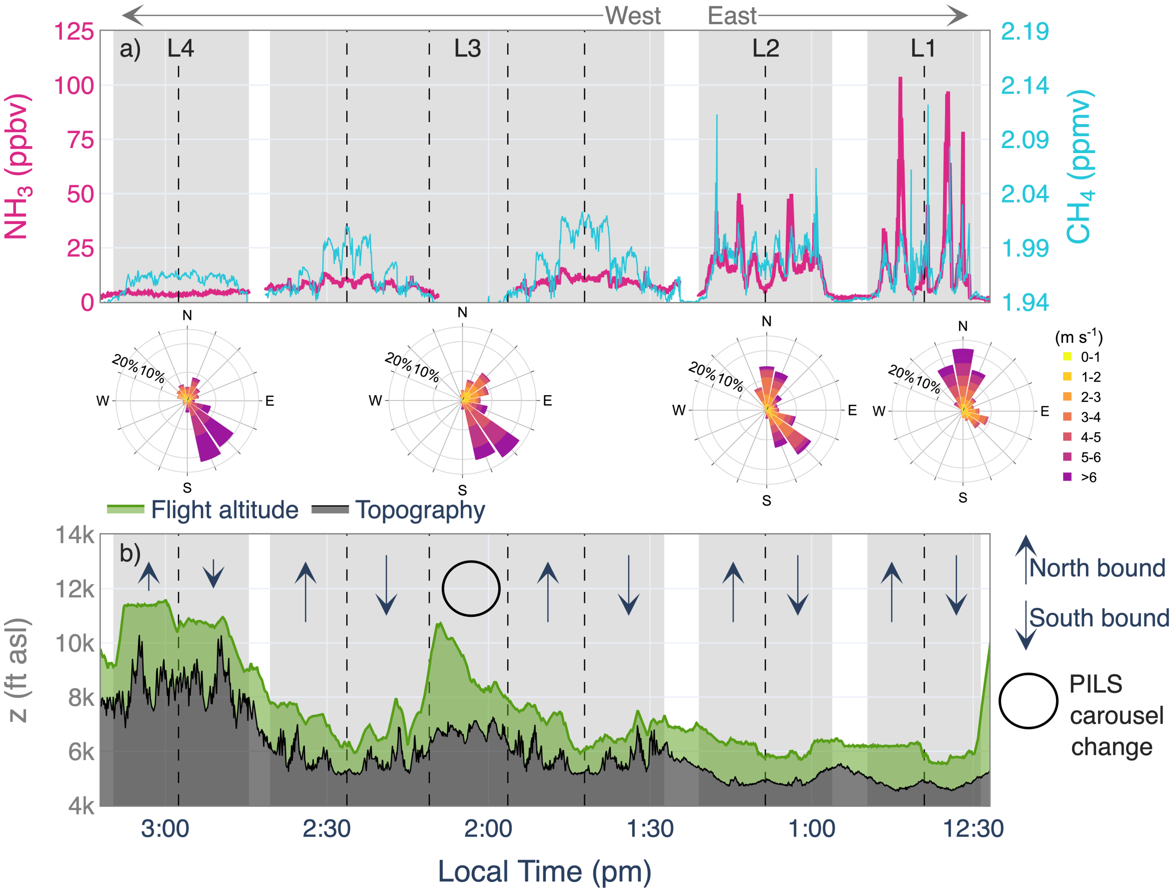

Figure 5.2: a) Time series of NH_3 (pink) and CH_4 (blue) during RF21 (August 29, 2022). The x-axis is flipped to show the eastern legs on the right. b) Corresponding, flying altitude (green) and topography (black). The light gray areas show the limits of each leg, excluding turns. The wind roses represent the wind observed during each sampling period.

are consistent with weaker, less organized winds observed in L1. By the time the aircraft reached L2 (i.e., 13:00 - 14:00 LT), winds with a stronger easterly component (SE, NE, or E) were observed. L2 and L3 are 32 km apart, which includes the narrow 12 km of the Colorado Front Range urban corridor and fewer and smaller animal feeding operations (19, mostly dairies with a maximum animal capacity of <10,000). Between L2 and L3, there is a steep decline in the NH_3 mixing ratios, explained by a combination of fewer and smaller emission sources, dilution, deposition to the ground, and/or partitioning to the particle-phase (minimal, as shown in Figure 5.1).

5.3 Variability between upslope events

Figure 5.3 shows the NH_3 plume sampled by the UWKA during the upslope event on July 27, 2021 (TF04). The NH_3 plume is observed in all four flight legs. The winds during TF04 were strong (max = 9.2 ms^{-1} with gusts up to 40 ms^{-1} in L4) and sustained, especially later in the day, resulting in effective transport of NH_3 emissions westward. As in the example shown in Figure **??**a, the NH_3 enhancements along L1 and L2 are large, sharp, and usually co-located near animal husbandry facilities. ΔNH_3 along L1 and L2 range between 20 - 550 ppbv and are co-located with ΔCH_4 (up to 600 ppbv). NH_3 along L3 reaches $\sim$10 ppbv above background (5 ppbv). NH_3 intercepted along L4 is $\sim$7 ppbv above background ($\sim$4 ppbv), and the plume is identifiable towards the northern edge of L4, consistent with the southeasterly winds along L3.

To estimate transport times for plumes intercepted in L3 and L4 from specific upwind areas, we initialized forward trajectories coincident with large ΔNH_3 observed along the UWKA flight track (see Section 2.5.3). The trajectories and wind roses confirm weak southerly winds that transport emissions along L1 to the north. Consistent with this picture, high NH_3 concentrations (up to 560 ppbv) were encountered along L1 and towards the northern portion of the UWKA flight track between L1 and L2, where no major emission sources are located. The trajectories on L1 were initialized at 11 am LT. To investigate whether easterly flow would organize in time to transport emissions from L1 towards L2, L3, and L4, we initialized another set of forward trajectories along L1 each hour between 10 am and 3 pm LT (not shown). The trajectories initialized after 1 pm

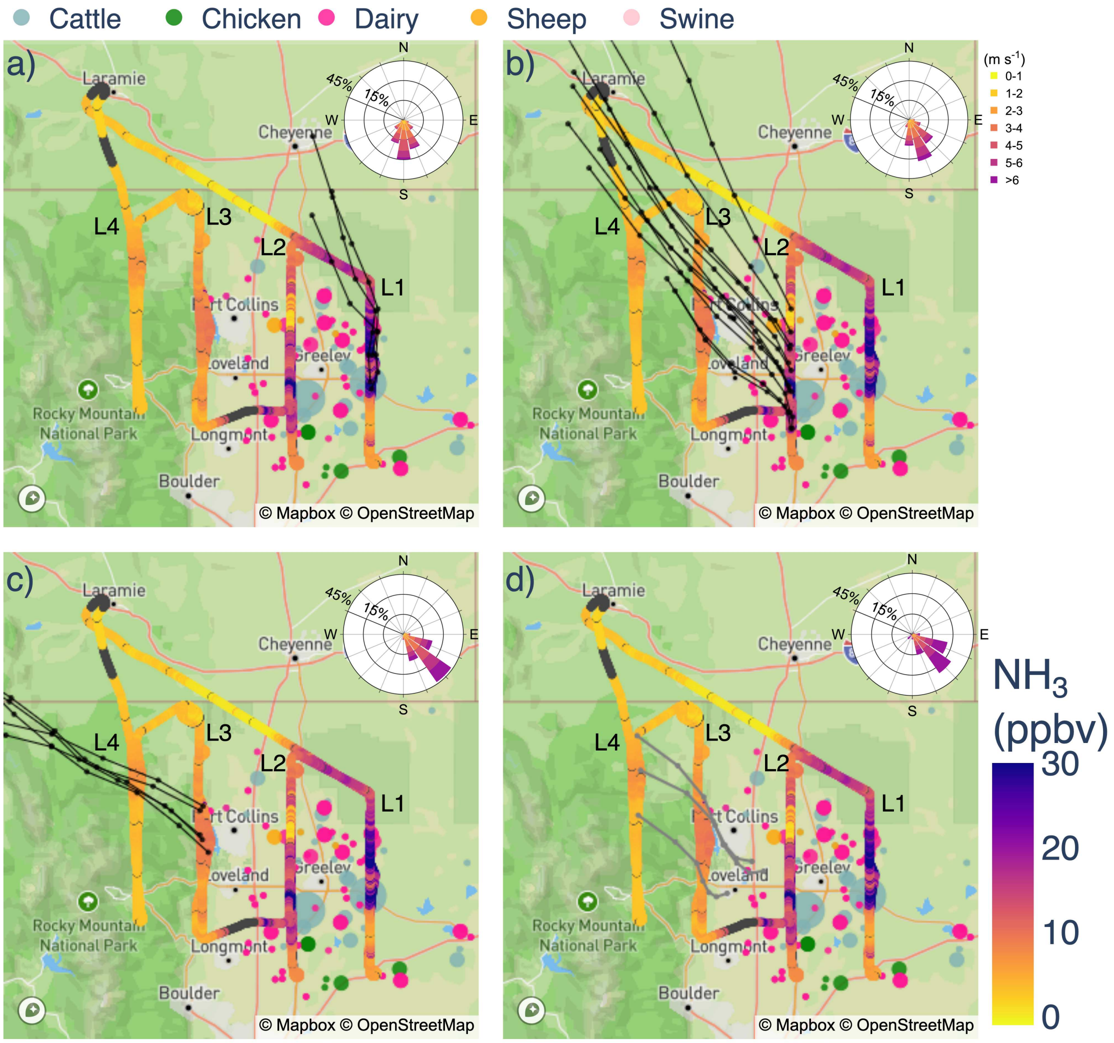

Figure 5.3: UWKA flight track colored by NH_3 mixing rations during TF04 (July 27, 2021). The black sections along the flight path indicate instrument zeros. The wind roses correspond to the wind observed in each leg (a) - (d) corresponding to L1 - L4. Circles signify livestock housing facilities colored by type of animal and sized by the reported maximum animal capacity. The black and gray lines show HYSPLIT forward and backward trajectories, respectively. Each dot within the lines represents one hour of transport.

LT suggest that plumes from emission sources located along the southernmost portion of L1 could reach L2 and contribute to $\Delta\mathrm{NH}_3$ over the northern portion of L3 between 2 and 3 pm LT, 2-3 hours after L3 was completed.

South-southeast (SSE) winds with an average speed of 4.4 ms^{-1} were encountered along L2. The trajectories suggest that the transport of emissions from L2 would take $\sim$3-4 hours to reach L3 (i.e., $\sim$30 - 32 km downwind). The trajectories initialized along L2 suggest that the plume observed on L3 originates from emission sources located on the southern end of L2. Note the large NH_3 enhancements (up to 65 ppbv) near the large beef cattle facility toward the south of L2.

Given that the uncertainty of trajectories increases with time, we re-initialized another set of trajectories along L3, coincident with the observed plume. The broad nature of the plume suggests contributions from transport rather than emissions at this location. Along L3, predominantly southeasterly (SE) winds enable more efficient transport into the mountains. The transport time for the plume observed in L3 to L4 is only 2 hours. The trajectories suggest that the two enhancements encountered in L3 and L4 are from the same transported plume originating from the same facility. We expect considerable NH_3 deposition in the $\sim$30 km between L2 and L3 with an average transport time between 3-5 hours (Juncosa Calahorrano et al., 2023). Between L2 and L3, the plume passed over several small dairies with maximum animal capacities < 8000. Dairies typically have lower $\Delta\mathrm{NH}_3$:$\Delta\mathrm{CH}_4$ ratios than cattle feeding operations (Juncosa Calahorrano et al., 2023). The $\Delta\mathrm{NH}_3$:$\Delta\mathrm{CH}_4$ in L3 was between 0.12 - 0.28 ppbv ppbv^{-1}, consistent with a combination of fresh dairy emissions and beef cattle emissions transported over several hours.

Other events observed during $\mathrm{TRANS}^2\mathrm{Am}$ show less efficient transport of plumes from major agricultural sources and the potential for recirculation of plumes to the east. Figure 5.4 shows data collected during RF10 (August 16, 2021). Note that L1 during RF10 was positioned further east (upwind of most animal husbandry facilities) than on other sampling days; thus, lower NH_3 enhancements were observed over this leg (< 40 ppbv). Consistent with what was observed during most of the other sampling days, the winds on L1 are less organized and weaker compared to L2 - L4. During RF10, winds along L2 show a partial easterly component. However, they are

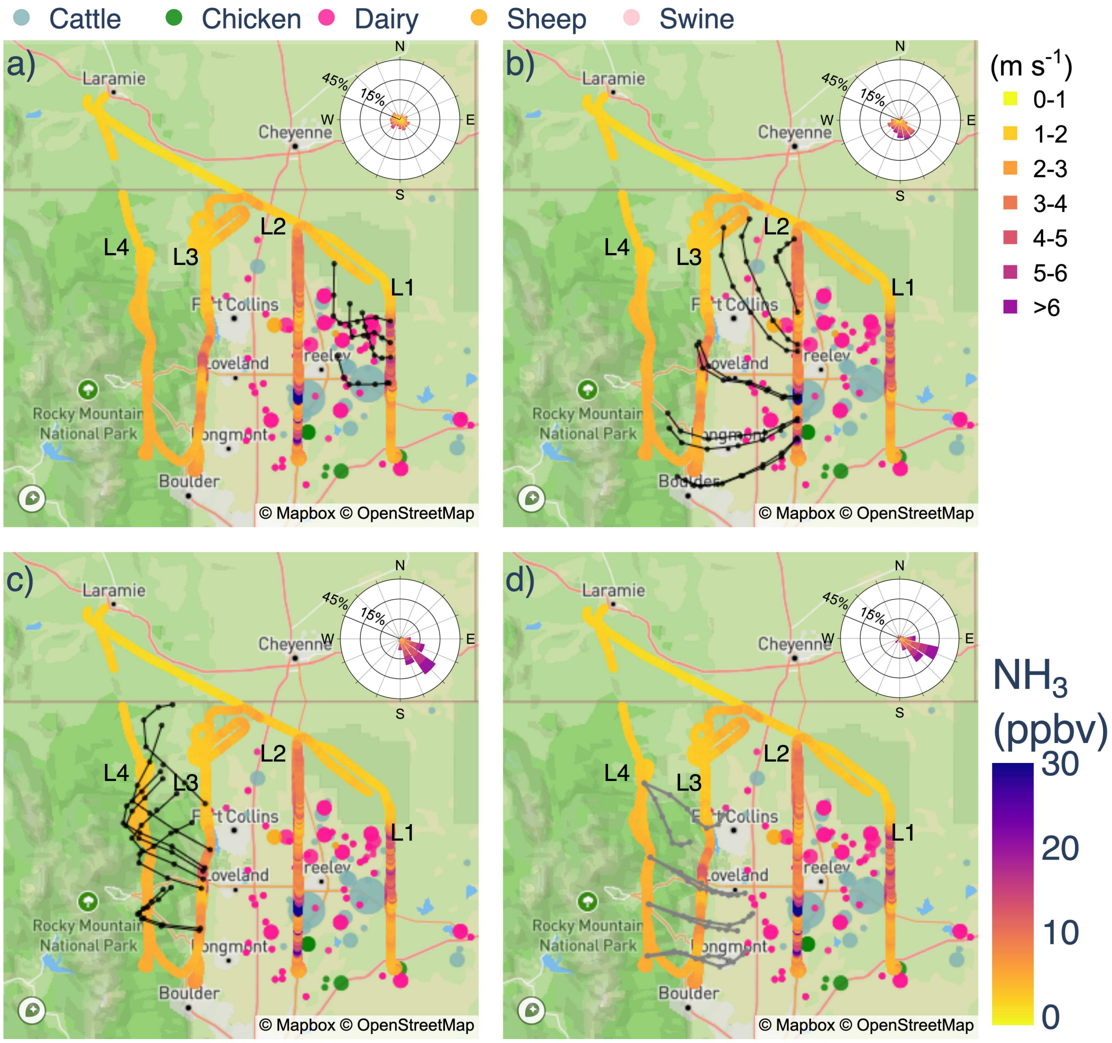

Figure 5.4: As described in Figure 5.3, except for RF10 (August 16, 2021).

less organized than those observed during TF04 (Figure 5.3b). This wind variability suggests that emissions to the south of L2 are transported to the SW, emissions along the middle of L2 are transported towards the west (stronger easterly component), and emissions along the northern end of L2 are transported to the north (southerly winds). This results in at least two distinct plumes observed along L3. These plumes can be attributed to emission sources located along the southern (NH_3 enhancement in L3 $\sim$10 ppbv) and middle portion of L2 (NH_3 enhancement in L3 $\sim$20 ppbv). As these plumes are transported into the mountains, they are recirculated back to the east. A distinct sharp plume is not observed along L4; instead, a small enhancement is observed along the leg with a maximum NH_3 of 5 ppbv ($\sim$3 ppbv above the background).

These examples show that summertime upslope events in the Colorado Front Range have diverse flow patterns. Figures D.3, D.4, and D.5 show similar analysis for RF18, RF21, and RF16. A few commonalities of all the events include the following. 1) The largest enhancements of NH_3 and CH_4 are observed near large livestock facilities. While water treatment facilities and golf courses were not the focus of the study, L3 of our flight pattern did pass downwind of a water treatment facility and several golf courses, and we were not able to distinguish any additional NH_3 plumes. Distinguishing the contribution of vehicles is not possible with data from Phase I of $\mathrm{TRANS^2Am}$ due to the high CO associated with the wildfire smoke. However, L3 in RF16, RF18, and RF21 have average NH_3:CO of 0.26 - 0.55, which are substantially higher than NH_3:CO from vehicle emissions (0.029 ± 0.005; Sun et al., 2014). 2) During the morning, L1 shows weaker and less organized winds that suggest less efficient transport to the foothills (L3) and mountain (L4) legs, especially before 3 pm. 3) At least one distinct broad plume is observable along L3 for all flights. Using wind information and trajectories, we can link these plumes to large emission sources along L2. 4) Three of the five upslope events show recirculation of polluted air to the east, whereas two suggest effective transport further west. This last point has important implications for studies investigating N-deposition in RMNP because the N deposited during summer could be from a recirculated and diluted plume rather than a fresh one, depending on where the measurements are taken.

5.4 NH_3 spatial gradient and loss during upslope events.

The top panels in Figure 5.5 (a, b, and c) show a clear regional, east-to-west gradient in NH_3 across NE CO. The largest NH_3 mixing ratios are observed along L2, corresponding with the location of livestock facilities (e.g., 40.32° N, immediately downwind of a large cattle facility). The average NH_3 on L2 across all sampling days ranges from 8 - 33 ppbv. Note the large range of NH_3 mixing ratios observed along this leg, which suggests that background and plume conditions were sampled during all RF flights (see Figure **??**). Average NH_3 mixing ratios over L3 show less variability than in L2, ranging from $\sim$3 - 8 ppbv, with the lowest values towards the north of L3. Unlike L2, there is no distinct peak at one location along L3; rather, there are two broader plumes to the north and south of the peak at L2, and the cluster of facilities located to the north of L2, consistent with SE or NE winds observed during $\mathrm{TRANS^2Am}$. L4 shows the lowest concentration and variability of NH_3 with a small, broad plume towards the north of the leg. The differences in average NH_3 between L4 and the other eastern legs range from 0.3 - 4.3 ppbv (L3) and 4 - 30 ppb (L2).

There is also a regional east-to-west gradient in CH_4 (Figure 5.5d - 5.5f). A few CH_4 peaks near agricultural facilities stand out (e.g., L2: 40.32° N and L3: 40.52° N). In addition to agricultural activities, there is also dense oil and gas extraction in the eastern portion of our study area, providing another source of CH_4 (see Figure D.7). To interpret the latitudinal profiles in CH_4, we also provide latitudinal profiles of C_2H_6 (Figure 5.5g - 5.5i), a tracer for oil and gas activities. Both CH_4 and C_2H_6 are elevated in L2, corresponding with the location of the oil and gas well-dense Denver-Julesburg basin. Opposite to the CH_4 profiles, there is little difference between the C_2H_6 profiles in both western legs (L3 and L4). Therefore, differences in CH_4 observed between L3 and L4 are likely attributable to the transport of agricultural emissions of CH_4 between L2 and L3 and a decreased influence from oil and gas sources between these two legs.

We use the longitudinal (east-west) gradients in NH_3 and CH_4 to estimate the percentage of NH_3 loss in transport from L3 and L4. Since no agricultural (or oil and gas; see Figure D.7) sources exist in this area, the difference in NH_3 normalized by CH_4 (a conservative tracer on

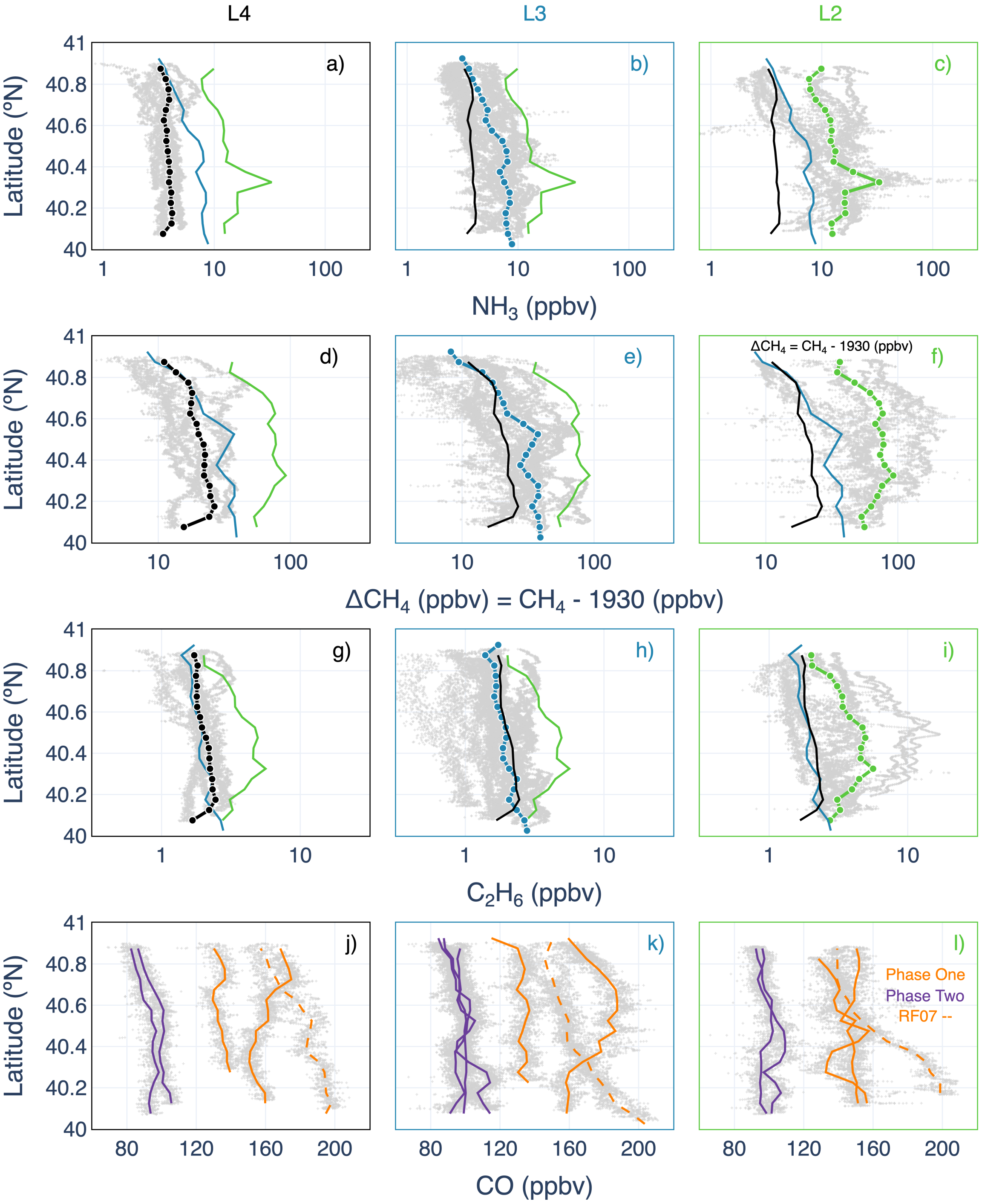

Figure 5.5: (a-i) 1-Hz NH_3 (top panels), ΔCH_4 (second row), C_2H_6 (third row) vs. latitude binned by L4 (first column), L3 (middle column), and L2 (third column). Lines with circles in each panel show latitudinal averages across that leg for all the flights. Lines with no circles show latitudinal averages for the other two legs. Colors remain the same across all the data (L4: black; L3: blue; and L2: green). (j - l) 1-Hz CO vs. latitude binned by legs. Each line represents the latitudinal averages for CO for each flight in that leg (flights in Phase One: orange; Phase Two: purple). Altitudinal average profiles are shown in Figure$_S$7.

relevant transport timescales) between legs is a function of the loss of $\mathrm{NH_3}$ to deposition and aerosol partitioning. Because upslope sampling during $\mathrm{TRANS^2Am}$ was not pseudo-lagrangian, we account for the diurnal cycle in emission from livestock facilities, shown to vary significantly throughout the day (Juncosa Calahorrano et al., 2023). The plume intercepted along L4 was emitted an hour earlier than the plume intercepted along L3. On average, the plumes intercepted along L3 and L4 were emitted at 10 and 9 am, respectively. The $\mathrm{NH_3}$:$\mathrm{CH_4}$ is 10-30$\%$ larger at 10:00 than at 9:00 am. We estimate that $\sim$70$\%$ of the $\mathrm{NH_3}$ in L3 is lost during transport to L4. During $\mathrm{TRANS^2Am}$, this loss is mostly in the form of dry deposition, given the absence of precipitation and low prevalence of $\mathrm{NH_4NO_3}$ formation during the summertime months.

5.5 Comparison to Prior Studies in Northeastern Colorado

Several other studies in Colorado have helped to shape our understanding of nitrogen transport from the Front Range into RMNP. The aircraft observations presented here both reinforce and challenge past findings.

During the summer, easterly winds establish close to the foothills, and their eastward extent is limited. This was reported by Baumann et al. (1997), and easterly flow was not present in our easternmost flight leg. We also observed the recirculation of plumes near the mountains, which has also been observed by Sullivan et al. (2015). During $\mathrm{TRANS^2Am}$, we sampled plumes over the mountains that were likely emitted from sources in the morning. However, an analysis of wind in Fort Collins and Greeley coupled with measurements of $\mathrm{NH_3}$ in RMNP shows that the stronger afternoon winds over the northern Front Range are correlated with higher $\mathrm{NH_3}$ in RMNP later in the afternoon (Figure D.8 - D.9). This pattern, also observed by Baumann et al. (1997), is partially explained by higher afternoon emissions of $\mathrm{NH_3}$ (Eilerman et al.,2016; Juncosa Calahorrano et al., 2023).

Most of the $\mathrm{NH_x}$ observed during $\mathrm{TRANS^2Am}$ is in the gas-phase in agricultural plumes; $\mathrm{NH_3}$ was 1-2 orders larger than $\mathrm{NH_4}^+$. Hot and dry conditions during $\mathrm{TRANS^2Am}$ inhibited the formation of $\mathrm{NH_4NO_3}$ (Juncosa Calahorrano et al., 2023; Li et al., in prep), and $\mathrm{TRANS^2Am}$

observations represent $\mathrm{NH_3}$ plumes with excess $\mathrm{NH_3}$ vs. the broader range of conditions captured by the site in RMNP reported by Benedict et al. (2013a). Over sites closer to the agricultural region, $\sim$90$\%$ of the reduced nitrogen in the atmosphere has been observed in the gas-phase (Benedict et al., 2013a), which is closer to the observed partitioning of reduced N during $\mathrm{TRANS^2Am}$. We observe that over 50$\%$ of the N measured during $\mathrm{TRANS^2Am}$ (total $\mathrm{NO_3}$ and $\mathrm{NH_4}$) was reduced (i.e., $\mathrm{NH_3}$ and $\mathrm{NH_4}^+$). $\mathrm{NO_2}$ was not sampled during $\mathrm{TRANS^2Am}$, but it is likely a large portion of the N transported to RMNP (Benedict et al., 2013a).

We observe major regional gradients in $\mathrm{NH_3}$ across northeastern Colorado; longitudinal averages range from 3 to 26 ppbv. Passive samples collected across NE Colorado provide a consistent picture. Summertime maximum regional gradients observed from 2012 to 2015 were $\sim$53 ppbv between Greeley and RMNP (Li et al., 2017). This gradient decreased between the foothills and source region areas to $\sim$12 ppbv (Benedict et al., 2013b). The regional gradients presented here (0.3 - 30 ppbv) represent upslope events. Under other wind patterns, we expect a larger difference between the westernmost legs and the source regions.

Finally, we calculate the percentage of $\mathrm{NH_3}$ loss ($\sim$70$\%$) between L3 and L4, which, under ideal wind conditions (sustained easterly winds), could be translated to an $\mathrm{NH_3}$ deposition rate. Several studies have reported $\mathrm{NH_3}$ dry deposition rates in the region between 1.8 and 27 ng $\mathrm{NH_3}$ $\mathrm{m^{-2}}$ $\mathrm{s^{-1}}$ (Benedict et al., 2013a; Benedict et al., 2018; Burns, 2003; Campbell et al., 2000; Pan et al. 2021), with the higher values corresponding to air masses that can be traced back to the northeastern agricultural region. Our data provide useful information for future modeling efforts to quantify further the rate of $\mathrm{NH_3}$ deposition and its latitudinal gradient in the region.

5.6 Implications and future directions

The observations presented here show effective westward transport of agricultural $\mathrm{NH_3}$-rich plumes from northeastern Colorado to the Rocky Mountains. Emissions from facilities near the foothills have the highest potential for efficient transport to the mountains during summer afternoons under thermally driven wind systems. We have sampled $\mathrm{NH_3}$ plumes that can be largely attributed to individual livestock facilities. Future modeling efforts should benefit from considering large livestock facilities as point sources rather than area sources. Targeted reductions in emissions of $\mathrm{NH_3}$ close to the foothills during summer may also be more effective in reducing summertime N deposition under these conditions. In the summers of 2021 and 2022, upslope events were dominated by SE winds, transporting nitrogen-rich plumes north of Denver further north and westward. This pattern likely enhanced $\mathrm{NH_3}$ deposition in the Colorado Rocky Mountains unequally, with the strongest enhancements in the north decreasing in the south direction. Latitudinally spaced surface monitors would provide a more comprehensive constraint on N deposition in RMNP and mountain regions to the south and north of the park.

Partitioning of $\mathrm{NH_3}$ to the particle-phase was relatively minor during the warm, dry conditions characteristic of $\mathrm{TRANS^2Am}$. However, colder and more humid conditions that occur more frequently in other seasons will promote $\mathrm{NH_4NO_3}$ aerosol formation. Further, larger scale synoptically driven upslope flow, more common in spring and autumn, can push air from regions further east back up against the Rocky Mountains. Therefore, a similar airborne campaign in other seasons would likely unveil important differences in a) the partitioning of $\mathrm{NH_3}$ to the particle-phase, b) the influence of $\mathrm{NH_3}$ transport from facilities located further east in the study region, and c) additional major facilities that disproportionately contribute to $\mathrm{NH_3}$ deposition in RMNP.

Chapter 6

Summary, conclusions, and recommendations for future research.

6.1 Summary

This dissertation better quantifies the summertime emissions, evolution, and transportation of $\mathrm{NH_3}$ from large animal feeding operations in northeastern Colorado. I present an analysis of observations from the Transport and Transformation of Ammonia ($\mathrm{TRANS^2Am}$) airborne field campaign, which was conducted during the summers of 2021 and 2022. The $\mathrm{TRANS^2Am}$ data collection was designed to 1) improve quantification of the $\mathrm{NH_3}$ emissions from cattle feedlots and dairies, 2) increase understanding of the near-field evolution of the emitted $\mathrm{NH_3}$, and 3) investigate easterly wind conditions (i.e., upslope events) capable of moving agricultural emissions of $\mathrm{NH_3}$ through urban areas and into the Rocky Mountains. This work is separated into three papers. In the first paper (Chapter 3, published in the *Journal of Geophysical Research (JGR)* in 2023, Juncosa Calahorrano et al. 2023), I use near-source measurements of $\mathrm{NH_3}$ and $\mathrm{CH_4}$ to quantify $\mathrm{NH_3}$ EmRs. In the second paper (Chapter 4, to be submitted to *Environmental Science and Technology (ES&T)*, Juncosa Calahorrano et al., in prep), I present the timescales of the loss of $\mathrm{NH_3}$ to deposition in the near-field from five large animal feeding operations. In the third paper (Chapter 5, submitted to *ES&T*, Juncosa Calahorrano et al. (submitted)), I study the time and spatial scales of the transport of $\mathrm{NH_3}$ from large animal feeding operations towards the RMNP under upslope conditions (i.e., easterly winds).

6.2 Chapter 3 overview

Using $\mathrm{NH_3}$ and $\mathrm{CH_4}$ observations from Phase I of $\mathrm{TRANS^2Am}$, I found that $\mathrm{NH_3}$ EmRs have a strong dependence with time of day, and my estimates of $\mathrm{NH_3}$ EmRs for 29 feedlots and dairies in the region are larger than previously reported in the literature with a large range of values (i.e., 0.1 - 2.6 ppbv ppbv^{-1}). Facilities housing cattle and dairy had a mean (std) of 1.20 (0.63) and 0.29 (0.08) ppbv ppbv^{-1}, respectively. Since most of these animal husbandry facilities are co-located within oil and gas development, an important source of $\mathrm{CH_4}$ and $\mathrm{C_2H_6}$ in the region, these estimates include correction of $\mathrm{CH_4}$ from oil and gas. I also found that only 15% of the $\mathrm{NH_x}$ is in the particle phase (i.e., $\mathrm{NH_4{}^+}$) near major sources during the warm summertime months when $\mathrm{TRANS^2Am}$ took place. I studied the evolution of $\mathrm{NH_3}$ in one plume that was sampled at different distances and altitudes up to 25 km downwind and estimated that the $\mathrm{NH_3}$ lifetime against deposition and partitioning to the particle phase is between 87 and 120 minutes. Finally, I present estimates of $\mathrm{NH_3}$ emission rates from 4 optimally sampled facilities. These ranged from 4 - 29 g $\mathrm{NH_3} \cdot \mathrm{h}^{-1} \cdot \mathrm{hd}^{-1}$, which are within previously reported values.

6.3 Chapter 4 overview

I use $\mathrm{NH_3}$ and $\mathrm{CH_4}$ observations from 5 agricultural plumes from large emissions sources sampled 25 km downwind during Phase I and Phase II of $\mathrm{TRANS^2Am}$. $\mathrm{TRANS^2Am}$ did not sample the plume in a lagrangian manner, which can lead to over or underestimation of $\mathrm{NH_3}$ loss in the nearfield due to the strong dependence of $\mathrm{NH_3}$ EmR and time of day. Using data from five other facilities that resampled emissions on the same RF at different times, I propose a simple correction factor to account for differences in $\mathrm{NH_3}$ EmR per hour between 09:00 and 15:00 LT. Using $\mathrm{CH_4}$ as a conservative tracer in the timescales of plume transport, I calculated the decay time of $\mathrm{NH_3}$ below 80 and 60% in plumes from large animal feeding operations, which is $\sim$1 and 2 hours, respectively. Additionally, I calculated emission fluxes every 5 km downwind of the plume. I found that deposition almost always happens in the first 10 km from the emission source. Beyond that, the complex environmental exchange of $\mathrm{NH_3}$ between the atmosphere and the surface suggests that fresh $\mathrm{NH_3}$ emissions from small nearby sources, water bodies, and crops/soil could contribute to sufficient $\mathrm{NH_3}$ to switch the direction of the flux (to emission).

6.4 Chapter 5 overview

I studied the transport of $\mathrm{NH_3}$ during the six upslope events sampled during Phase I and Phase II of $\mathrm{TRANS^2Am}$. I found that $\mathrm{NH_3}$ enhancements are present over the mountains on summer afternoons with easterly winds in the foothills region. Gas-phase $\mathrm{NH_3}$ is 1 and 2 orders of magnitude higher than particle-phase $\mathrm{NH_4}^+$ in the mountains and near the source region, respectively. Summertime upslope events exhibit thermally driven circulation periods in which the easterly flow first establishes near the foothills and then spreads towards the eastern plains. I found that emission sources closer to the mountains likely contribute more to the $\mathrm{NH_3}$ observed over the mountains than sources located further east. For the six upslope events sampled during $\mathrm{TRANS^2Am}$, I estimate that the transport of plumes from major emission sources in NE Colorado westward across the foothills requires $\sim$5 hours. Finally, I observed that winds drive variability in the transport of $\mathrm{NH_3}$ into nearby mountain ecosystems, producing both direct plume transport and recirculation towards the east.

6.5 Recommendations for future research

6.5.1 Campaigns in other seasons

$\mathrm{TRANS^2Am}$ was carried out during August 2021 and 2022. This timing resulted in little partitioning of $\mathrm{NH_3}$ to the particle phase due to the warm and hot conditions. Therefore, questions still remain about the timescale and magnitude of $\mathrm{NH_3}$ that partitions to the particle phase in conditions where $\mathrm{NH_4}^+$ formation is more favorable (i.e., winter, autumn, and spring). Moreover, there are important differences between spring and autumn versus summertime upslope events. The former are often driven by synoptic-scale winds that can produce sustained upslope transport of $\mathrm{NH_3}$ emissions to the mountains. Spring and autumn upslope events often generate clouds and precipitation which would result in scavenging of NH_3 by cloud droplets. Therefore, I recommend organizing a similar campaign in other seasons to answer the following questions. 1) What is the magnitude and timescale of the partitioning of gas-phase $\mathrm{NH_3}$ to the particle-phase in the near field? 2) What are the timescales and key spatial features of the transport of agricultural $\mathrm{NH_3}$

emissions to the mountains during synoptically-driven upslope events? Finally, I have observed (and smelled) the influence of $\mathrm{NH_3}$ emissions on hazy and polluted air conditions in urban areas during the autumn and winter seasons. If other campaigns happen, I would include an in-situ station near an urban site (e.g., Fort Collins) equipped with instruments to measure PM, $\mathrm{NH_3}$, NO_x, wind, and particle composition throughout the duration of the campaign. This could shine light into the frequency of upslope events and their impact on urban air quality. The use of data from low cost sensors such as PurpleAir can unveil the spatial extent of high $\mathrm{PM}_{2.5}$ related to upslope events.

6.5.2 Sampling strategy

One key finding from the $\mathrm{TRANS^2Am}$ observations is the strong variability of $\mathrm{NH_3}$ emissions with time of day. During Phase I and II of $\mathrm{TRANS^2Am}$, we had only five instances where $\mathrm{NH_3}$ EmR from the same plume was sampled at different times between 9:00 and 15:00 LT. Thus, our observations lack a complete picture throughout the day.

Furthermore, reviewers from our first paper suggested that the evolution of $\mathrm{NH_3}$ with respect to $\mathrm{CH_4}$ was new and worth highlighting due to the lack of other observations like ours. Therefore, I suggest that if a similar campaign occurs, the plumes should be sampled in a pseudo-lagrangian manner by following the same air mass at different distances downwind. For a plume from a large facility, like the ones presented in Chapter 4, the plume could be measured 25 km downwind in $\sim$1.2 hours. Then, the airplane could return and resample emissions near the sources (to increase our understanding of $\mathrm{NH_3}$ EmR with respect to time of day) and follow this with another sampling of the plume at a different altitude downwind

Another set of flights could be dedicated to sampling only emission ratios near the facility (<10 km) with one or two curtains, similar to the $\mathrm{TRANS^2Am}$ strategy. However, I recommend increasing the vertical extent to the top of the PBL to understand better the vertical extent and distribution of the $\mathrm{NH_3}$ plume near the source.

If an autumn, winter, or spring campaign is proposed to understand the partitioning of $\mathrm{NH_3}$ to the particle phase, I suggest 1) using the same cutoff for measuring the total volume of particles and the aerosol chemical composition and 2) planning each leg so that at least 2 min are spent in each transect to collect one PILS sample that is representative of the plume. In Chapter 4, I report that horizontal distances are $\sim$12 km large plumes for animal feeding operations. If the airplane were to spend 2-min in each leg, this would require a cruising speed of 360 km h^{-1}. The maximum cruising speed reported for the UWKA is 561 km h^{-1}. However, from our data, I calculated a speed of 126 km h^{-1}, suggesting that longer times could be spent in each leg to retrieve one PILS sample representative of the plume conditions.

6.5.3 Research using satellite data

Satellite retrievals are an exciting tool that has been used to understand the $\mathrm{NH_3}$ distribution globally and regionally (e.g., IASI: Van Damme et al., 2018; CrIS: Shepard et al., 2020). Due to their coarse spatial resolution with respect to the spatial extent of agricultural plumes, it can be challenging to use satellites to study emissions and evolution of $\mathrm{NH_3}$ from individual facilities. New techniques such as oversampling algorithms (Cady-Pereira et al., 2022) provide an opportunity to study plumes from stationary sources such as animal feeding operations. Part of this work contributes to increasing the quantification of $\mathrm{NH_3}$ EmR from many emissions sources and our understanding of the evolution of $\mathrm{NH_3}$ in the near field. However, $\mathrm{NH_3}$ emissions from many small facilities (or big ones that were challenging to measure because of their proximity to urban areas or restricted air spaces) remain uncharacterized. Therefore I recommend 1) devoting a subset of flight hours in a new field campaign to systematically retrieving information useful for the validation of satellite retrievals and 2) using oversampling algorithms for $\mathrm{NH_3}$ and $\mathrm{CH_4}$ satellite retrievals in the region to quantify daily summertime $\mathrm{NH_3}$ EmR from other facilities in northeastern Colorado and across the U.S.

6.5.4 Modeling

Finally, from my modeling work using WRF-Chem to study the transport of NH_3 in Colorado during upslope events, I learned that 1) fine-resolution wind fields improve the evaluation of the model with the in situ observations. In particular, we used the HRRR 3 km output as the input meteorological data for the model. However, note that this requires a larger computational need than the default fields. 2) The agricultural NH_3 emissions used in the model are area sources, which resulted in low values for NH_3 emission rates. I recommend changing NH_3 emission rates from animal agriculture from area to point sources, at least for large facilities (animal capacity > 100,000). Alternatively, modeling experiments that change the area-based NH_3 emission rates by a factor (based on back-of-the-envelope calculations, I suggest using a factor of 2 to start) could result in better agreements between the model and in-situ observations.

Bibliography

[Ackerman et al., 2019] Ackerman, D., Millet, D. B., and Chen, X. (2019). Global Estimates of Inorganic Nitrogen Deposition Across Four Decades. *Global Biogeochemical Cycles*, 33(1):100–107.

[Baron, 2006] Baron, J. S. (2006). Hindcasting Nitrogen Deposition To Determine An Ecological Critical Load. *Ecological Applications*, 16(2):433–439.

[Baron et al., 2011] Baron, J. S., Driscoll, C. T., Stoddard, J. L., and Richer, E. E. (2011). Empirical Critical Loads of Atmospheric Nitrogen Deposition for Nutrient Enrichment and Acidification of Sensitive US Lakes. *BioScience*, 61(8):602–613.

[Baron et al., 2000] Baron, J. S., Rueth, H. M., Wolfe, A. M., Nydick, K. R., Allstott, E. J., Minear, J. T., and Moraska, B. (2000). Ecosystem Responses to Nitrogen Deposition in the Colorado Front Range. *Ecosystems*, 3(4):352–368.

[Bauer et al., 2016] Bauer, S. E., Tsigaridis, K., and Miller, R. (2016). Significant atmospheric aerosol pollution caused by world food cultivation. *Geophysical Research Letters*, 43(10):5394–5400.

[Baumann et al., 1997] Baumann, K., Williams, E. J., Olson, J. A., Harder, J. W., and Fehsenfeld, F. C. (1997). Meteorological characteristics and spatial extent of upslope events during the 1993 Tropospheric OH Photochemistry Experiment. *Journal of Geophysical Research: Atmospheres*, 102(D5):6199–6213.

[Beem et al., 2010] Beem, K. B., Raja, S., Schwandner, F. M., Taylor, C., Lee, T., Sullivan, A. P., Carrico, C. M., McMeeking, G. R., Day, D., Levin, E., Hand, J., Kreidenweis, S. M., Schichtel, B., Malm, W. C., and Collett, J. L. (2010). Deposition of reactive nitrogen during the Rocky Mountain Airborne Nitrogen and Sulfur (RoMANS) study. *Environmental Pollution*, 158(3):862–872.

[Behera et al., 2013] Behera, S. N., Sharma, M., Aneja, V. P., and Balasubramanian, R. (2013). Ammonia in the atmosphere: a review on emission sources, atmospheric chemistry and deposition on terrestrial bodies. *Environmental Science and Pollution Research*, 20(11):8092–8131.

[Benedict et al., 2013a] Benedict, K. B., Carrico, C. M., Kreidenweis, S. M., Schichtel, B., Malm, W. C., and Collett, J. L. (2013a). A seasonal nitrogen deposition budget for Rocky Mountain National Park. *Ecological Applications*, 23(5):1156–1169.

[Benedict et al., 2013b] Benedict, K. B., Day, D., Schwandner, F. M., Kreidenweis, S. M., Schichtel, B., Malm, W. C., and Collett, J. L. (2013b). Observations of atmospheric reactive nitrogen species in Rocky Mountain National Park and across northern Colorado. *Atmospheric Environment*, 64:66–76.

[Benedict et al., 2018] Benedict, K. B., Prenni, A. J., Sullivan, A. P., Evanoski-Cole, A. R., Fischer, E. V., Callahan, S., Sive, B. C., Zhou, Y., Schichtel, B. A., and Collett Jr, J. L. (2018). Impact of Front Range sources on reactive nitrogen concentrations and deposition in Rocky Mountain National Park. *PeerJ*, 6:e4759.

[Bobbink et al., 2010] Bobbink, R., Hicks, K., Galloway, J., Spranger, T., Alkemade, R., Ashmore, M., Bustamante, M., Cinderby, S., Davidson, E., Dentener, F., Emmett, B., Erisman, J.-W., Fenn, M., Gilliam, F., Nordin, A., Pardo, L., and De Vries, W. (2010). Global assessment of nitrogen deposition effects on terrestrial plant diversity: a synthesis. *Ecological Applications*, 20(1):30–59.

[Bowman et al., 2012] Bowman, W. D., Murgel, J., Blett, T., and Porter, E. (2012). Nitrogen critical loads for alpine vegetation and soils in Rocky Mountain National Park. *Journal of Environmental Management*, 103:165–171.

[Brandani et al., 2023] Brandani, C. B., Lee, M., Auvermann, B. W., Parker, D. B., Casey, K. D., Crosman, E. T., Gouvêa, V. N., Beck, M. R., Bush, K. J., Koziel, J. A., Shaw, B., and Brauer,

D. (2023). Mitigating Ammonia Deposition Derived from Open-Lot Livestock Facilities into Colorado's Rocky Mountain National Park: State of the Science. *Atmosphere*, 14(10):1469.

[Burns, 2004] Burns, D. A. (2004). The effects of atmospheric nitrogen deposition in the Rocky Mountains of Colorado and southern Wyoming, USA—a critical review. *Environmental Pollution*, 127(2):257–269.

[Cady-Pereira et al., 2023] Cady-Pereira, K. E., Guo, X., Wang, R., Leytem, A., Calkins, C., Berry, E., Sun, K., Müller, M., Wisthaler, A., Payne, V. H., Shephard, M. W., Zondlo, M. A., and Kantchev, V. H. (2023). Validation of NH $_3$ observations from AIRS and CrIS against aircraft measurements from DISCOVER-AQ and a surface network in the Magic Valley. preprint, Gases/Remote Sensing/Validation and Intercomparisons.

[Cazorla and Juncosa, 2018] Cazorla, M. and Juncosa, J. (2018). Planetary boundary layer evolution over an equatorial Andean valley: A simplified model based on balloon-borne and surface measurements. *Atmospheric Science Letters*, 19(8):e829.

[Clarisse et al., 2009] Clarisse, L., Clerbaux, C., Dentener, F., Hurtmans, D., and Coheur, P.-F. (2009). Global ammonia distribution derived from infrared satellite observations. *Nature Geoscience*, 2(7):479–483.

[Crosson, 2008] Crosson, E. (2008). A cavity ring-down analyzer for measuring atmospheric levels of methane, carbon dioxide, and water vapor. *Applied Physics B*, 92(3):403–408.

[Denmead et al., 2008] Denmead, O. T., Chen, D., Griffith, D. W. T., Loh, Z. M., Bai, M., and Naylor, T. (2008). Emissions of the indirect greenhouse gases NH3 and NOx from Australian beef cattle feedlots. *Australian Journal of Experimental Agriculture*, 48(2):213.

[Eilerman et al., 2016] Eilerman, S. J., Peischl, J., Neuman, J. A., Ryerson, T. B., Aikin, K. C., Holloway, M. W., Zondlo, M. A., Golston, L. M., Pan, D., Floerchinger, C., and Herndon, S. (2016). Characterization of Ammonia, Methane, and Nitrous Oxide Emissions from Concentrated Animal Feeding Operations in Northeastern Colorado. *Environmental Science & Technology*, 50(20):10885–10893.

[Ellis et al., 2010] Ellis, R. A., Murphy, J. G., Pattey, E., van Haarlem, R., O'Brien, J. M., and Herndon, S. C. (2010). Characterizing a Quantum Cascade Tunable Infrared Laser Differential Absorption Spectrometer (QC-TILDAS) for measurements of atmospheric ammonia. *Atmos. Meas. Tech.*

[Fenn et al., 1998] Fenn, M. E., Poth, M. A., Aber, J. D., Baron, J. S., Bormann, B. T., Johnson, D. W., Lemly, A. D., McNulty, S. G., Ryan, D. F., and Stottlemyer, R. (1998). NITROGEN EXCESS IN NORTH AMERICAN ECOSYSTEMS: PREDISPOSING FACTORS, ECOSYSTEM RESPONSES, AND MANAGEMENT STRATEGIES. *Ecological Applications*, 8(3):706–733.

[Fowler et al., 2013] Fowler, D., Coyle, M., Skiba, U., Sutton, M. A., Cape, J. N., Reis, S., Sheppard, L. J., Jenkins, A., Grizzetti, B., Galloway, J. N., Vitousek, P., Leach, A., Bouwman, A. F., Butterbach-Bahl, K., Dentener, F., Stevenson, D., Amann, M., and Voss, M. (2013). The global nitrogen cycle in the twenty-first century. *Philosophical Transactions of the Royal Society B: Biological Sciences*, 368(1621):20130164.

[Galloway et al., 2003] Galloway, J. N., Aber, J. D., Erisman, J. W., Seitzinger, S. P., Howarth, R. W., Cowling, E. B., and Cosby, B. J. (2003). The Nitrogen Cascade. *BioScience*, 53(4):341.

[Gebhart et al., 2014] Gebhart, K. A., Malm, W. C., Rodriguez, M. A., Barna, M. G., Schichtel, B. A., Benedict, K. B., Collett, J. L., and Carrico, C. M. (2014). Meteorological and Back Trajectory Modeling for the Rocky Mountain Atmospheric Nitrogen and Sulfur Study II. *Advances in Meteorology*, 2014:1–19.

[Gebhart et al., 2011] Gebhart, K. A., Schichtel, B. A., Malm, W. C., Barna, M. G., Rodriguez, M. A., and Collett, J. L. (2011). Back-trajectory-based source apportionment of airborne sulfur and nitrogen concentrations at Rocky Mountain National Park, Colorado, USA. *Atmospheric Environment*, 45(3):621–633.

[Golston et al., 2020] Golston, L. M., Pan, D., Sun, K., Tao, L., Zondlo, M. A., Eilerman, S. J., Peischl, J., Neuman, J. A., and Floerchinger, C. (2020). Variability of Ammonia and Methane Emissions from Animal Feeding Operations in Northeastern Colorado. *Environmental Science & Technology*, 54(18):11015–11024.

[Hacker et al., 2016] Hacker, J. M., Chen, D., Bai, M., Ewenz, C., Junkermann, W., Lieff, W., McManus, B., Neininger, B., Sun, J., Coates, T., Denmead, T., Flesch, T., McGinn, S., and Hill, J. (2016). Using airborne technology to quantify and apportion emissions of CH4 and NH3 from feedlots. *Animal Production Science*, 56(3):190.

[Heald et al., 2012] Heald, C. L., Collett, J. L., Lee, T., Benedict, K. B., Schwandner, F. M., Li, Y., Clarisse, L., Hurtmans, D. R., Van Damme, M., Clerbaux, C., Coheur, P.-F., Philip, S., Martin, R. V., and Pye, H. O. T. (2012). Atmospheric ammonia and particulate inorganic nitrogen over the United States. *Atmospheric Chemistry and Physics*, 12(21):10295–10312.

[Holmes, 2018] Holmes, C. D. (2018). Methane Feedback on Atmospheric Chemistry: Methods, Models, and Mechanisms. *Journal of Advances in Modeling Earth Systems*, 10(4):1087–1099.

[Hrdina et al., 2019] Hrdina, A., Moravek, A., Schwartz-Narbonne, H., and Murphy, J. (2019). Summertime Soil-Atmosphere Ammonia Exchange in the Colorado Rocky Mountain Front Range Pine Forest. *Soil Systems*, 3(1):15.

[Huntington and Archibeque, 2000] Huntington, G. B. and Archibeque, S. L. (2000). Practical aspects of urea and ammonia metabolism in ruminants. *Journal of Animal Science*, 77(E-Suppl):1.

[Karydis et al., 2021] Karydis, V. A., Tsimpidi, A. P., Pozzer, A., and Lelieveld, J. (2021). How alkaline compounds control atmospheric aerosol particle acidity. *Atmospheric Chemistry and Physics*, 21(19):14983–15001.

[Kille et al., 2017] Kille, N., Baidar, S., Handley, P., Ortega, I., Sinreich, R., Cooper, O. R., Hase, F., Hannigan, J. W., Pfister, G., and Volkamer, R. (2017). The CU mobile Solar Occultation

Flux instrument: structure functions and emission rates of NH3, NO2 and C2H6. *Atmospheric Measurement Techniques*, 10(1):373–392.

[Kille et al., 2019] Kille, N., Chiu, R., Frey, M., Hase, F., Sha, M. K., Blumenstock, T., Hannigan, J. W., Orphal, J., Bon, D., and Volkamer, R. (2019). Separation of Methane Emissions From Agricultural and Natural Gas Sources in the Colorado Front Range. *Geophysical Research Letters*, 46(7):3990–3998.

[Kim et al., 2006] Kim, S.-W., Heckel, A., McKeen, S. A., Frost, G. J., Hsie, E.-Y., Trainer, M. K., Richter, A., Burrows, J. P., Peckham, S. E., and Grell, G. A. (2006). Satellite-observed U.S. power plant NO $_x$ emission reductions and their impact on air quality. *Geophysical Research Letters*, 33(22):L22812.

[Lassman et al., 2020] Lassman, W., Collett, J. L., Ham, J. M., Yalin, A. P., Shonkwiler, K. B., and Pierce, J. R. (2020). Exploring new methods of estimating deposition using atmospheric concentration measurements: A modeling case study of ammonia downwind of a feedlot. *Agricultural and Forest Meteorology*, 290:107989.

[Li et al., 2016] Li, Y., Schichtel, B. A., Walker, J. T., Schwede, D. B., Chen, X., Lehmann, C. M. B., Puchalski, M. A., Gay, D. A., and Collett, J. L. (2016). Increasing importance of deposition of reduced nitrogen in the United States. *Proceedings of the National Academy of Sciences*, 113(21):5874–5879.

[Li et al., 2017] Li, Y., Thompson, T. M., Van Damme, M., Chen, X., Benedict, K. B., Shao, Y., Day, D., Boris, A., Sullivan, A. P., Ham, J., Whitburn, S., Clarisse, L., Coheur, P.-F., and Collett Jr., J. L. (2017). Temporal and spatial variability of ammonia in urban and agricultural regions of northern Colorado, United States. *Atmospheric Chemistry and Physics*, 17(10):6197–6213.

[Lieb et al., 2011] Lieb, A. M., Darrouzet-Nardi, A., and Bowman, W. D. (2011). Nitrogen deposition decreases acid buffering capacity of alpine soils in the southern Rocky Mountains. *Geoderma*, 164(3-4):220–224.

[Lindaas et al., 2021] Lindaas, J., Pollack, I. B., Garofalo, L. A., Pothier, M. A., Farmer, D. K., Kreidenweis, S. M., Campos, T. L., Flocke, F., Weinheimer, A. J., Montzka, D. D., Tyndall, G. S., Palm, B. B., Peng, Q., Thornton, J. A., Permar, W., Wielgasz, C., Hu, L., Ottmar, R. D., Restaino, J. C., Hudak, A. T., Ku, I., Zhou, Y., Sive, B. C., Sullivan, A., Collett, J. L., and Fischer, E. V. (2021). Emissions of Reactive Nitrogen From Western U.S. Wildfires During Summer 2018. *Journal of Geophysical Research: Atmospheres*, 126(2):e2020JD032657.

[Liu et al., 2022] Liu, L., Xu, W., Lu, X., Zhong, B., Guo, Y., Lu, X., Zhao, Y., He, W., Wang, S., Zhang, X., Liu, X., and Vitousek, P. (2022). Exploring global changes in agricultural ammonia emissions and their contribution to nitrogen deposition since 1980. *Proceedings of the National Academy of Sciences*, 119(14):e2121998119.

[Malm et al., 2013] Malm, W. C., Schichtel, B. A., Barna, M. G., Gebhart, K. A., Rodriguez, M. A., Collett, J. L., Carrico, C. M., Benedict, K. B., Prenni, A. J., and Kreidenweis, S. M. (2013). Aerosol species concentrations and source apportionment of ammonia at Rocky Mountain National Park. *Journal of the Air & Waste Management Association*, 63(11):1245–1263.

[Marple et al., 1991] Marple, V. A., Rubow, K. L., and Behm, S. M. (1991). A Microorifice Uniform Deposit Impactor (MOUDI): Description, Calibration, and Use. *Aerosol Science and Technology*, 14(4):434–446.

[McCabe et al., 2023] McCabe, M. E., Pollack, I. B., Fischer, E. V., Steinmann, K. M., and Caulton, D. R. (2023). Technical note: Isolating methane emissions from animal feeding operations in an interfering location. *Atmospheric Chemistry and Physics*, 23(13):7479–7494.

[McGinn et al., 2007] McGinn, S. M., Flesch, T. K., Crenna, B. P., Beauchemin, K. A., and Coates, T. (2007). Quantifying Ammonia Emissions from a Cattle Feedlot using a Dispersion Model. *Journal of Environmental Quality*, 36(6):1585–1590.

[McManus, 2010] McManus, J. B. (2010). Application of quantum cascade lasers to high-precision atmospheric trace gas measurements. *Optical Engineering*, 49(11):111124.

[McManus et al., 1995] McManus, J. B., Kebabian, P. L., and Zahniser, M. S. (1995). Astigmatic mirror multipass absorption cells for long-path-length spectroscopy. *Applied Optics*, 34(18):3336.

[Meng et al., 2017] Meng, W., Zhong, Q., Yun, X., Zhu, X., Huang, T., Shen, H., Chen, Y., Chen, H., Zhou, F., Liu, J., Wang, X., Zeng, E. Y., and Tao, S. (2017). Improvement of a Global High-Resolution Ammonia Emission Inventory for Combustion and Industrial Sources with New Data from the Residential and Transportation Sectors. *Environmental Science & Technology*, 51(5):2821–2829.

[Mesinger et al., 2006] Mesinger, F., DiMego, G., Kalnay, E., Mitchell, K., Shafran, P. C., Ebisuzaki, W., Jović, D., Woollen, J., Rogers, E., Berbery, E. H., Ek, M. B., Fan, Y., Grumbine, R., Higgins, W., Li, H., Lin, Y., Manikin, G., Parrish, D., and Shi, W. (2006). North American Regional Reanalysis. *Bulletin of the American Meteorological Society*, 87(3):343–360.

[Miller et al., 2015] Miller, D. J., Sun, K., Tao, L., Pan, D., Zondlo, M. A., Nowak, J. B., Liu, Z., Diskin, G., Sachse, G., Beyersdorf, A., Ferrare, R., and Scarino, A. J. (2015). Ammonia and methane dairy emission plumes in the San Joaquin Valley of California from individual feedlot to regional scales. *Journal of Geophysical Research: Atmospheres*, 120(18):9718–9738.

[Myhre et al., 2013] Myhre, G., Shindell, D., Bréon, F.-M., Collins, W., Fuglestvedt, J., Huang, J., Koch, D., Lamarque, J.-F., Lee, D., Mendoza, B., Nakajima, T., Robock, A., Stephens, G., Zhang, H., Aamaas, B., Boucher, O., Dalsøren, S. B., Daniel, J. S., Forster, P., Granier, C., Haigh, J., Hodnebrog, , Kaplan, J. O., Marston, G., Nielsen, C. J., O'Neill, B. C., Peters, G. P., Pongratz, J., Ramaswamy, V., Roth, R., Rotstayn, L., Smith, S. J., Stevenson, D., Vernier, J.-P., Wild, O., Young, P., Jacob, D., Ravishankara, A. R., and Shine, K. (2013). Anthropogenic and Natural Radiative Forcing. In: Climate Change Cambridge, United Kingdom and New York, NY, USA. *Cambridge University Press*, pages 1–44.

[Ndegwa et al., 2008] Ndegwa, P., Hristov, A., Arogo, J., and Sheffield, R. (2008). A review of ammonia emission mitigation techniques for concentrated animal feeding operations. *Biosystems Engineering*, 100(4):453–469.

[Nemitz et al., 2001] Nemitz, E., Milford, C., and Sutton, M. A. (2001). A two-layer canopy compensation point model for describing bi-directional biosphere-atmosphere exchange of ammonia. *Quarterly Journal of the Royal Meteorological Society*, 127(573):815–833.

[Neuman et al., 2003] Neuman, J. A., Ryerson, T. B., Huey, L. G., Jakoubek, R., Nowak, J. B., Simons, C., and Fehsenfeld, F. C. (2003). Calibration and Evaluation of Nitric Acid and Ammonia Permeation Tubes by UV Optical Absorption. *Environmental Science & Technology*, 37(13):2975–2981.

[Nowak et al., 2012] Nowak, J. B., Neuman, J. A., Bahreini, R., Middlebrook, A. M., Holloway, J. S., McKeen, S. A., Parrish, D. D., Ryerson, T. B., and Trainer, M. (2012). Ammonia sources in the California South Coast Air Basin and their impact on ammonium nitrate formation: SOUTH COAST AIR BASIN AMMONIA SOURCES. *Geophysical Research Letters*, 39(7):n/a–n/a.

[Orsini et al., 2003] Orsini, D. A., Ma, Y., Sullivan, A., Sierau, B., Baumann, K., and Weber, R. J. (2003). Refinements to the particle-into-liquid sampler (PILS) for ground and airborne measurements of water soluble aerosol composition. *Atmospheric Environment*, 37(9-10):1243–1259.

[Pan et al., 2021] Pan, D., Benedict, K. B., Golston, L. M., Wang, R., Collett, J. L., Tao, L., Sun, K., Guo, X., Ham, J., Prenni, A. J., Schichtel, B. A., Mikoviny, T., Müller, M., Wisthaler, A., and Zondlo, M. A. (2021). Ammonia Dry Deposition in an Alpine Ecosystem Traced to Agricultural Emission Hotpots. *Environmental Science & Technology*, 55(12):7776–7785.

[Piña et al., 2019] Piña, A. J., Schumacher, R. S., Denning, A. S., Faulkner, W. B., Baron, J. S., Ham, J., Ojima, D. S., and Collett, J. L. (2019). Reducing Wet Ammonium Deposition in Rocky Mountain National Park: the Development and Evaluation of A Pilot Early Warning System for Agricultural Operations in Eastern Colorado. *Environmental Management*, 64(5):626–639.

[Pleim et al., 2019] Pleim, J. E., Ran, L., Appel, W., Shephard, M. W., and Cady-Pereira, K. (2019). New Bidirectional Ammonia Flux Model in an Air Quality Model Coupled With an Agricultural Model. *Journal of Advances in Modeling Earth Systems*, 11(9):2934–2957.

[Pollack et al., 2019] Pollack, I. B., Lindaas, J., Roscioli, J. R., Agnese, M., Permar, W., Hu, L., and Fischer, E. V. (2019). Evaluation of ambient ammonia measurements from a research aircraft using a closed-path QC-TILDAS operated with active continuous passivation. *Atmospheric Measurement Techniques*, 12(7):3717–3742.

[Pollack et al., 2022] Pollack, I. B., McCabe, M. E., Caulton, D. R., and Fischer, E. V. (2022). Enhancements in Ammonia and Methane from Agricultural Sources in the Northeastern Colorado Front Range Using Observations from a Small Research Aircraft. *Environmental Science & Technology*, 56(4):2236–2247.

[Roscioli et al., 2016] Roscioli, J. R., Zahniser, M. S., Nelson, D. D., Herndon, S. C., and Kolb, C. E. (2016). New Approaches to Measuring Sticky Molecules: Improvement of Instrumental Response Times Using Active Passivation. *The Journal of Physical Chemistry A*, 120(9):1347–1357.

[Sander, 1999] Sander, R. (1999). Modeling Atmospheric Chemistry: Interactions between Gas-Phase Species and Liquid Cloud/Aerosol Particles. *Surveys in Geophysics*, 20(1):1–31.

[Shonkwiler and Ham, 2018] Shonkwiler, K. B. and Ham, J. M. (2018). Ammonia emissions from a beef feedlot: Comparison of inverse modeling techniques using long-path and point measurements of fenceline NH3. *Agricultural and Forest Meteorology*, 258:29–42.

[Snider et al., 2018] Snider, J., Petters, M., Takagi, H., Liu, P., Lukens, D., Glover, B., Deshler, T., Montague, D., Wechsler, P., Vali, G., Rogers, D., and Kelly, B. (2018). The NCAR-UWyo Aerosol Inlet. White paper.

[Staebler et al., 2009] Staebler, R. M., McGinn, S. M., Crenna, B. P., Flesch, T. K., Hayden, K. L., and Li, S.-M. (2009). Three-dimensional characterization of the ammonia plume from a beef cattle feedlot. *Atmospheric Environment*, 43(38):6091–6099.

[Sullivan et al., 2022] Sullivan, A. P., Pokhrel, R. P., Shen, Y., Murphy, S. M., Toohey, D. W., Campos, T., Lindaas, J., Fischer, E. V., and Collett Jr., J. L. (2022). Examination of brown carbon absorption from wildfires in the western US during the WE-CAN study. *Atmospheric Chemistry and Physics*, 22(20):13389–13406.

[Sullivan et al., 2016] Sullivan, J. T., McGee, T. J., Langford, A. O., Alvarez, R. J., Senff, C. J., Reddy, P. J., Thompson, A. M., Twigg, L. W., Sumnicht, G. K., Lee, P., Weinheimer, A., Knote, C., Long, R. W., and Hoff, R. M. (2016). Quantifying the contribution of thermally driven recirculation to a high-ozone event along the Colorado Front Range using lidar: O_3 LIDAR DURING RECIRCULATION EVENT. *Journal of Geophysical Research: Atmospheres*, 121(17):10,377–10,390.

[Sun et al., 2015] Sun, K., Tao, L., Miller, D. J., Zondlo, M. A., Shonkwiler, K. B., Nash, C., and Ham, J. M. (2015). Open-path eddy covariance measurements of ammonia fluxes from a beef cattle feedlot. *Agricultural and Forest Meteorology*, 213:193–202.

[Sutton et al., 2008] Sutton, M. A., Erisman, J. W., Dentener, F., and Möller, D. (2008). Ammonia in the environment: From ancient times to the present. *Environmental Pollution*, 156(3):583–604.

[Thompson et al., 2015] Thompson, T. M., Rodriguez, M. A., Barna, M. G., Gebhart, K. A., Hand, J. L., Day, D. E., Malm, W. C., Benedict, K. B., Collett, J. L., and Schichtel, B. A. (2015). Rocky Mountain National Park reduced nitrogen source apportionment. *Journal of Geophysical Research: Atmospheres*, 120(9):4370–4384.

[Tong et al., 2015] Tong, D. Q., Lamsal, L., Pan, L., Ding, C., Kim, H., Lee, P., Chai, T., Pickering, K. E., and Stajner, I. (2015). Long-term NOx trends over large cities in the United States during the great recession: Comparison of satellite retrievals, ground observations, and emission inventories. *Atmospheric Environment*, 107:70–84.

[Van Damme et al., 2018] Van Damme, M., Clarisse, L., Whitburn, S., Hadji-Lazaro, J., Hurtmans, D., Clerbaux, C., and Coheur, P.-F. (2018). Industrial and agricultural ammonia point sources exposed. *Nature*, 564(7734):99–103.

[Wolfe et al., 2001] Wolfe, A. P., Baron, J. S., and Cornett, R. J. (2001). Anthropogenic nitrogen deposition induces rapid ecological changes in alpine lakes of the Colorado Front Range (USA). *Journal of Paleolimnology*, 25:1–7.

[Wolfe et al., 2003] Wolfe, A. P., Van Gorp, A. C., and Baron, J. S. (2003). Recent ecological and biogeochemical changes in alpine lakes of Rocky Mountain National Park (Colorado, USA): a response to anthropogenic nitrogen deposition. *Geobiology*, 1(2):153–168.

[Wyer et al., 2022] Wyer, K. E., Kelleghan, D. B., Blanes-Vidal, V., Schauberger, G., and Curran, T. P. (2022). Ammonia emissions from agriculture and their contribution to fine particulate matter: A review of implications for human health. *Journal of Environmental Management*, 323:116285.

[Xu et al., 2019] Xu, R., Tian, H., Pan, S., Prior, S. A., Feng, Y., Batchelor, W. D., Chen, J., and Yang, J. (2019). Global ammonia emissions from synthetic nitrogen fertilizer applications in agricultural systems: Empirical and process-based estimates and uncertainty. *Global Change Biology*, 25(1):314–326.

[Yacovitch et al., 2014] Yacovitch, T. I., Herndon, S. C., Roscioli, J. R., Floerchinger, C., McGovern, R. M., Agnese, M., Pétron, G., Kofler, J., Sweeney, C., Karion, A., Conley, S. A., Kort, E. A., Nähle, L., Fischer, M., Hildebrandt, L., Koeth, J., McManus, J. B., Nelson, D. D., Zahniser, M. S., and Kolb, C. E. (2014). Demonstration of an Ethane Spectrometer for Methane Source Identification. *Environmental Science & Technology*, 48(14):8028–8034.

[Yang et al., 2016] Yang, Y., Liao, W., Wang, X., Liu, C., Xie, Q., Gao, Z., Ma, W., and He, Y. (2016). Quantification of ammonia emissions from dairy and beef feedlots in the Jing-Jin-Ji district, China. *Agriculture, Ecosystems & Environment*, 232:29–37.

[Zahniser et al., 1995] Zahniser, M. S., David D. Nelson, J. Barry McManus, and Paul L. Kebabian (1995). Measurement of trace gas fluxes using tunable diode laser spectroscopy. *Philosophical Transactions of the Royal Society of London*, 351(1696):371–382.

[Zhan et al., 2017] Zhan, X., Bo, Y., Zhou, F., Liu, X., Paerl, H. W., Shen, J., Wang, R., Li, F., Tao, S., Dong, Y., and Tang, X. (2017). Evidence for the Importance of Atmospheric Nitrogen Deposition to Eutrophic Lake Dianchi, China. *Environmental Science & Technology*, 51(12):6699–6708.

[Zhu et al., 2015] Zhu, L., Henze, D. K., Bash, J. O., Cady-Pereira, K. E., Shephard, M. W., Luo, M., and Capps, S. L. (2015). Sources and Impacts of Atmospheric NH3: Current Understanding and Frontiers for Modeling, Measurements, and Remote Sensing in North America. *Current Pollution Reports*, 1(2):95–116.

Appendix A

Supplementary information for Chapter 2

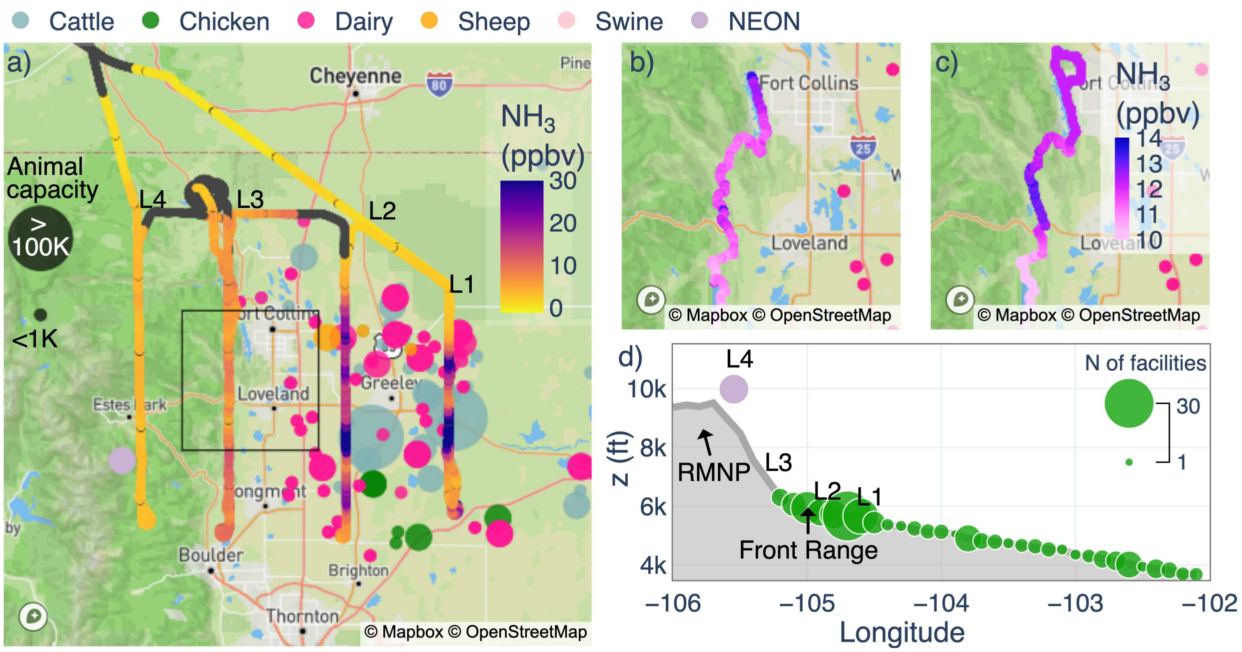

Figure A.1: a) Flight track of the UWKA colored by NH_3 (ppbv) on August 29, 2022, between 11:15 and 15:15 local time (MT). This flight track is representative of the upslope-focused sampling during Phase I and Phase II of $\mathrm{TRANS^2Am}$. Dots represent agricultural facilities colored by the type of animal and sized by the reported maximum capacity. The box shows the area included in panels b) and c). b) Southbound transect of the mobile laboratory colored by NH_3 (ppbv) on August 29, 2022, between 14:30 and 16:30 local time. c) Same as panel b) but showing the northbound transect collected between 16:30 and 18:30 local time. d) Longitudinal average (every 0.1°) of the terrain for the study region (i.e., northeastern Colorado). The size of the green dots represents the number of facilities located at each longitude. The N-S bounds used for this terrain profile are 39 - 41.75 °N.

Mobile Lab Payload

An instrumented hybrid Chevrolet Tahoe ‘’plume tracker” (Hecobian et al., 2019) was deployed periodically in tandem with the aircraft to measure CH_4 and NH_3 at the surface. The Tahoe was equipped with a Picarro G2508 analyzer (Picarro, Santa Clara, CA), which made measurements using cavity ring-down spectroscopy (CRDS) every 15 s, in conjunction with an A0941 mobile measurement kit (Picarro, Santa Clara, CA). The Picarro sampled from a short ¼” diameter Teflon line that passed through the roof of the mobile lab. The inlet line was heated to 40 ºC to limit the loss of gaseous $\mathrm{NH_3}$. Before installation in the Tahoe, the Picarro's calibration was verified by standard addition of known mixing ratios of $\mathrm{NH_3}$ and $\mathrm{CH_4}$ from certified calibration sources (e.g., a gas cylinder for $\mathrm{CH_4}$, and a gas cylinder and a permeation device for $\mathrm{NH_3}$). Zero measurements were made by overflowing the inlet with ultra-high purity zero air. An A21 Global Position System (GPS, Hemisphere GNSS Inc., AZ, USA) and Climatronics' SonimometerTM (P/N 102779-A1-C1-D0; Climatronics Co., NY, USA) for measuring the wind speed and direction, respectively, were mounted 3m above the ground at the front of the plume tracker. The Picarro and meteorological data were displayed in real-time on a laptop inside the vehicle to help identify the interception of a plume.

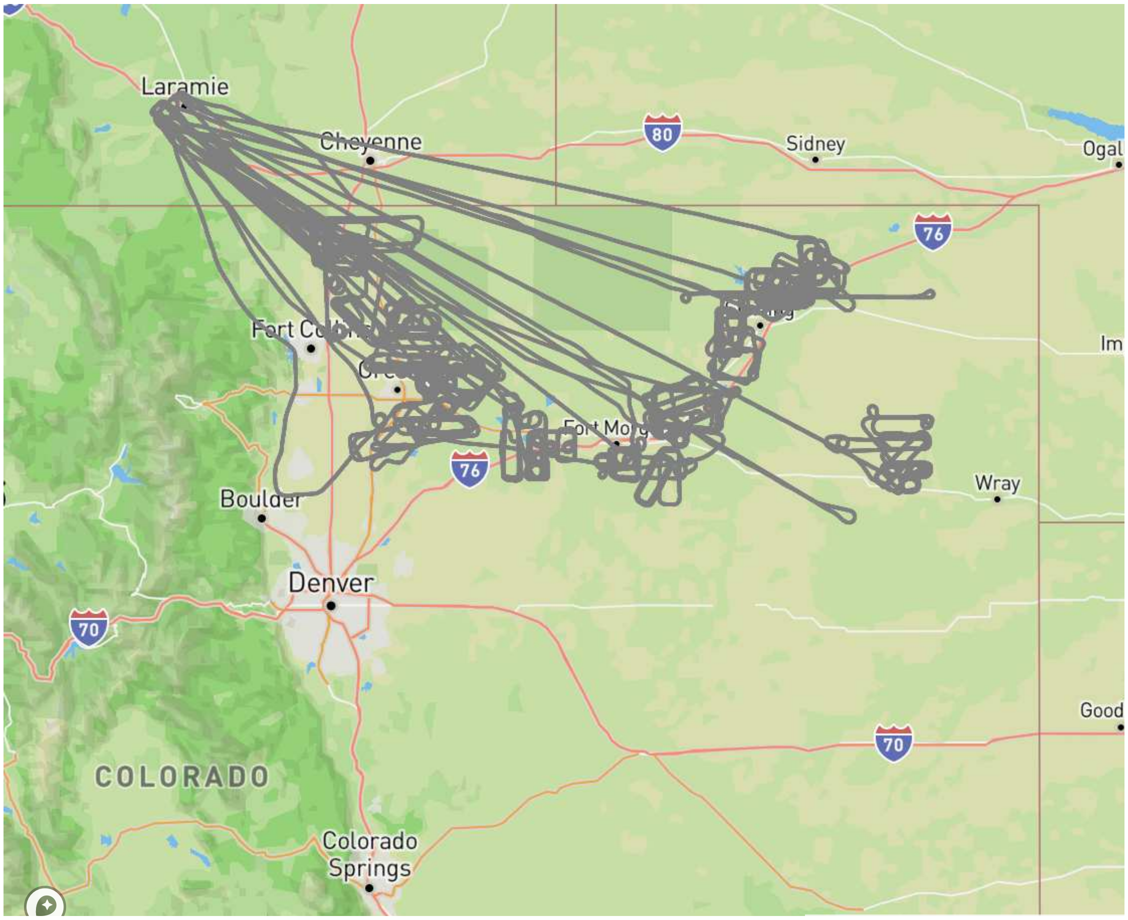

Figure A.2: Flight tracks of the UWKA during Phase I of $\mathrm{TRANS^2Am}$ for 12 near-field sampling flights.

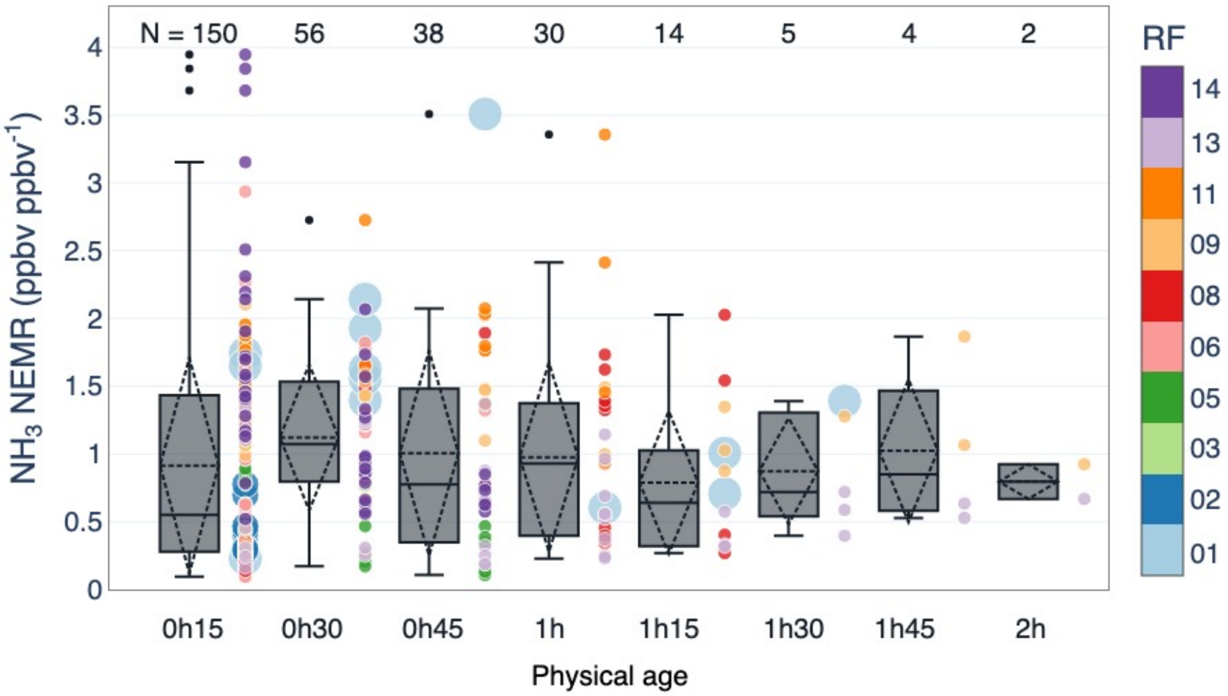

Figure A.3: Transect-specific NH_3 NEMR as a function of physical age. The points represented by the boxplots are colored by the research flight. Points for RF01 (light blue) and RF02 (dark blue) were made larger intentionally to prevent masking from other data points. The lower and upper ends of the boxes span from quartile 1 (Q1) to quartile 3 (Q3). The whiskers correspond to the box edges ±1.5 the interquartile range (IQR: Q3-Q1). N indicates the number of transects in each box plot.

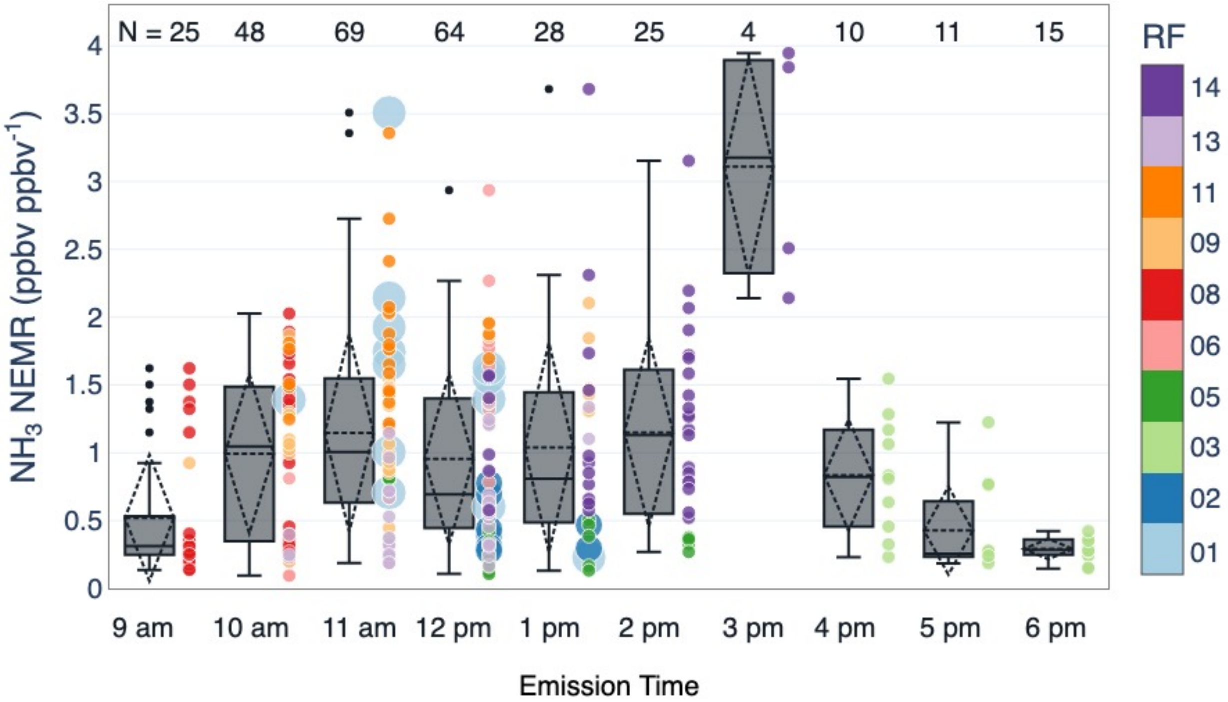

Figure A.4: Transect-specific NH$_3$ NEMR as a function of emissions time (see Section 2.5.1). The points represented by the boxplots are colored by the research flight. Points for RF01 (light blue) and RF02 (dark blue) were made larger intentionally to prevent masking from other data points. The lower and upper ends of the boxes span from quartile 1 (Q1) to quartile 3 (Q3). The whiskers correspond to the box edges ±1.5 the interquartile range (IQR: Q3-Q1). N indicates the number of transects in each box plot.

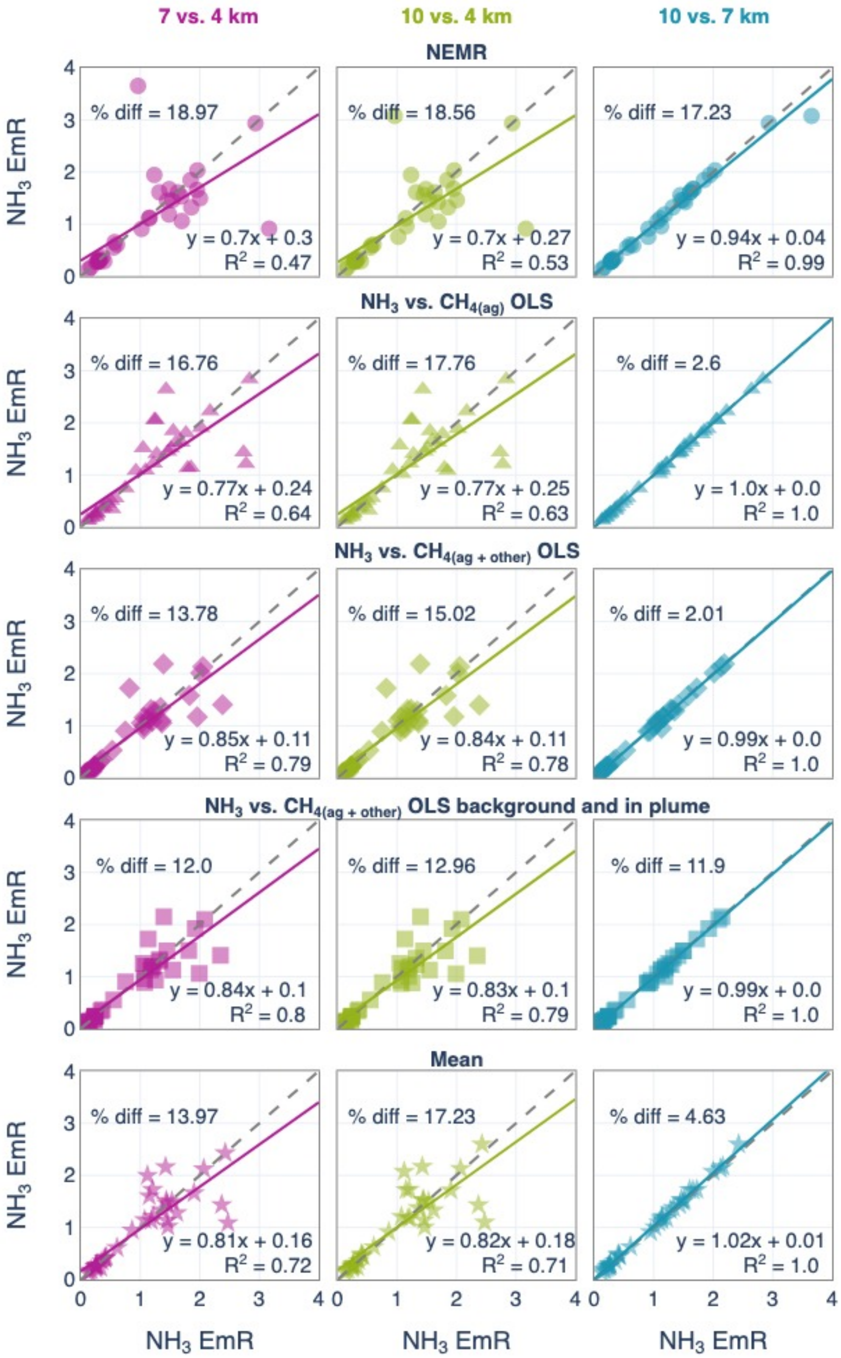

Figure A.5: Sensitivity analysis for estimates of NH_3 EmR using different distances from the center of the targeted facility: 4 (128 transects), 7 (199 transects), and 10 km (235 transects) (approximately 2.5, 4.3, and 6 miles, respectively). Color (columns) show a comparison between distances: pink (col 1) shows NH_3 EmR estimates for 7 vs. 4 km; green (col 2) 10 vs. 4 km; and blue (col 3) 10 vs. 7 km. Different symbols (rows) show the different methods detailed in Figure 2 and Section 2.5. The stars (last row) show the mean of the four methods presented as bars in Figure 2.

Table A.1: Estimated $\mathrm{NH_3}$ EmR. Ttop: mean (std) and bottom: median (range) at different distances from targeted facilities by cattle, dairy, and both combined.

	Cattle	Dairy	All
< 4 km	1.25 (0.68) 1.29 (0.13 - 2.47)	0.31 (0.07) 0.28 (0.25 - 0.43)	1.01 (0.72) 1.12 (0.13 - 2.47)
< 7 km	1.22 (0.64) 1.25 (0.13 - 2.43)	0.3 (0.08) 0.26 (0.21 - 0.43)	0.98 (0.68) 1.09 (0.13 - 2.43)
<10 km	1.2 (0.63) 1.21 (0.13 - 2.43)	0.29 (0.08) 0.26 (0.21 - 0.43)	0.97 (0.68) 1.09 (0.13 - 2.43)

Figure A5 shows that there is little difference between $\mathrm{NH_3}$ EmRs calculated using data collected at different distances downwind from targeted facilities. The correlation between $\mathrm{NH_3}$ EmR based on data collected at 7 and 10 km downwind falls almost exactly in the 1:1 line (third column or blue symbols). This indicates that little to no change in $\mathrm{NH_3}$ EmR occurred between 7 to 10 km of distance from a facility. A difference is identified between estimates based on data collected 4 km downwind versus collected at larger distances (7 and 10 km), first column or pink symbols and second column or green symbols, respectively. In general, the linear regressions show that the estimated $\mathrm{NH_3}$ EmR are larger for the estimates based on data collected 4 km than those based on data collected at larger distances downwind. This is shown by the slope value less than 1 (note that x = shorter distance and y = longer distance). This could be explained by loss processes such as deposition or partitioning to the particle phase. However, during $\mathrm{TRANS^2Am}$, we found that $\mathrm{NH_4}^+$ was less than 15% of the observed NHx.

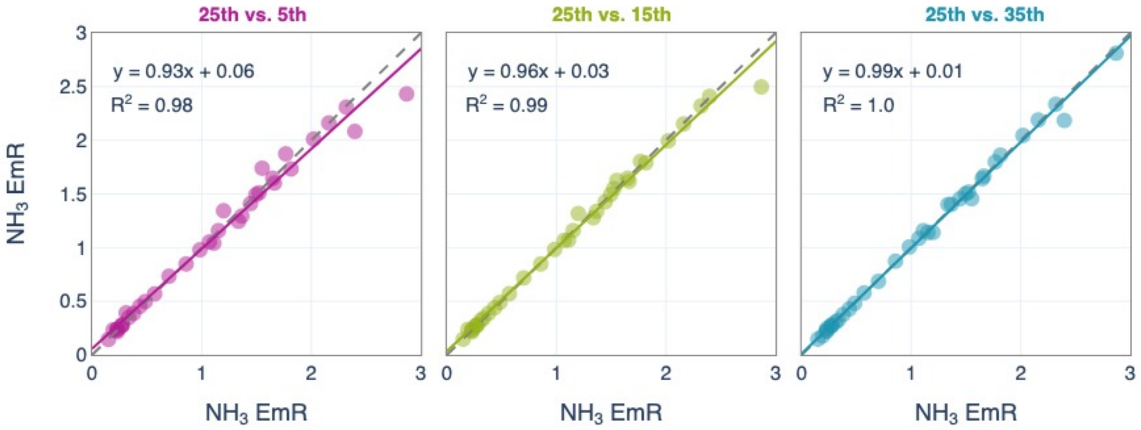

Figure A.6: Sensitivity analysis for estimates of $\mathrm{NH_3}$ EmR using different background cutoffs at $\mathrm{NH_3} <$ 5th (pink), 15th (green), and 35th (blue) percentile compared to the 25th percentile used in the main text.

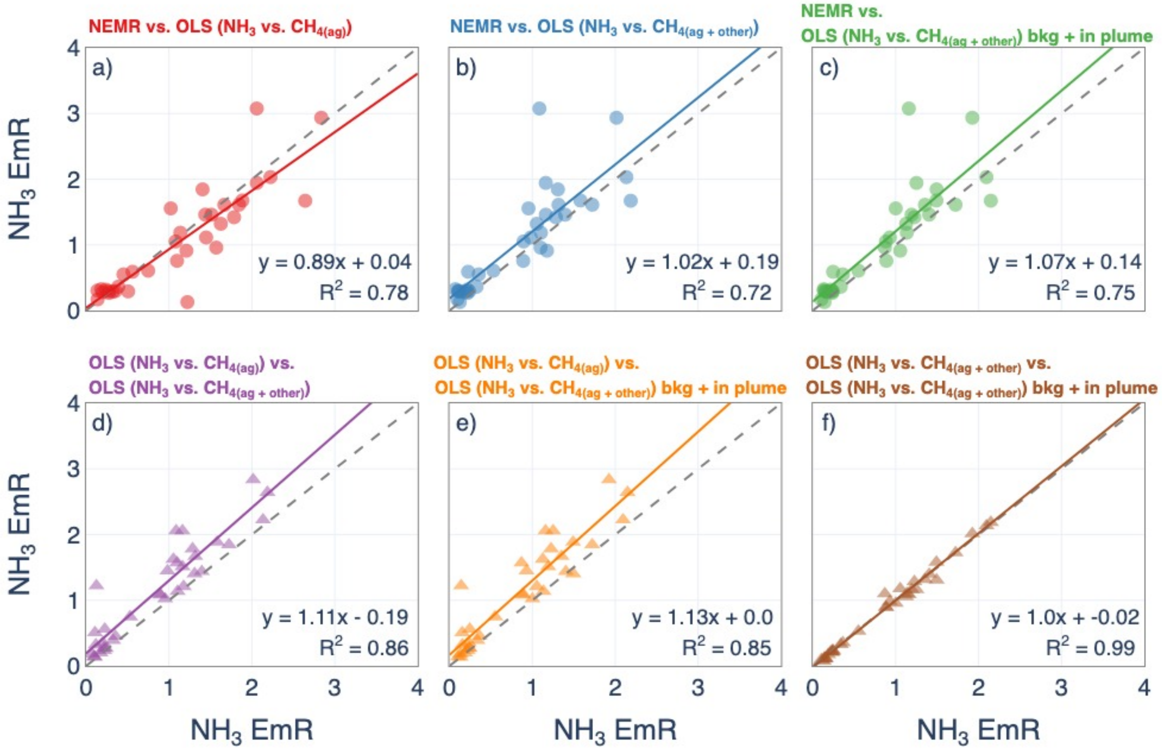

Figure A.7: Sensitivity analysis for estimated $\mathrm{NH_3}$ EmR using different methods at 10 km from the targeted facility.

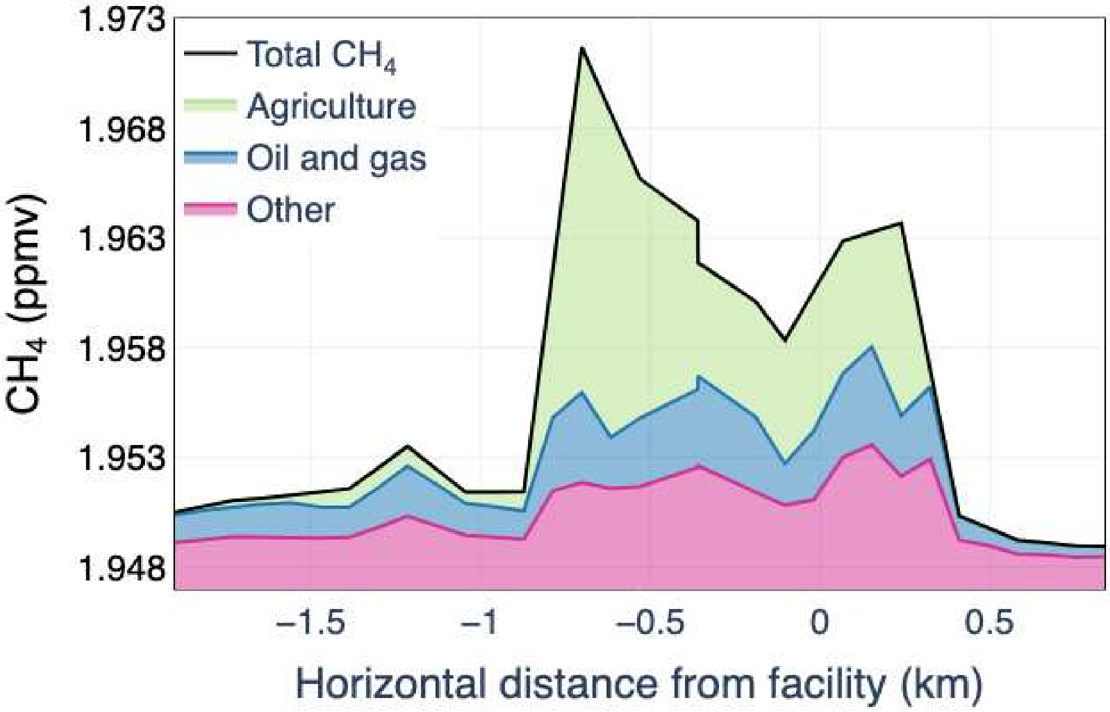

Figure A.8: Same example transect for CH_4 as shown in Figure 2.1d but colored by emission source. Each color indicates the magnitude of CH_4 attributed to the different emissions sources.

Table A.2: Coefficients and regression scores for linear regression with multiple predictors for each facility. Regression scores refers to the proportion of variation in the dependent variable that can be explained by the multiple regression model based on the independent variables.

Facility	RF	β_0	β_1	β_2	Regression score
F01	RF01	3.28	7.42	0.64	0.47
F02 - F03	RF02	0.49	7.37	1.65	0.73
F04	RF03	3.12	10.47	0.87	0.55
F05	RF03	-0.40	5.32	3.49	0.81
F08 - F09	RF05	0.86	15.16	1.91	0.71
F07	RF05	1.14	15.55	2.26	0.93
F12	RF06	8.55	4.05	0.58	0.65
F13, F14, F15	RF06	10.94	-2.80	0.76	0.77
F19, F23, F24, F25	RF08	5.60	6.94	2.55	0.56
F01	RF09	5.35	-1.17	0.90	0.59
F11, F20, F21, F22	RF09	0.51	9.07	0.46	0.60
F27, F28	RF11	1.51	6.07	0.56	0.83
F29	RF13	17.63	8.57	3.04	0.60
F04	RF13	7.85	15.56	0.74	0.88
F13, F14, F15, F16	RF14	1.32	13.50	0.47	0.70

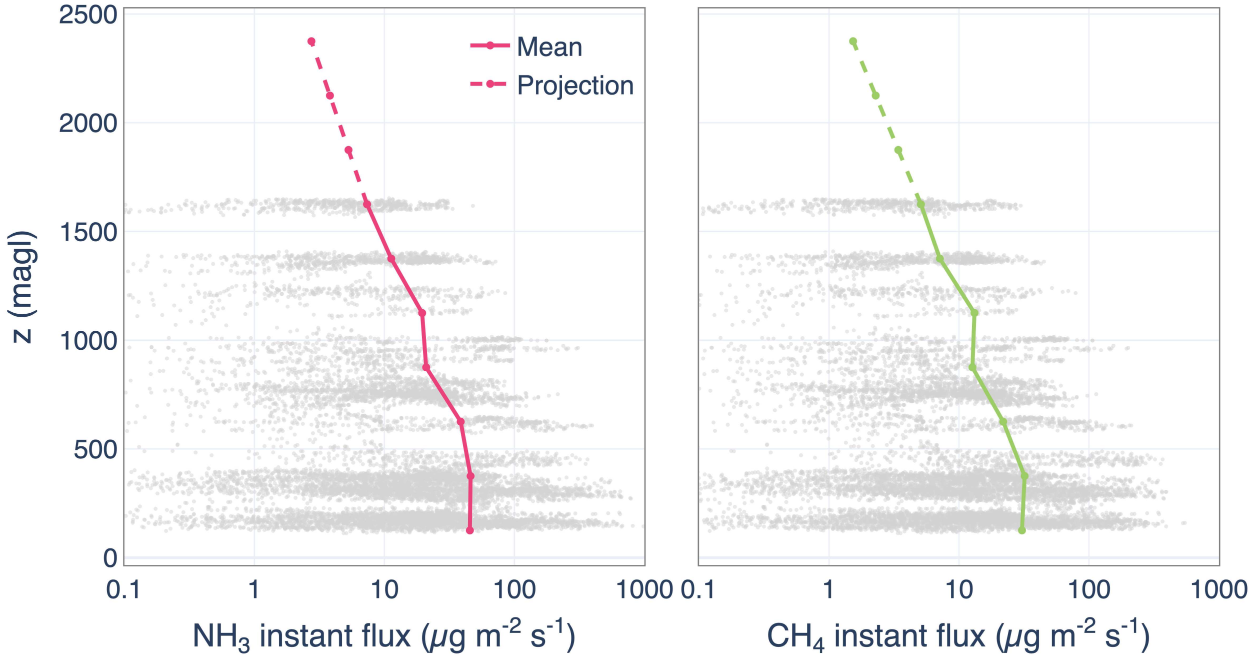

Figure A.9: Vertical average profile for NH_3 (a) and CH_{4_ag} (b) instant fluxes. The gray tracers show all the data for each tracer. The solid line shows the average of each 250 m bin. The dashed line shows the estimated profile up to 2500 magl using the smallest positive slope from the average vertical profile.

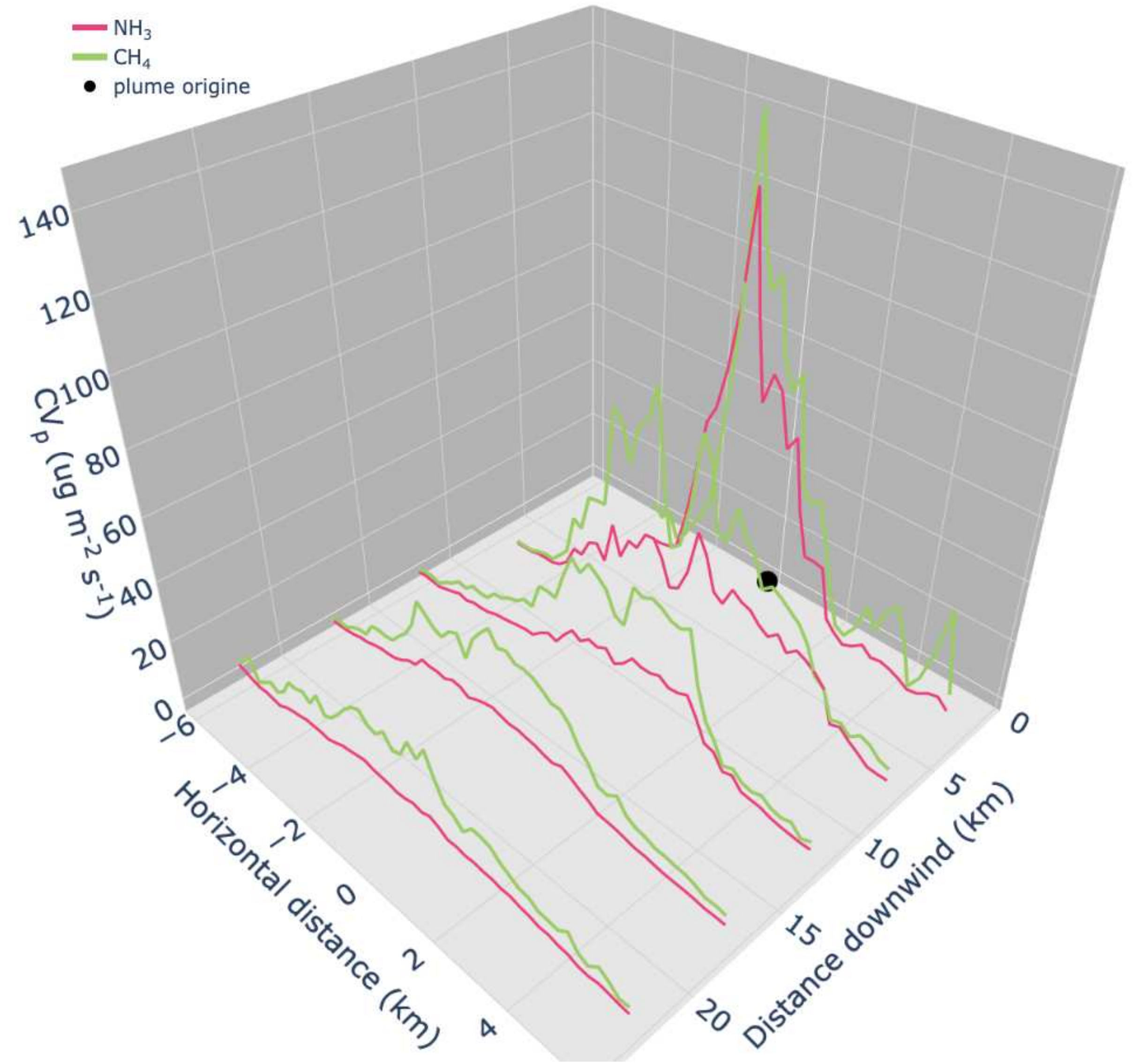

Figure A.10: NH_3 (pink) and CH_{4_ag} (green) horizontal and downwind average profiles with respect to the center of the facility (i.e., plume origin; back dot at (0,0)). The z-axis represents the average instant flux for each tracer.

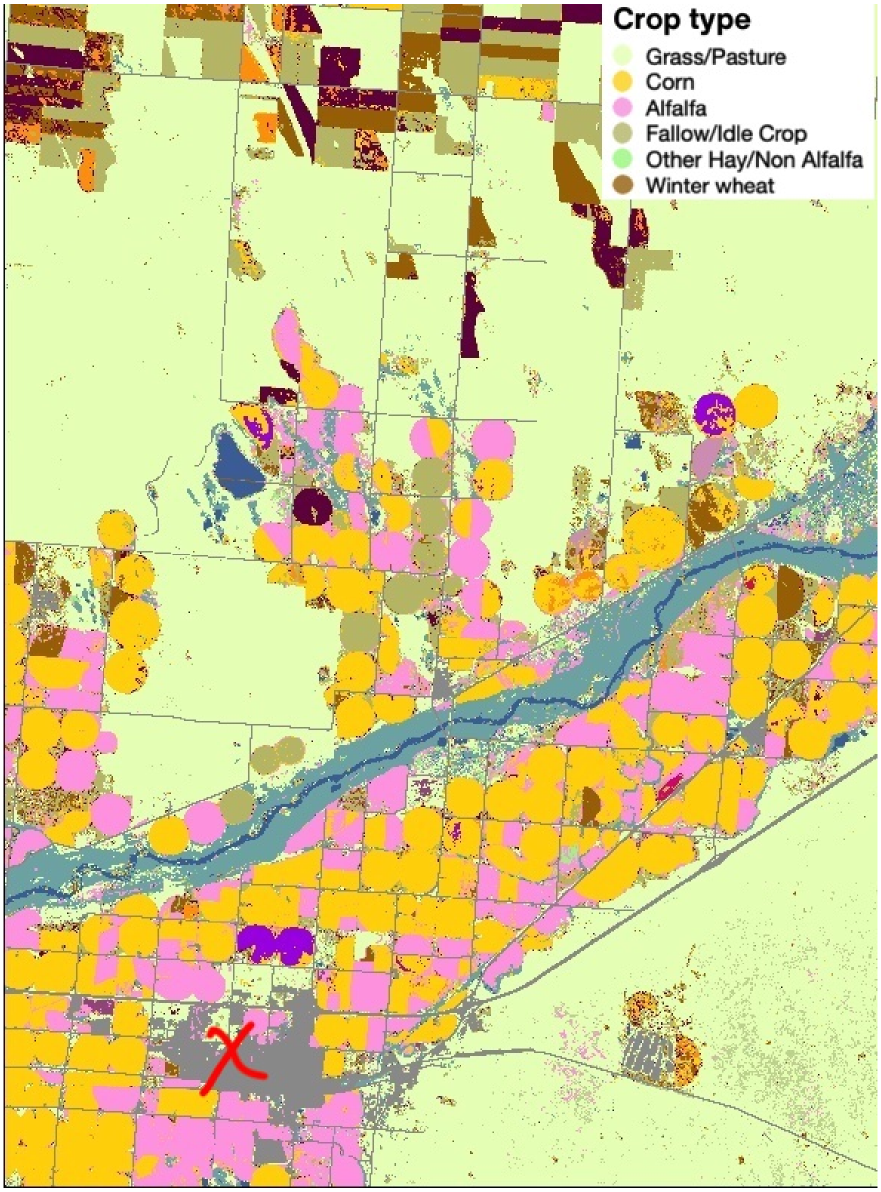

Figure A.11: Crop types for the surface underneath the plume originating from F01 sampled during RF09.

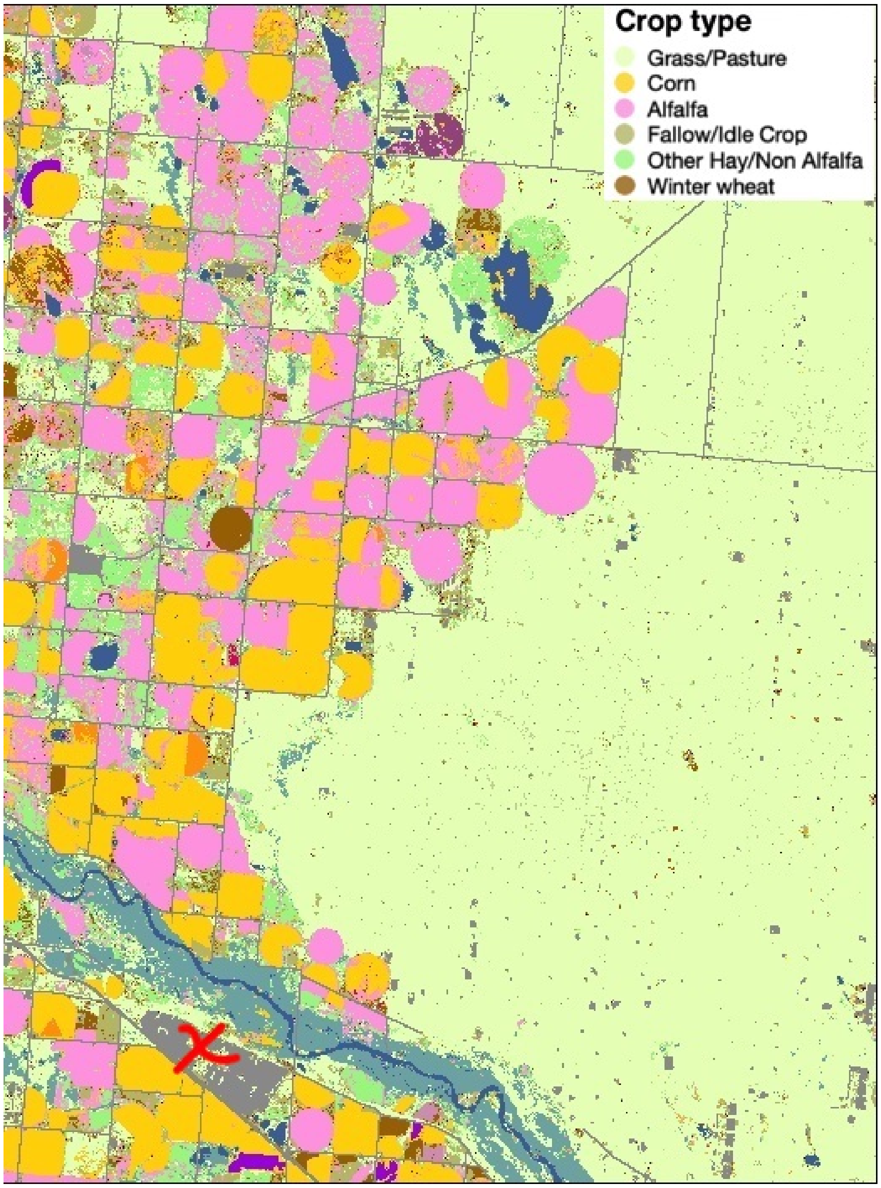

Figure A.12: Crop types for the surface underneath the plume originating from F04 sampled during RF13.

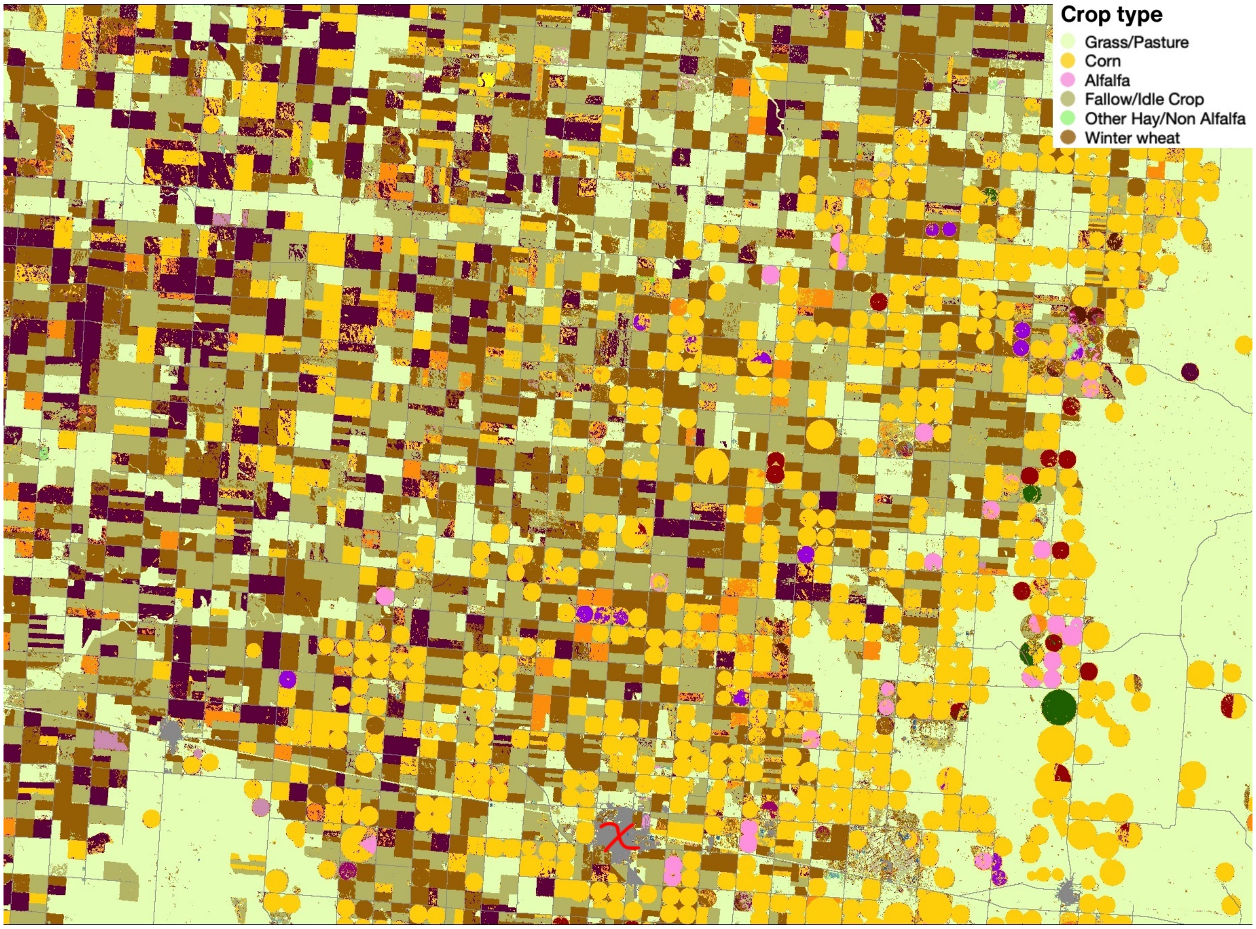

Figure A.13: Crop types for the surface underneath the plume originating from F04 sampled during RF11, RF19, and RF22.

Appendix B

Supplementary information for Chapter 3

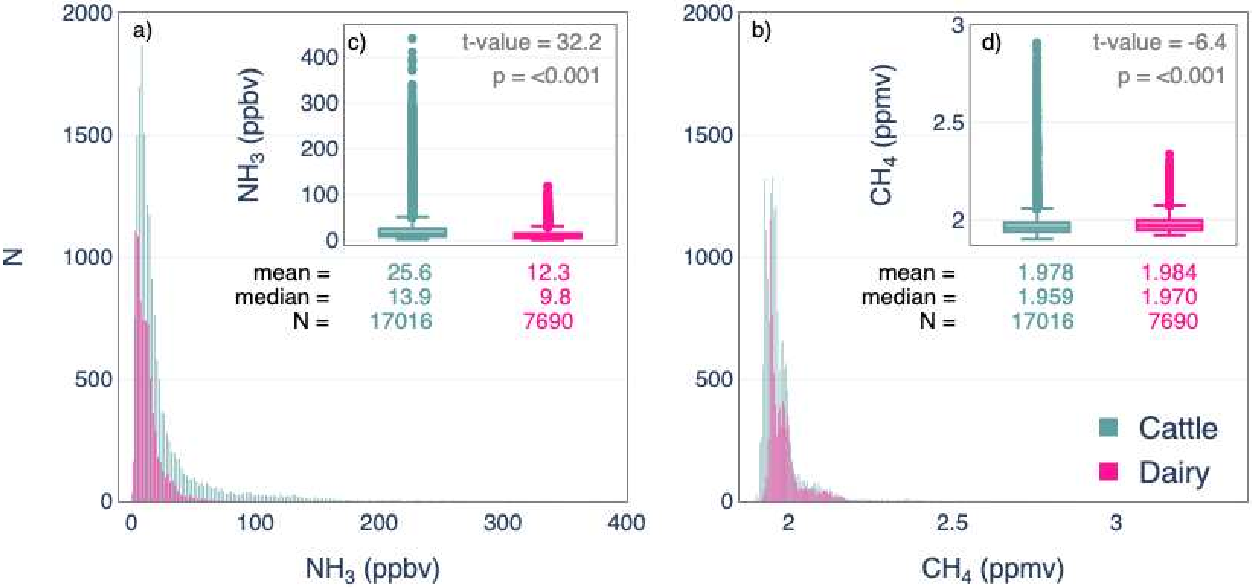

Figure B.1: Distribution of $\mathrm{NH_3}$ (panels a) and c)) and $\mathrm{CH_4}$ (panels b) and d)) for sampled facilities housing beef battle (blue) and dairy cows (pink) without correcting for $\mathrm{CH_4}$ emissions from oil and gas. Results of a t-test are shown in inset panels c) and d) for each trace gas.

$$NH_3\ EmR(T) = \frac{A_0}{T} \cdot exp(\frac{-10378}{T}) \tag{B.1}$$

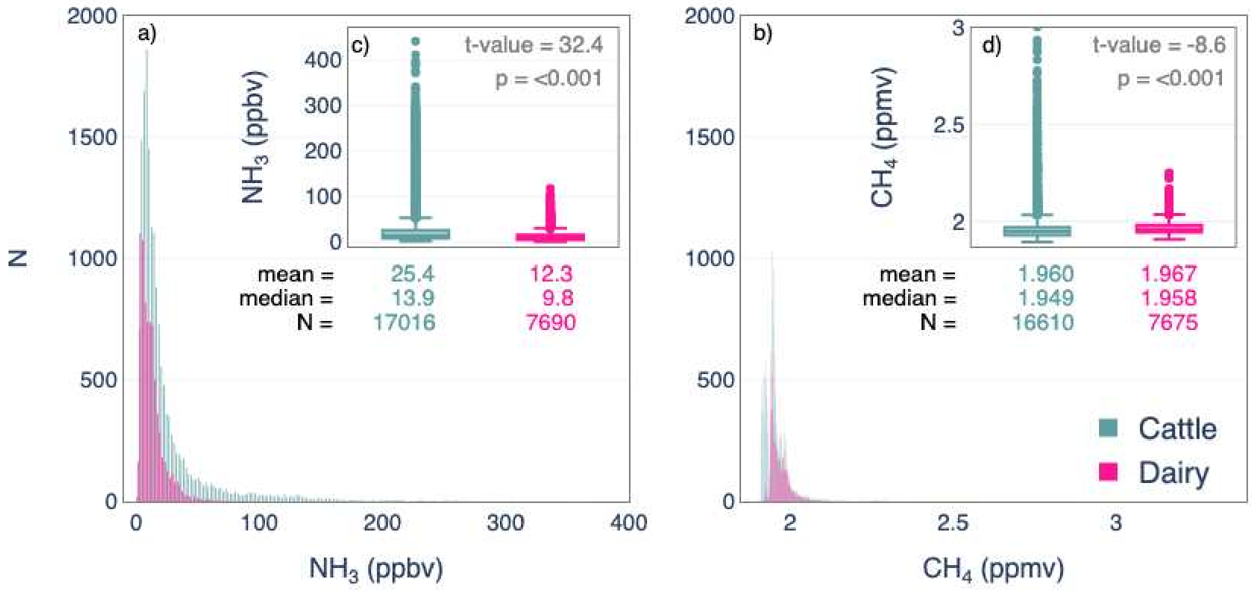

Figure B.2: Same as Figure B1 but using CH_{4_ag} from the linear regression analysis using multiple predictors. Results of t-tests are shown in inset panels c) and d) for each trace gas.

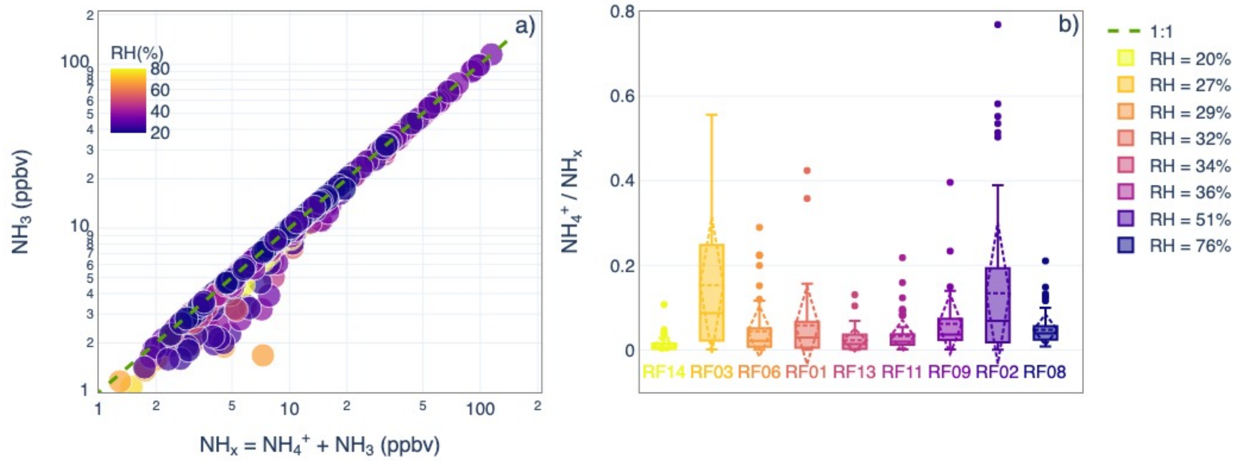

Figure B.3: a) NH_3 as a function of total ammonium (NH_x=NH_3+NH_4^+) for 2 min data colored by RH (%). b) Distribution of NH_4^+ over total NH_x for each research flight colored and ordered by the average RH during the sampling period.

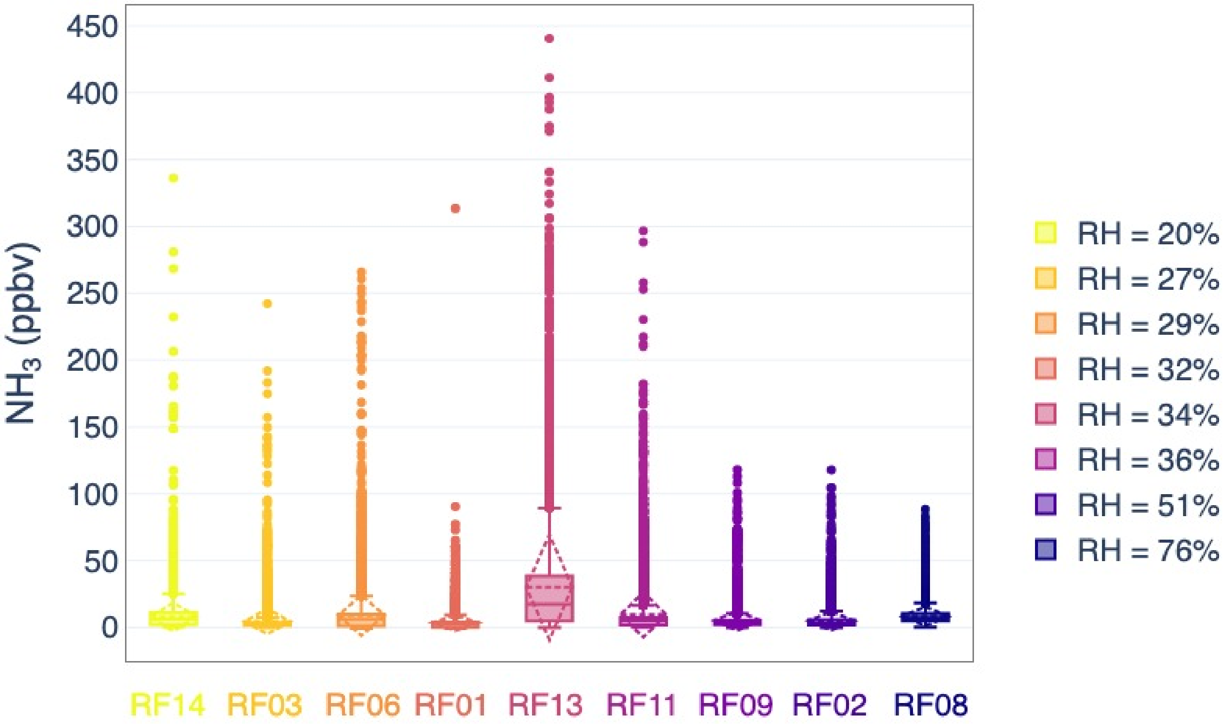

Figure B.4: Distribution of NH_3 for each research flight (RF) colored and ordered by the average RH during the sampling period.

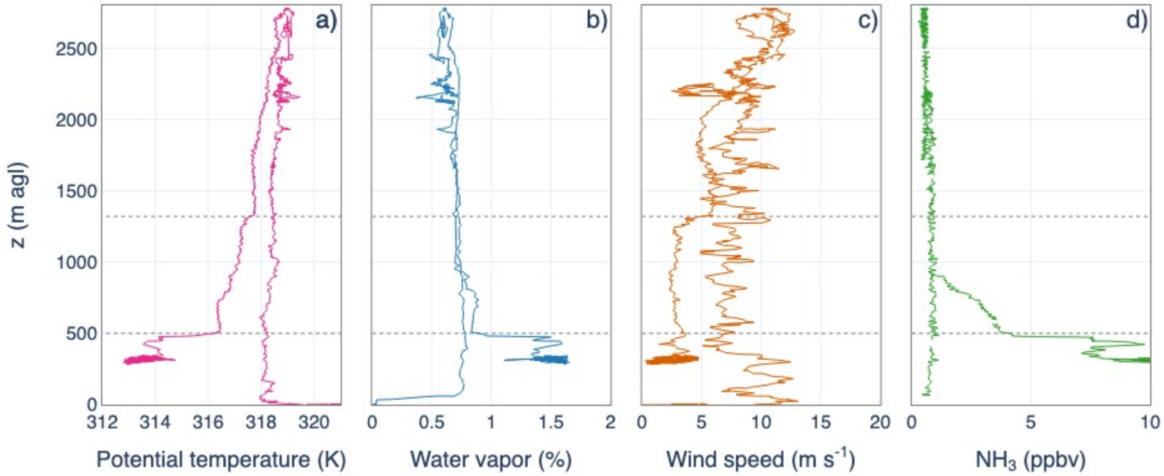

Figure B.5: Vertical profiles of a) potential temperature (K), b) water vapor (%), c) wind speed (m s^{-1}), and d) NH_3 (ppbv) for August 23, 2021 during the sampling of F04 during RF13. Dash lines show the two altitudes at which the two invertions were identified: ∼500 m agl and ∼1300 m agl

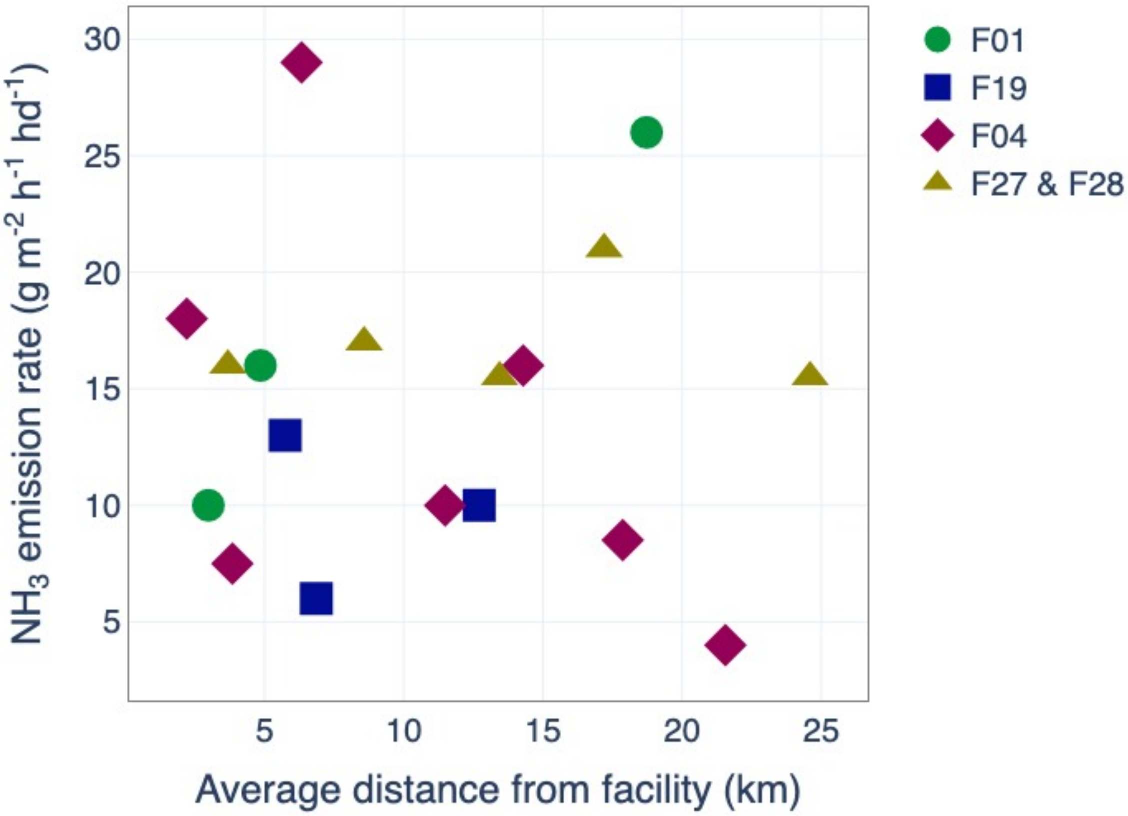

Figure B.6: NH_3 emission rates (g $NH_3 \cdot h^{-1} \cdot hd^{-1}$) for F01 (green circles), F19 (blue squares), F04 (red diamonds), and F27/27 (mustard triangles) as a function of distance from the corresponding facility.

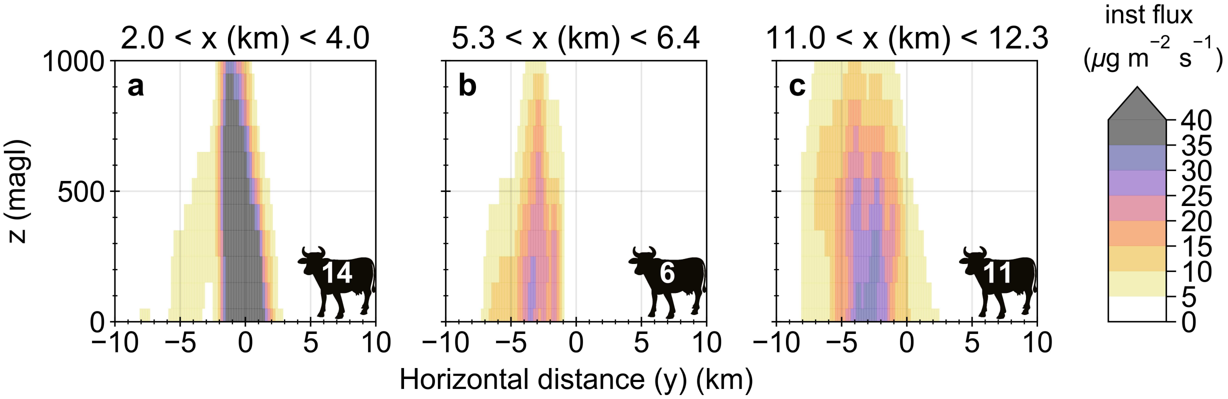

Figure B.7: NH_3 emissions rates for F19 - RF08 for a) 2 - 4, b) 5.3 - 6.4, and c) 11 and 12.3 km downwind of the targeted facility. Colorbar shows instantaneous fluxes in each grid cell in $\mu g\ m^{-2}\ s^{-1}$. Grid cells are 200 (horizontal) x 100 (altitude) m. The number in the lower right corner shows the total inferred emission rates in g $NH_3 \cdot h^{-1} \cdot hd^{-1}$. Panels show simple linear interpolation using the python package scipy.interpolate, with a smooth factor of 1.

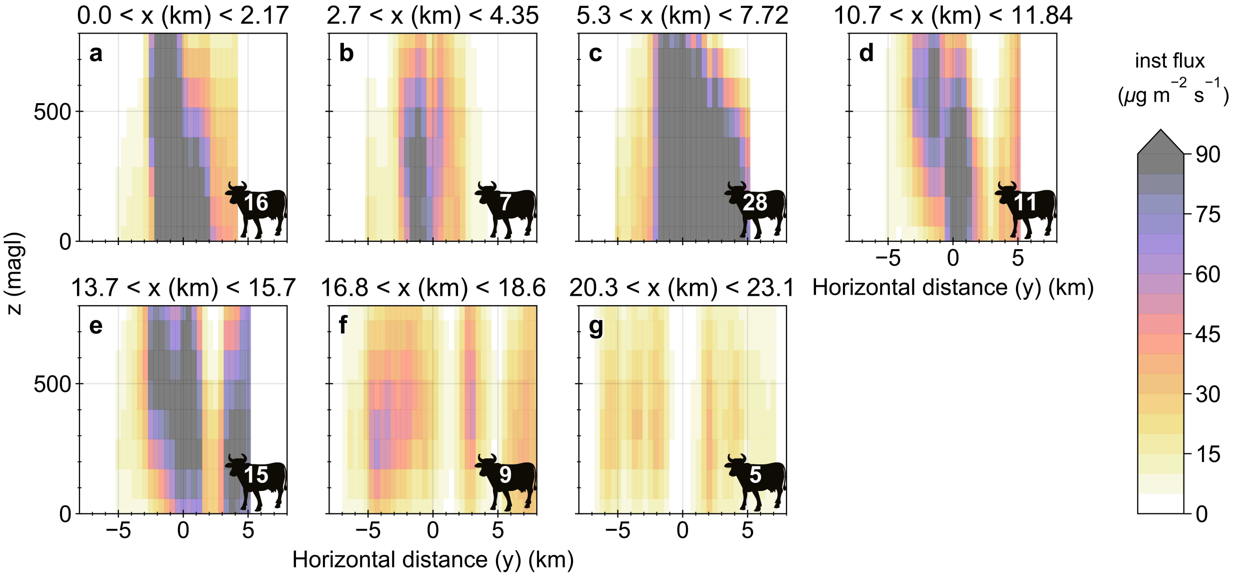

Figure B.8: NH_3 emissions rates for F04 - RF13 for a) 0 - 2.2, b) 2.7 - 4.3, c) 5.3 and 7.72, d) 10.7 - 11.8, e) 13.7 - 15.7, f) 16.8 - 18.6, and (g) 20.3 - 23.1 km , downwind of the targeted facility. Colorbar shows instantaneous fluxes in each grid cell in $\mu g\ m^{-2}\ s^{-1}$. Grid cells are 200 (horizontal) x 100 (altitude) m. The number in the lower right corner shows the total inferred emission rates in g $NH_3 \cdot h^{-1} \cdot hd^{-1}$. Panels show simple linear interpolation using the python package scipy.interpolate, with a smooth factor of 1.

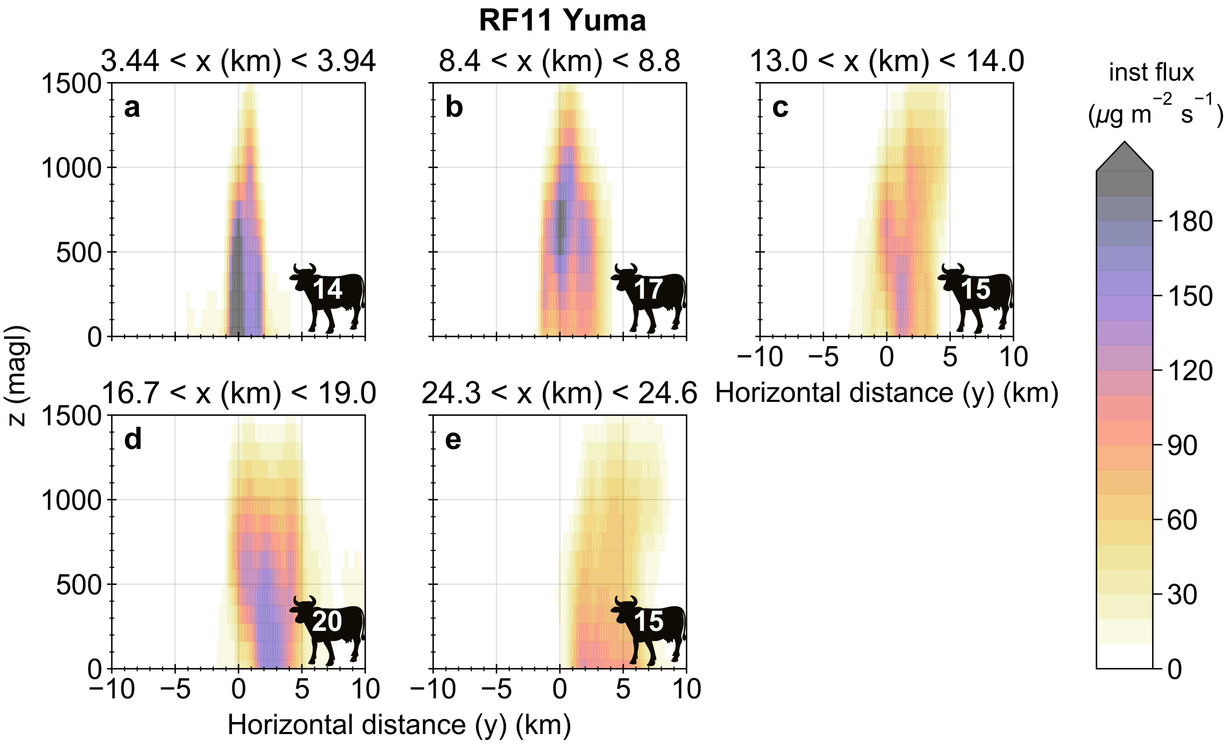

Figure B.9: NH_3 emissions rates for F27 and F28 - RF11 for a) 3.4 - 3,9, b) 8.4 - 8.8, c) 13 and 14, d) 16.7 - 19, and e) 24.3 - 24.6 km downwind of targeted facility F27. Colorbar shows instantaneous fluxes in each grid cell in $\mu g\ m^{-2}\ s^{-1}$. Grid cells are 200 (horizontal) x 100 (altitude) m. The number in the lower right corner shows the total inferred emission rates in g $NH_3 \cdot h^{-1} \cdot hd^{-1}$. Panels show simple linear interpolation using the python package scipy.interpolate, with a smooth factor of 1.

Appendix C

Supplementary information for Chapter 4

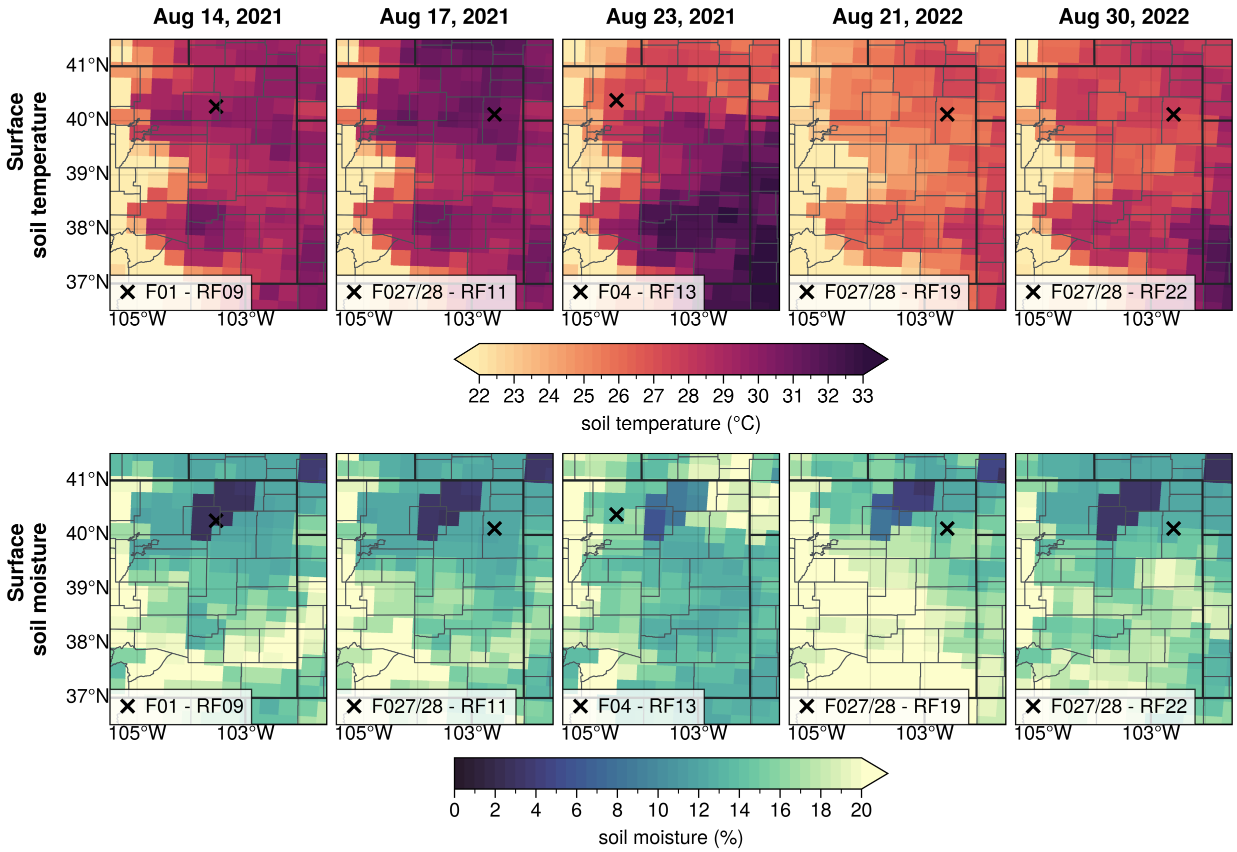

Figure C.1: Soil temperature (top panels) and moisture (bottom panels) for the surface underneath the plumes presented in this study.

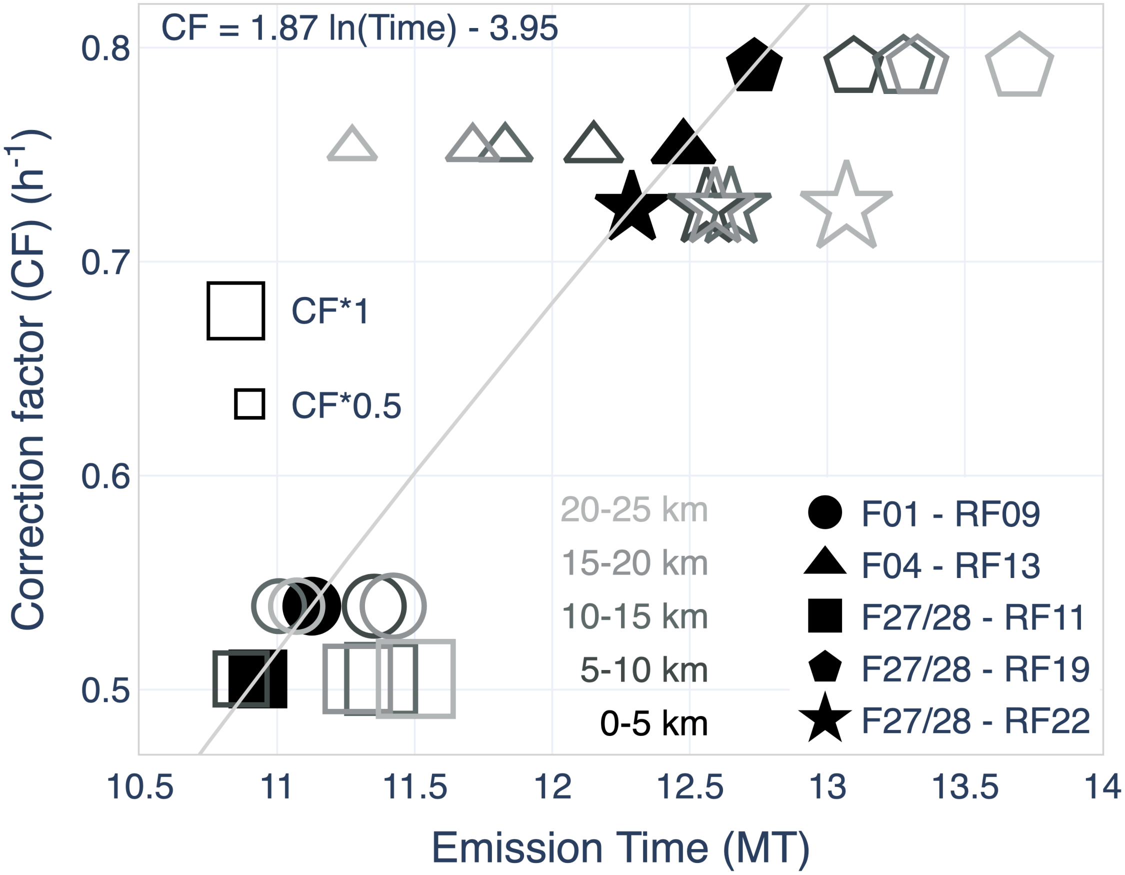

Figure C.2: Correction on NH_3 EmR representative of curtains > 5 km downwind of the facility (grey colors) relative to the first curtain (black 0 km<= x < 5 km). The symbols represent different facilities. The different colors represent the different curtain downwind. The size of the symbol represent the correction applied to each of the curtains relative to the first curtain.

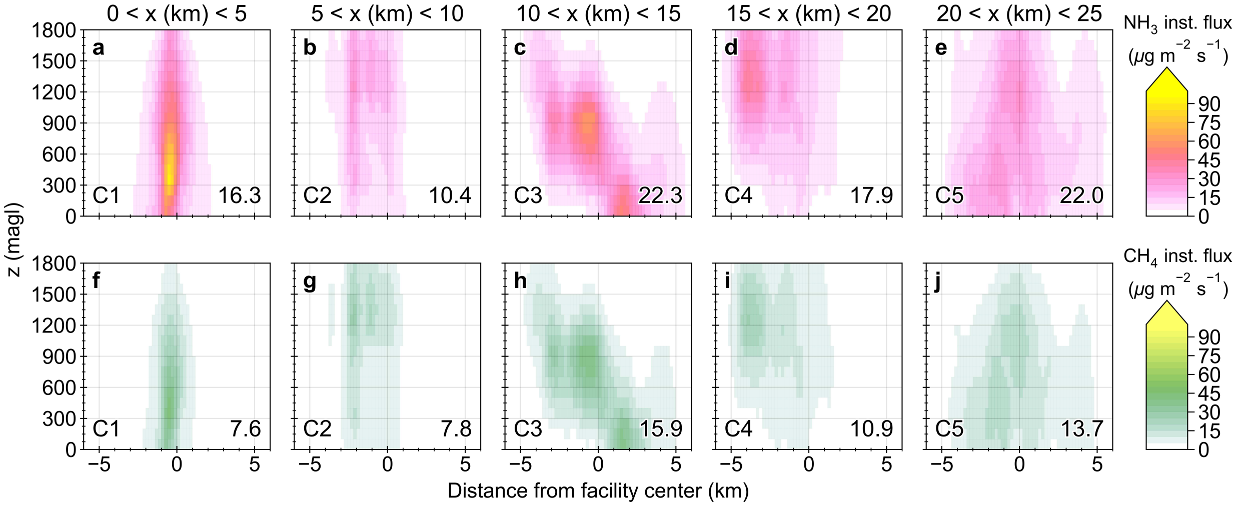

Figure C.3: NH$_3$ (top row) and CH$_4$ (bottom row) mass conductances (J) for the F01 sampled during RF09 on August 14, 2021. Panels a - e and f - j present J_{NH3} and J_{CH4_ag} every 5 km downwind of the facility. The colorbar refers to the inferred instantaneous horizontal fluxes in each grid cell in $\mu g\, m^{-2}\, s^{-1}$. Grid cells are 200 m wide and 100 m high. The number in the lower right corner is the integrated mass conductance (J) per hour per head of cattle in $g \cdot hr^{-1} \cdot head^{-1}$ for each domain (or ''curtain'' C). Panels show simple linear interpolation using the python package scipy.interpolate, with a smooth factor of 1.

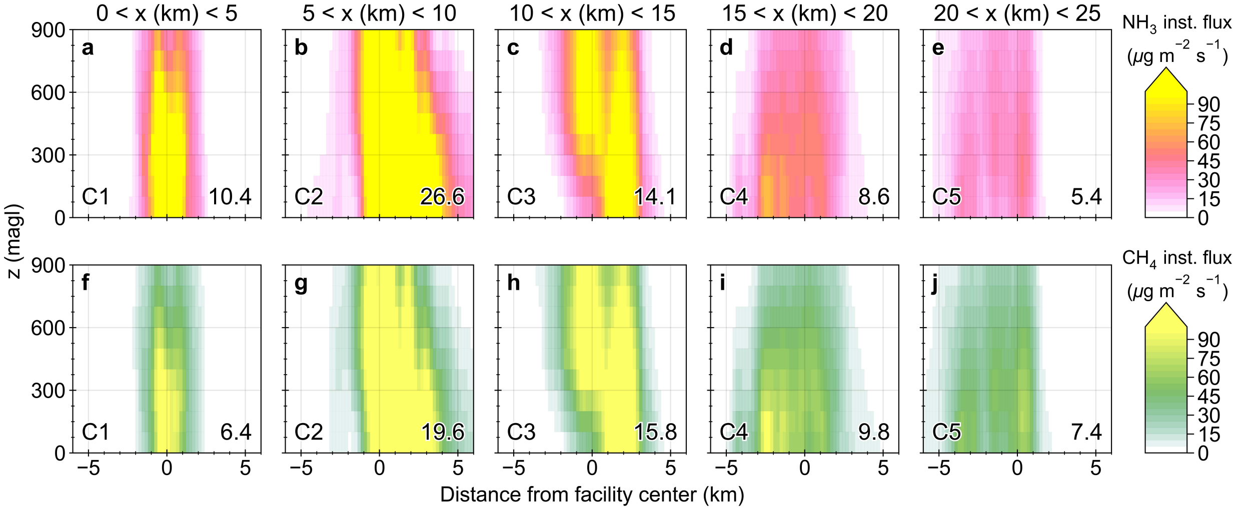

Figure C.4: NH$_3$ (top row) and CH$_4$ (bottom row) mass conductances (J) for the F04 sampled during RF13 on August 23, 2021. Panels a - e and f - j present J_{NH3} and J_{CH4_ag} every 5 km downwind of the facility. The colorbar refers to the inferred instantaneous horizontal fluxes in each grid cell in $\mu g\, m^{-2}\, s^{-1}$. Grid cells are 200 m wide and 100 m high. The number in the lower right corner is the integrated mass conductance (J) per hour per head of cattle in $g \cdot hr^{-1} \cdot head^{-1}$ for each domain (or ''curtain'' C). Panels show simple linear interpolation using the python package scipy.interpolate, with a smooth factor of 1.

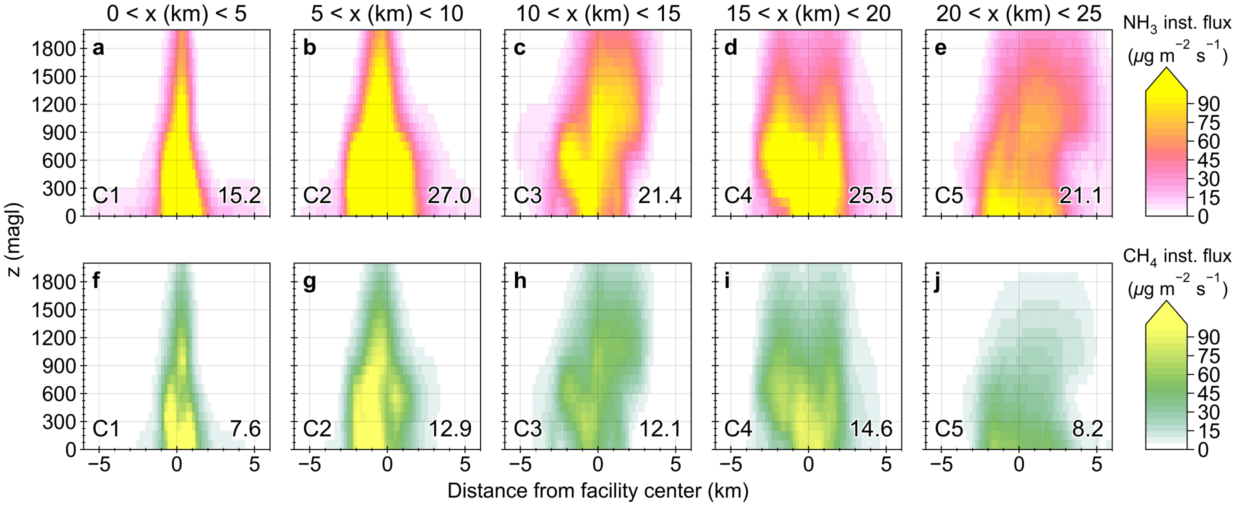

Figure C.5: NH_3 (top row) and CH_4 (bottom row) mass conductances (J) for the F27/28 sampled during RF11 on August 17, 2021. Panels a - e and f - j present J_{NH3} and J_{CH4_ag} every 5 km downwind of the facility. The colorbar refers to the inferred instantaneous horizontal fluxes in each grid cell in $\mu g\ m^{-2}\ s^{-1}$. Grid cells are 200 m wide and 100 m high. The number in the lower right corner is the integrated mass conductance (J) per hour per head of cattle in $g \cdot hr^{-1} \cdot head^{-1}$ for each domain (or ''curtain" C). Panels show simple linear interpolation using the python package scipy.interpolate, with a smooth factor of 1.

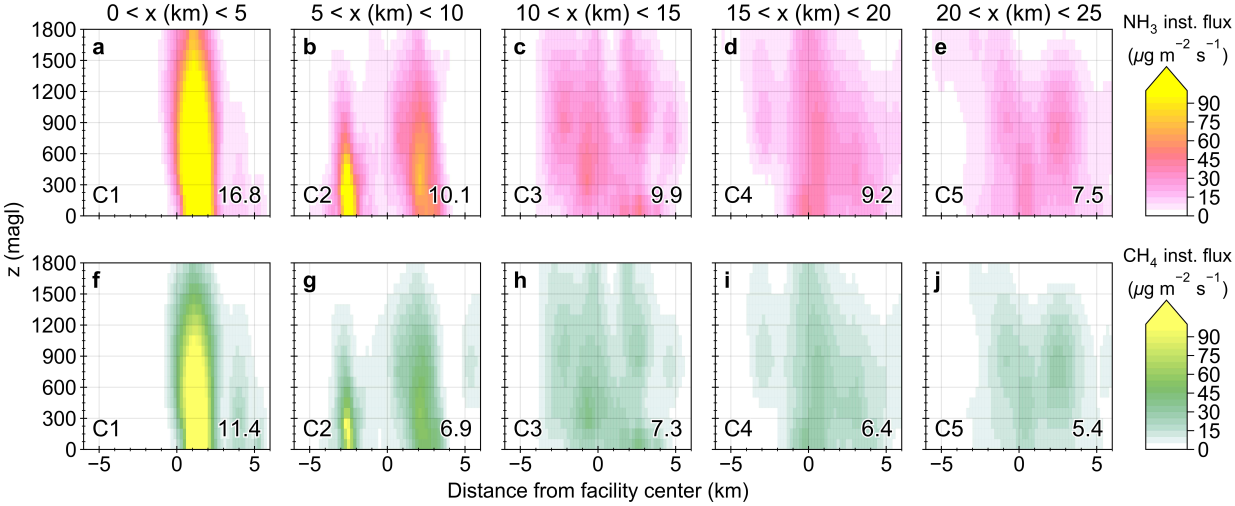

Figure C.6: NH_3 (top row) and CH_4 (bottom row) mass conductances (J) for the F27/28 sampled during RF19 on August 21, 2022. Panels a - e and f - j present J_{NH3} and J_{CH4_ag} every 5 km downwind of the facility. The colorbar refers to the inferred instantaneous horizontal fluxes in each grid cell in $\mu g m^{-2} s^{-1}$. Grid cells are 200 m wide and 100 m high. The number in the lower right corner is the integrated mass conductance (J) per hour per head of cattle in $g \cdot hr^{-1} \cdot head^{-1}$ for each domain (or ''curtain" C). Panels show simple linear interpolation using the python package scipy.interpolate, with a smooth factor of 1.

Appendix D

Supplementary information for Chapter 5

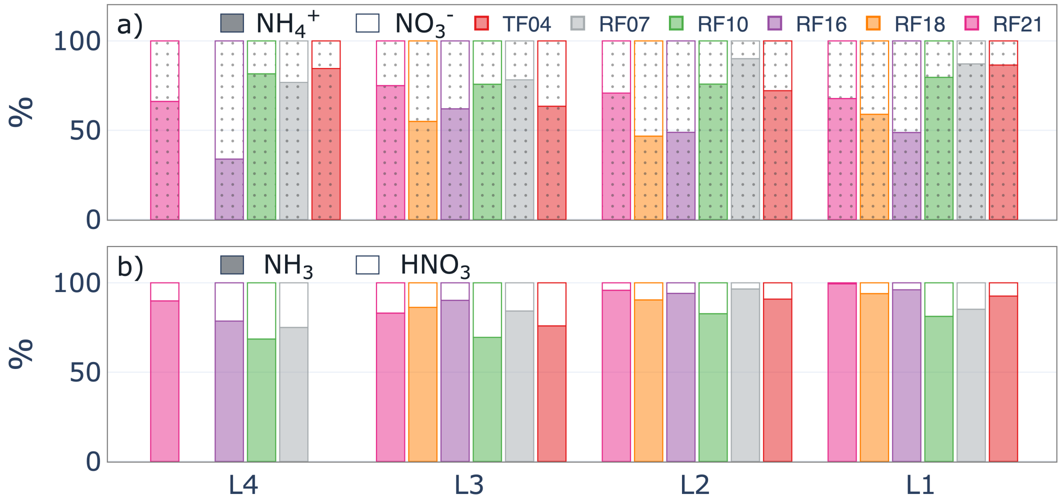

Figure D.1: a) 2-min PILS $NH_4{}^+$ and $NO_3{}^-$ percentage contribution from concentrations shown in Figure 5.1. b) same as a) for gas-phase NH_3 and HNO_3.

During $\mathrm{TRANS^2Am}$, the 2-min submicron aerosol composition was measured using a PILS. Figure D.1 shows the average aerosol composition in each leg for each of the upslope events sampled. The top row shows the events sampled during Phase I in 2021. Phase I of $\mathrm{TRANS^2Am}$ was impacted by aged smoke transported from the Pacific Northwest and California fires. Levoglucosan (brown) is commonly used as a smoke tracer (Simonet et al., 1999)and is present in the aerosol composition of the 2021 flights (top row) and not in the 2022 flights (bottom row).

Figure D.2 shows that the concentration of aerosols sampled by the PILS is always <6 μg/m^3 and that the cations (Na$^+$, K$^+$, Mg^{2+}, Ca^{2+}) and organics measured (green) are a large fraction (50 - 75$\%$) of the aerosols sampled. On the other hand, the inorganic $SO_4{}^{2+}$ - $NO_3{}^+$ - $NH_4{}^+$ system is rarely more than 20$\%$ of the total aerosol composition (e.g., the inorganic system is >25$\%$ for L1).

Figure D.2: Average aerosol composition for all upslope flights (a) TF04, b) RF07, c) RF10, d) RF16, e) RF18, f) RF21) for each leg: L1-L4 from bottom to top in each panel.

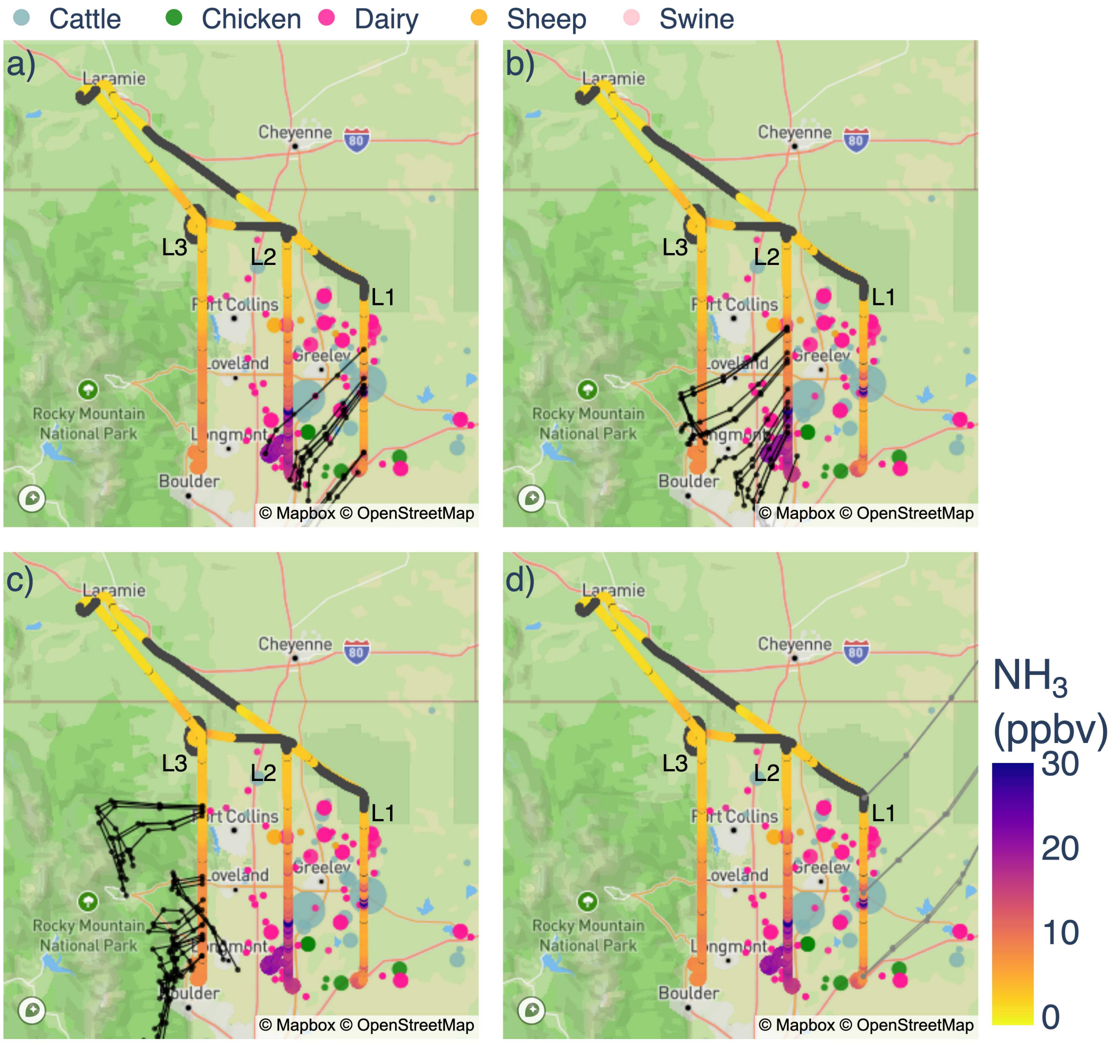

Figure D.3: UWKA flight track colored by NH_3 mixing rations during RF18 on August 19, 2022. The wind roses on the top right corner correspond to the wind observed in each of the legs (a) - (c) corresponding to L1 - L3, respectively. Circles signify livestock housing facilities colored by type of animal and sized by the reported maximum animal capacity. The black and grey lines show HYSPLIT forward and backward trajectories, respectively. Each dot within the lines represents one hour of transport.

Figure D.3 shows the flight track and wind profiles from RF18. This was the earliest upslope event sampled during $\mathrm{TRANS^2Am}$ due to the forecast of storms over the mountains later in the day. Therefore, the planning team decided to skip L4 due to the presence of clouds and the threat of storms. This upslope event observed the strongest wind systems on L1 and L2 across all the upslope events sampling during $\mathrm{TRANS^2Am}$. Wind up to 8 m s^{-1} from the NNE made for an efficient transport of airmasses from L1 to L2 and further southwest. This is evident in the $\mathrm{NH_3}$ enhancement south of L2. This is one of the cases where the regional gradient of $\mathrm{NH_3}$ might be overestimated because the more southern portion of L3 did not cover the whole plume observed in L1 and L2, as it was transported further south (e.g., towards Denver) into restricted air space. The back trajectory analysis in Figure D.3d shows that the NE system was already set up early in the morning, effectively transporting air masses from the neighboring states of Nebraska and South Dakota.

Note that along L3, a much weaker easterly flow can be observed, more similar to what was observed in the other upslope events sampled during $\mathrm{TRANS^2Am}$. However, the back trajectories show the recirculation of airmasses along L3 and not L4, suggesting NW flow recirculating airmasses from the south and east later in the day.

Wind patterns associated with high $\mathrm{NH_3}$ in RMNP.

Ammonia Airsenty Data

Near real-time $\mathrm{NH_3}$ concentrations were measured at the IMPROVE site in Rocky Mountain National Park using an Air Sentry II Ammonia Ion Mobility Spectrometer (Particle Measuring Systems). The Air Sentry was deployed in the shelter at the site from July 2021 through August 2022 and provided 30s integrated measurements of $\mathrm{NH_3}$. It sampled from a ¼” Teflon line heated to 40°C. A fiber filter was located at its inlet to remove particles. The Air Sentry required a continuous supply of clean, dry zero air in order to operate, which was supplied using a Teledyne portable zero air generator. In addition, during site visits, zero measurements were periodically made by overflowing the inlet with ultra-high purity zero air supplied from a cylinder for 30 min.

Ammonia Denuder Data

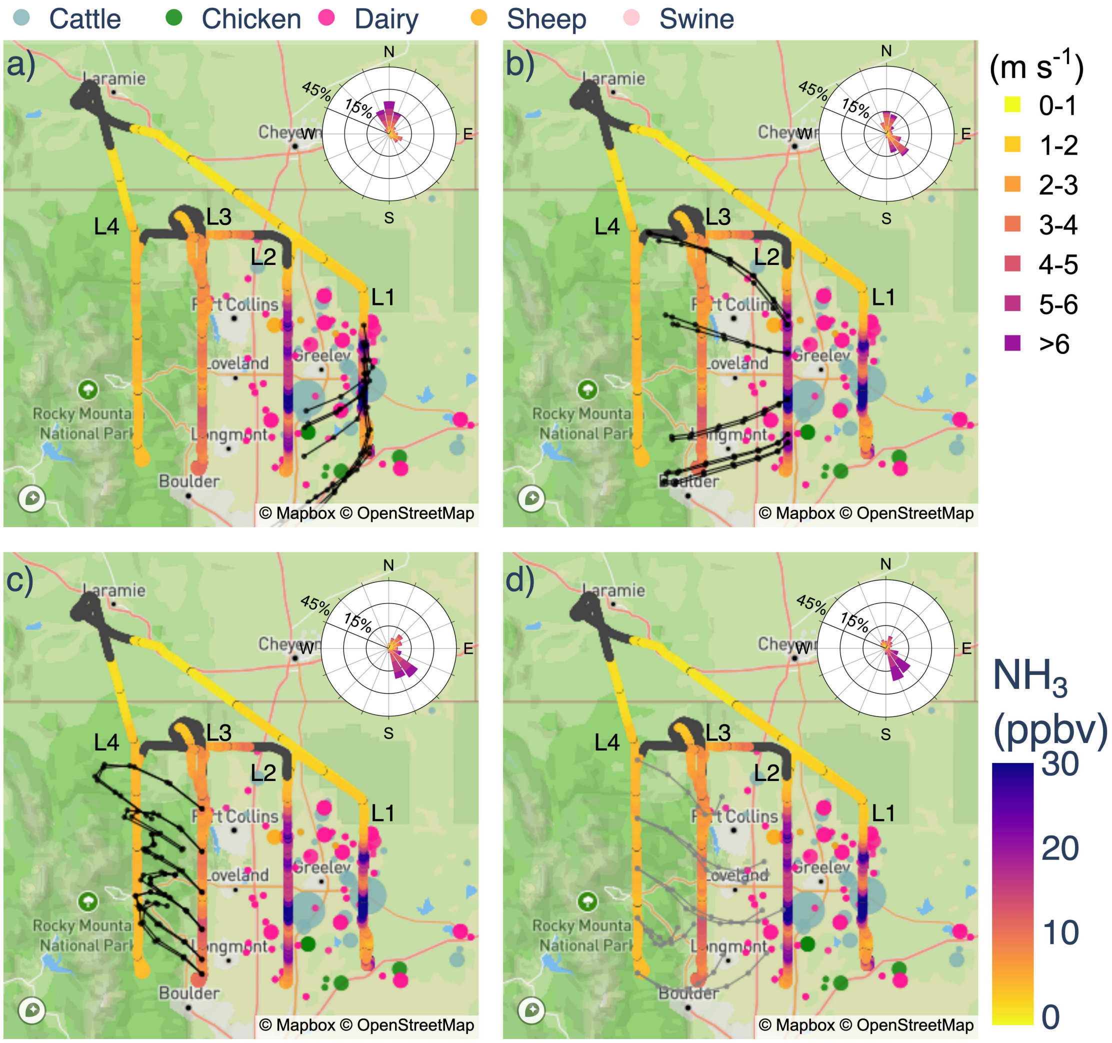

Figure D.4: UWKA flight track colored by NH$_3$ mixing rations during RF21 on August 29, 2022. The wind roses on the top right corner correspond to the wind observed in each of the legs (a) - (d) corresponding to L1 - L4, respectively. Circles signify livestock housing facilities colored by type of animal and sized by the reported maximum animal capacity. The black and grey lines show HYSPLIT forward and backward trajectories, respectively. Each dot within the lines represents one hour of transport.

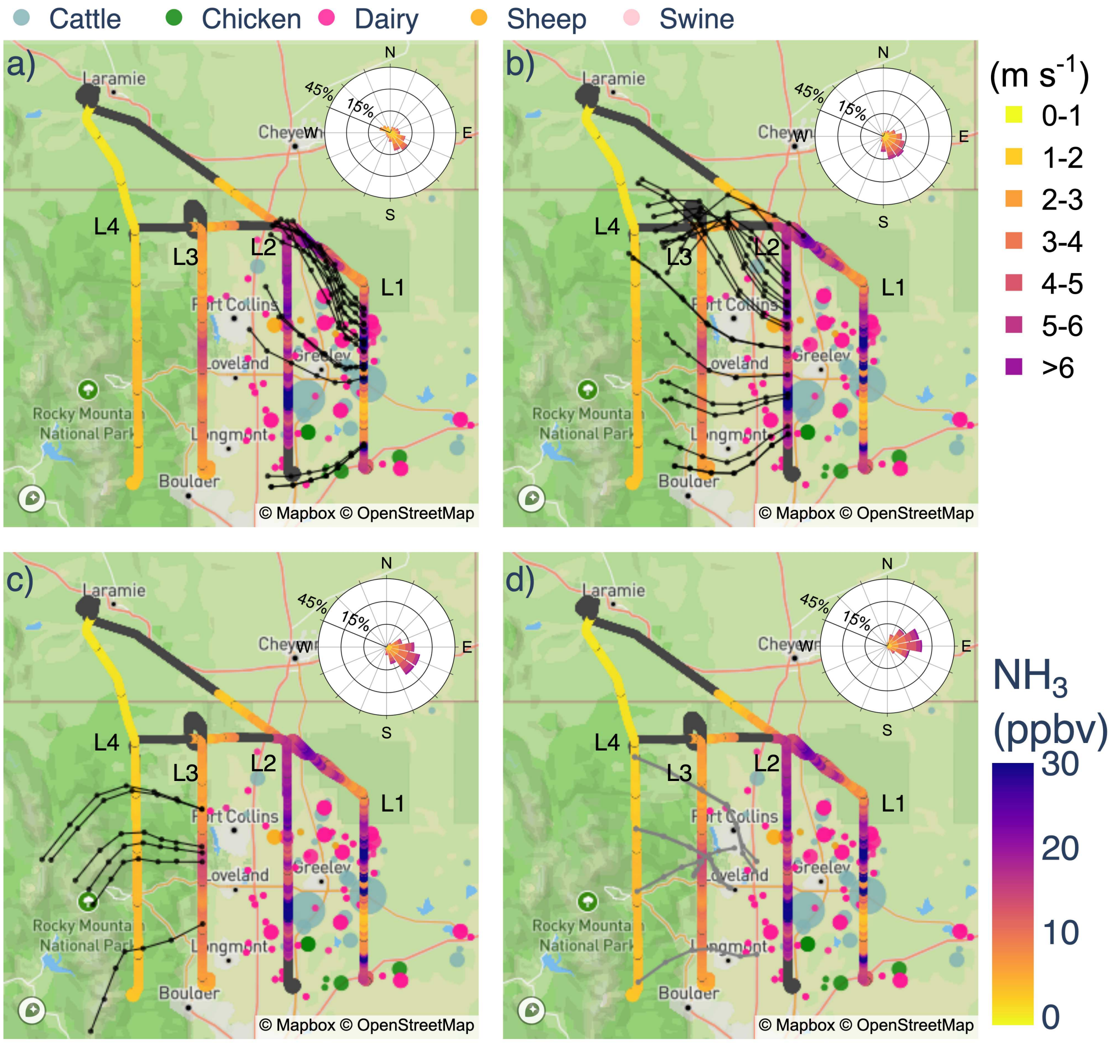

Figure D.5: UWKA flight track colored by NH$_3$ mixing rations during RF16 on August 17, 2022. The wind roses on the top right corner correspond to the wind observed in each of the legs (a) - (d) corresponding to L1 - L4, respectively. Circles signify livestock housing facilities colored by type of animal and sized by the reported maximum animal capacity. The black and grey lines show HYSPLIT forward and backward trajectories, respectively. Each dot within the lines represents one hour of transport.

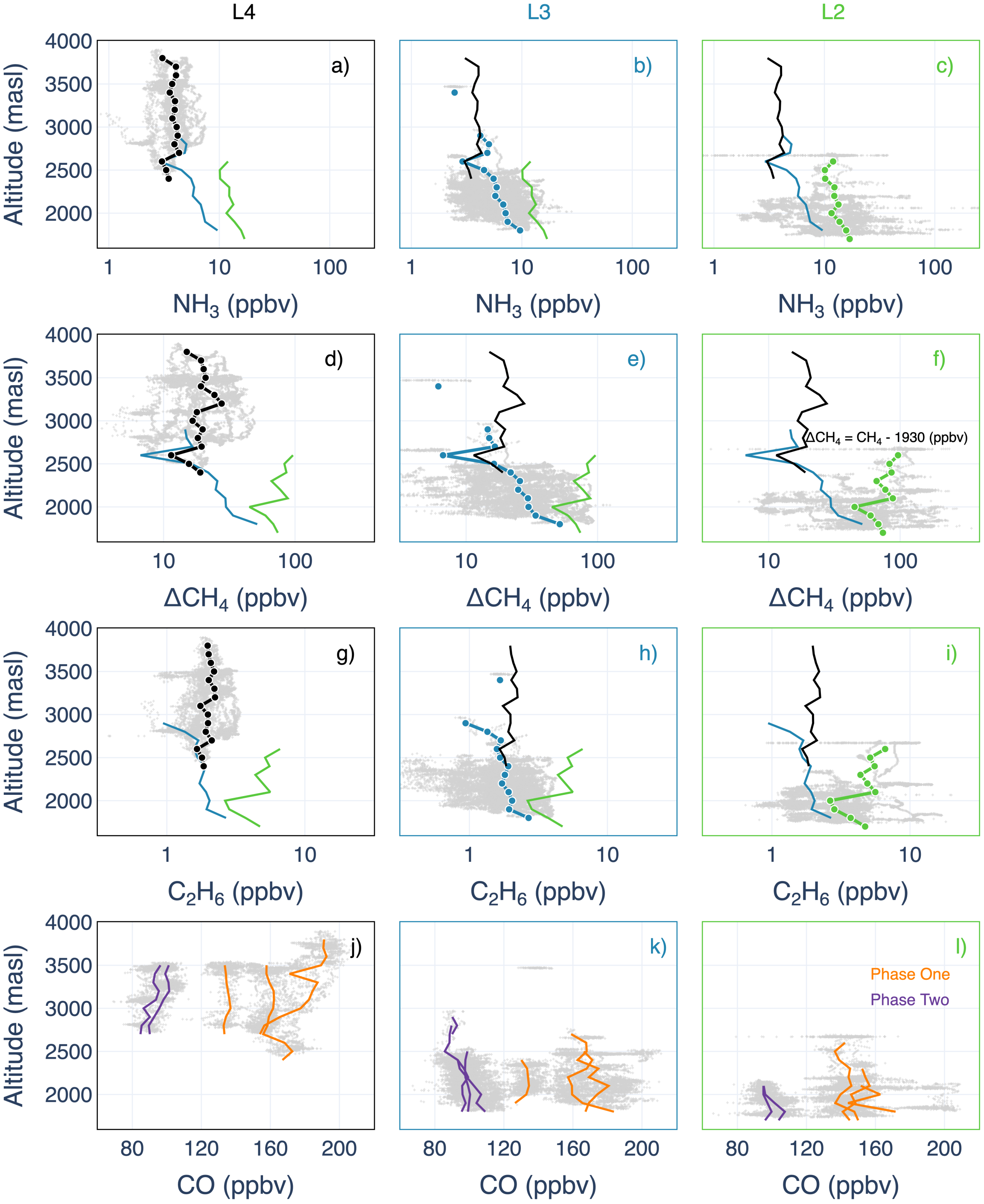

Figure D.6: (a-i) 1-Hz NH_3 (top row), ΔCH_4 (second row), C_2H_6 (third row) vs. altitude binned by L4 (first column; black), L3 (middle column; blue), and L2 (third column; green). Lines with circles in each panel show altitudinal averages across that leg for all the flights. Lines with no circles show latitudinal averages for the other two legs. Colors remain the same across all the data (L4: black; L3: blue; and L2: green). (j - l) 1-Hz CO vs. altitude binned by legs. Each line represents the altitudinal averages for CO for each flight in that leg (flights in Phase One: orange; Phase Two: purple).

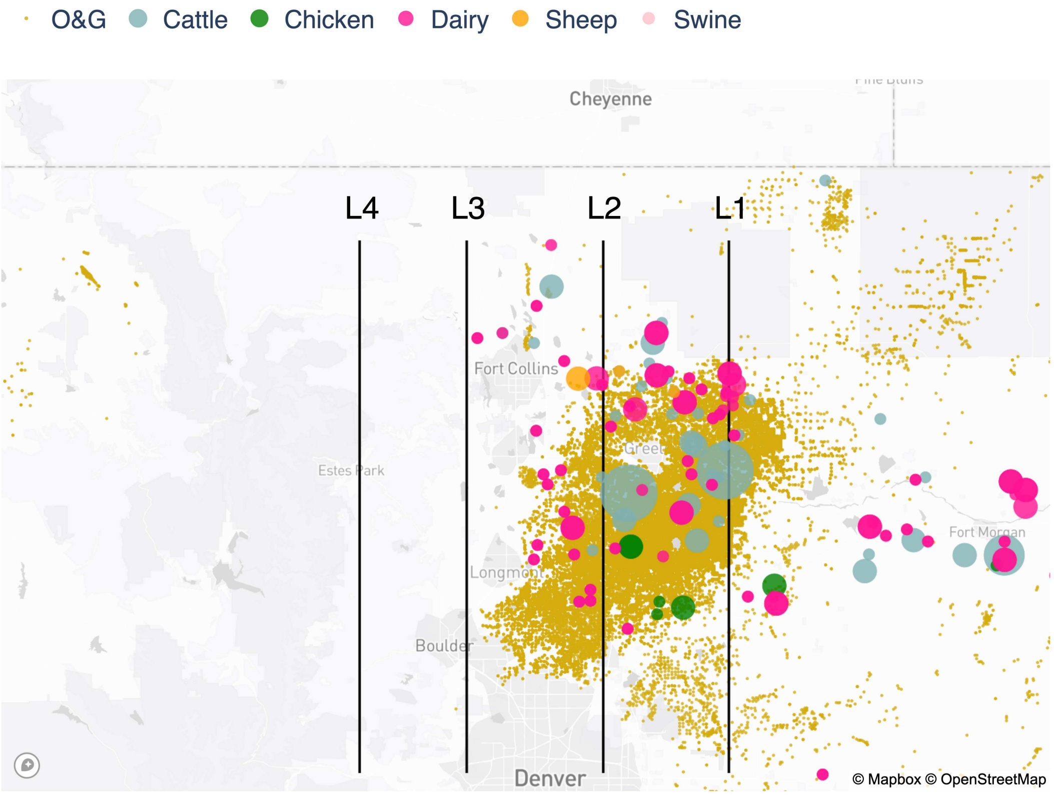

Figure D.7: Map of The TRANS^{2}Am study region. Lines show the average longitude of the legs flown during the six flights presented here. The sized and colored dots show the different livestock facilities in the region. The yellow dots represent the location of oil and gas wells as of 2015.

University Research Glassware (URG) denuder and filter pack samples were collected on the NEON flux tower located in Rocky Mountain National Park adjacent to the IMPROVE site from August to September 2021 to measure inorganic gases, including $\mathrm{NH_3}$ and particle species. Two samplers were located on both the 4th (middle) and 7th (top) levels of the tower. On sampling days, URG denuder and filter packs samples were collected from 9 am-1 pm, 1:30-5:30 pm, and overnight from 8 pm-6 am. The URG samplers operated by pulling ambient air through a $\mathrm{PM_{2.5}}$ cyclone at 16.7 LPM. The air then passed through a sodium carbonate-coated denuder, a phosphorous acid-coated denuder to collect $\mathrm{NH_3}$, and a 47 mm nylon filter (MTL Nylasorb, 1.0 m pore size) to capture $\mathrm{PM_{2.5}}$ particles. Finally, an additional phosphorous acid-coated denuder was located downstream of the filter to capture any $\mathrm{NH_3}$ volatilized from ammonium nitrate initially captured on the filter. After collection, the samples were brought back to the laboratory at Colorado State University. The denuders were extracted in 10 mL of deionized water and analyzed on a Dionex DX-500 ion chromatograph. A Dionex IonPac CS12A (3x120 mm) analytical column using 20 mM methanesulfonic acid eluent at a flow rate of 0.5 mL/min was employed to analyze the phosphorous acid-coated denuders. The injection volume was 190 µL with an analysis time of 17 minutes.

Meteorological Data

Wind data for RMNP was retrieved from data collected at the flux tower from the National Ecological Observatory Network (NEON) located at 40.275º N, 105.546º W, and 9022 ft agl, and from the IMPROVE station located at 40.36º N, 105.56º W and 7900 ft agl. Wind data for Fort Collins was retrieved using the observations at Christman Field, a site located near the foothills at 40.597º N, 105.143º W, and 5160 ft agl. Wind data for Greeley was retrieved using the observation from the MesoWest portal from the Greeley Airport, located near the foothills at 40.425 N, 104.635º W, and 4659 ft agl.

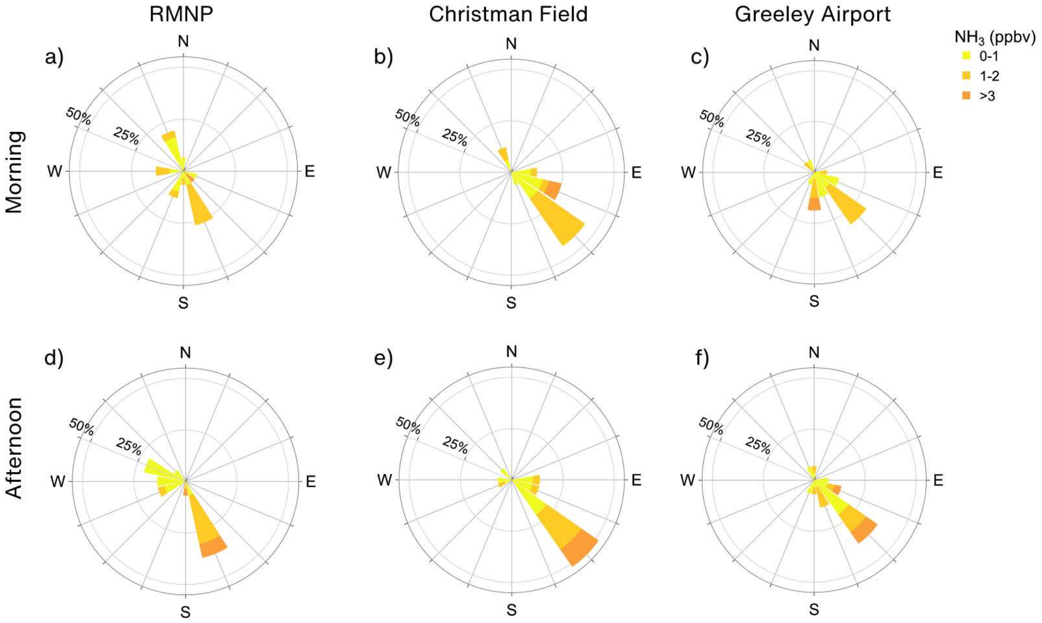

Figure D.8: NH_3 mixing ratios measured at RMNP during the summer of 2021 as a function of wind direction in RMNP (left), Fort Collins (center), and Greeley (right). NH_3 mixing ratios are from denuder measurements in the morning (top row) and afternoon (bottom row) above the canopy collected at RMNP.

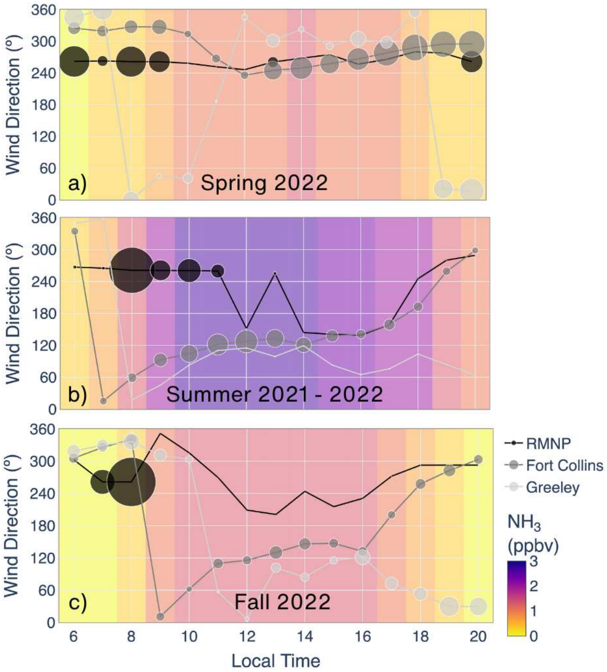

Figure D.9: Diurnal wind profile for summers 2021 and 2022 (2021-07-09 - 2021-31-08; 2022-06-01 - 2022-08-10; top panels) and spring 2022 (2022-04-01 - 2022-06-01; middle panels) and fall 2021 (2021-09-01 - 2021-11-30; bottom panels) in northeastern Colorado using data from surface stations in RMNP-IMPROVE (black), Fort Collins (grey), and Greeley (light grey). The size of the markers is proportional to the magnitude of the wind speed. The background colors show the average NH_3 concentration measured at RMNP using observation from an Air Sentry. The background colors represent average diurnal NH_3 mixing ratios using observation from the CSU Ammonia Airsentry.